Photoswitching of Lipids and Silicification of DNA Origami Objects Probed by Small-Angle X-ray Scattering

Martina Franziska Ober

Munich 2022

Photoswitching of Lipids and Silicification of DNA Origami Objects Probed by Small-Angle X-ray Scattering

Martina Franziska Ober

Dissertation
an der Fakultät für Physik
der Ludwig-Maximilians-Universität
München

vorgelegt von
Martina Franziska Ober
aus Starnberg

München, den 2. März 2022

Erstgutachter: PD. Dr. Bert Nickel

Zweitgutachter: Prof. Dr. Jan Lipfert

Tag der mündlichen Prüfung: 27. April 2022

ZUSAMMENFASSUNG

Ein zentrales Ziel der Nanowissenschaften ist die Entwicklung artifizieller biomolekularer Nanoobjekte, die in der Lage sind, spezifische Funktionen zu erfüllen. Zu den Anwendungsgebieten solcher Nanoobjekte gehören die biochemische Diagnostik sowie die Nanomedizin. Um deren Funktion zu kontrollieren und zu verbessern, ist es essenziell ihre Struktur in Aktion zu untersuchen. Hierfür eignet sich die Kleinwinkelröntgenstreuung (SAXS), da sie eine hochauflösende, nicht-invasive und lösungsbasierte Methode zur Strukturanalyse im Nanobereich ist. In dieser Arbeit wurden mittels SAXS drei verschiedene Nanoobjekte untersucht: Gold-Silber-DNA Nanozylinder, photoschaltbare Lipidmembranen und mit Siliziumdioxid beschichtete Nanoobjekte aus DNA, so genannte DNA Origami. Einige dieser SAXS Messungen konnten nur durch die Verwendung von unüblich hohen Röntgenenergien bewerkstelligt werden. Daher wird zu Beginn der Arbeit die Rolle der Energie für SAXS an Nanopartikeln in wässriger Lösung sowie potenzielle Vorteile hoch energetischer SAXS Messungen eruiert. Anschließend wird die Strukturanalyse der mit DNA funktionalisierten Gold-Silber Nanozylinder präsentiert, welche von der Gruppe von T. Liedl für plasmonische Anwendungen entwickelt wurden. Das Synthesedesign dieser Nanozylinder konnte validiert, ihre exakte Größenverteilung bestimmt und das Vorhandensein einer homogenen DNA-Außenschicht bestätigt werden. Als Nächstes werden die Ergebnisse der Forschungen, eine Zusammenarbeit mit an Gruppe von T. Lohmüller und 0. Thorn-Seshold, an photoschaltbaren Lipidmembranen vorgestellt. Licht isomerisiert Photolipide in einen trans oder cis Zustand, was eine reversible Manipulation der Membraneigenschaften z.B. eine Membrandickenänderung von 10% ermöglicht. Obwohl solche makroskopischen Änderungen vielfach nachgewiesen wurden, konnten sie bisher noch nicht den spezifischen trans-zu-cis Verhältnissen der membranbildenden Photolipide zugeordnet werden. Diese Arbeit weist nun eine lineare Abhängigkeit der Membrandicke von dem trans-zu-cis Verhältnis nach. Bei idealen Schaltbedingungen ist demnach eine doppelt so große Dickenänderung (20%) möglicht. Außerdem wurde eine Abhängigkeit der Photoschalteffizienz von der Zusammensetzung der wässrigen Phase aufgedeckt. Eine Erweiterung der optischen Membranmanipulation bieten niederenergetische Röntgenstrahlen via quantitativem „katalytischen Schaltens“. Zuletzt wird die Forschung an mit Siliziumdioxid beschichtete DNA Origami Objekten, eine Zusammenarbeit mit der Gruppe von A. Heuer-Jungemann, präsentiert. Der Fokus liegt hier auf dem Einfluss des Siliziumdioxidwachstums auf die DNA Origami Form und dessen innere Feinstruktur. Es wurde dabei gezeigt, dass ein Siliziumdioxid Präkursor bei Beginn der Silifizierung ein erhebliches Zusammenziehen der DNA Struktur auslöst. Durch Ablagerung des Siliziumdioxid sowohl im Inneren als auch auf der Oberfläche des DNA Origamis vergrößert sich das entstehende Siliziumdioxid-DNA Nanokomposit wieder. Auf diese Weise können DNA Origami im Subnanometerbereich mit Siliziumdioxid verkapselt werden, während ihre übergeordnete Form und die innere Feinstruktur präzise erhalten bleibt. Darüber hinaus erhöht sich die Steifigkeit der DNA Origami, sowie ihre innere Gitterordnung und ihre thermische Stabilität.

ABSTRACT

A central goal in nanoscience is the design of artificial biomolecular constructs, which are capable to perform a specific function on the nanoscale. Fields of application of such nanoconstructs include diagnostic devices as well as nanomedicine. Recording the nanoobject's structure in action is key in controlling and optimizing their envisioned operation. Small-angle X-ray scattering (SAXS) is an excellent tool to study biomolecular structure on the nanoscale since it is non-invasive, solution-based, and high-resolution. Here, three nanoconstructs are investigated by SAXS: DNA-functionalized gold-silver core-shell nanorods, photoswitchable lipid membranes and silica-coated DNA origami objects. Some of these SAXS experiments use higher-than-usual X-ray energies. Thus, firstly, the role of the X-ray energy for solution-based SAXS and its potential benefits are evaluated. Secondly, the structure of gold-silver core-shell nanorods with enhanced plasmonic properties, which were synthesized and optically characterized by the group of T. Liedl, were studied by SAXS. Here, their synthesis design could be validated, their size distribution determined, and the presence of a homogeneous DNA coating, crucial for biocompatibility, be confirmed. Thirdly, the switching of photoresponsive lipid membranes that allow reversible manipulation of membrane properties was investigated in cooperation with the group of T. Lohmüller and O. Thorn-Seshold. Light-driven molecular switching from the photolipid's trans-to-cis isomerization state and vice versa, translates into a membrane thickness change of ca. 10% upon UV and blue light illumination, respectively. Though these macroscopic responses are clear, it was unclear how large the respective changes of trans/cis ratio are, and if they can be improved. By linear correlation of the thickness to the trans/cis ratio, a dependency of photoswitching upon aqueous phase composition is revealed and experimentally possible thickness variations twice as large shown. Furthermore, soft X-rays (8keV) have been demonstrated to isomerize photolipid membranes to the all-trans state by a process called catalytic switching and thus to extend the optical control. Lastly, DNA origami objects coated with a protective silica encapsulation are investigated in cooperation with the A. Heuer-Jungemann group. Here, the influence of the silica growth on the DNA origami shape and its inner fine structure was studied in-situ during the silicification. We observed a substantial condensation of the DNA origami object induced by one of two silica precursors, prior to its expansion in response to silica formation on and within the DNA origami. This way, a sub-nanometer thin silica coating is yielded. Beyond that, silicification preserves the shape and inner find structure in great detail, provides thermal stability for the DNA nanoconstruct, and increases the DNA origami's rigidity and lattice order. Thus, the SAXS studies performed in this thesis accomplished the in-situ characterization of highly complex nanoconstructs in action and contributed to extend the control over their designed function.

PUBLICATIONS

Core publications of this thesis

L. Nguyen, M. Dass, **M. F. Ober**, L. V. Besteiro, Z. M. Wang, B. Nickel, A. O. Govorov, T. Liedl, A. Heuer-Jungemann, Chiral Assembly of Gold-Silver Core-Shell Plasmonic Nanorods on DNA Origami with Strong Optical Activity. *ACS Nano* 2020, 14 (6), 7454-7461. DOI: 10.1021/acsnano.0c03127

P. Urban*, S. D. Pritzl*, **M. F. Ober** *, C. F. Dirscherl, C. Pernpeintner, D. B. Konrad, J. A. Frank, D. Trauner, B Nickel, T. Lohmueller, A Lipid Photoswitch Controls Fluidity in Supported Bilayer Membranes. *Langmuir 2020*, 36 (10), 2629-2634. DOI: 10.1021/acs.langmuir.9b02942
*contributed equally to this work

S. Pritzl, D. B. Konrad, **M. F. Ober**, A. F. Richter, J. A. Frank, B. Nickel, D. Trauner, T. Lohmüller, Optical Membrane Control with Red Light Enabled by Red-Shifted Photolipids. *Langmuir 2022*, 38 (1), 385-393. DOI: 10.1021/acs.langmuir.1c02745

M. F. Ober, A. Müller-Deku, A. Baptist, H. Amenitsch, O. Thorn-Seshold, B. Nickel, SAXS measurements of azobenzene lipid vesicles reveal buffer-dependent photoswitching and quantitative Z→ E isomerisation by X-rays. *Nanophotonics 2022*. DOI: 10.1515/nanoph-2022-0053

M. F. Ober, A. Baptist, L. Wassermann, A. Heuer-Jungemann, B. Nickel, In situ small-angle X-ray scattering reveals strong condensation of DNA origami during silicification. *arXiv preprint 2022* DOI: 10.48550/ARXIV.2204.07385.

Additional scientific achievements

J. D. Bartl, C. Thomas, A. Henning, **M. F. Ober**, G. Savasci, B. Yazdanshenas, P. S. Deimel, E. Magnano, F. Bondino, P. Zeller, L. Gregoratti, M. Amati, C. Paulus, F. Allegretti, A. Cattani-Scholz, J. V. Barth, C. Ochsenfeld, B. Nickel, I. D. Sharp, M. Stutzmann, B. Rieger, Modular Assembly of Vibrationally and Electronically Coupled Rhenium Bipyridine Carbonyl Complexes on Silicon. *Journal of the American Chemical Society 2021*, 143 (46), 19505-19516. DOI: 10.1021/jacs.1c09061

T. Ehm, J. Philipp, M. Barkey, **M. F. Ober**, A. T. Brinkop, D. Simml, M. von Westphalen, B. Nickel, R. Beck and J. Rädler, 3D printed SAXS chamber for controlled in-situ dialysisand optical characterization. *bioRxiv preprint 2022*. DOI: 10.1101/2022.04.19.488724. Under revision at *Journal of Synchrotron Radiation*.

ACKNOWLEDGMENTS

I want to thank my family and friends, especially Julian, Verena, and Vroni for their unconditional support and encouragement during the last years.
Thank you very much, Bert, for being a great PhD supervisor and mentor, for always having an open door, for supporting me during beam times, for giving me good advice, and for giving me a lot of freedom during the last years. I really enjoyed my time as a PhD student in your group!
Special thanks to my collaboration partners Stefanie Pritzl, Theobald Lohmüller, Linh Nguyen, Lea Wassermann, Tim Liedl, Amelie Heuer-Jungemann, Oliver Thorn-Seshold and Adrian Müller-Deku for the good team work and the precious input.
Many thanks to Joachim Rädler for creating such a pleasant and appreciative atmosphere at the chair and for your many years of support.
Thanks to my early readers and colleges, Sirri Batuhan Kalkan, Heinrich Grabmayr and, in particular, Kilian Frank for invaluable feedback.
Thank you, Susanne Kempter and Gerlinde Schwake, for your good company, support and friendship.
Thanks to my students I had the privilege to mentor and whose scientific contributions are included in this work: Cornelia Sattler, Anna Baptist, Christiane Brummer, Simon Fuchs, and Benjamin Ajanović.
Heartfelt thanks to Team France for your help to get into writing.
Last but not least, I want to thank the current and former members of the Nickel group and all the other people that supported me, namely:

Aidin Lak
Alexandra Murschhauser
Andrea Hegele
Benedikt Bichler
Caroline Hartl
Claudia Leonhardt
Charlott Leu
Clemens Liewald
David Konrad
Eva Riedelsheimer
Friederike Ott
Gregor Cevc
Gregor Posnjak
Janina Baldhuber
Janina Römer
Linda Brützel
Margarete Meixner
Margarita Rüter-Stimpfl
Mehmet Öczan
Patrick Reisbeck
Patrick Urban
Peter Röttgerman
Philipp Altpeter
Philip Böhm
Stefan Fischer
Stephan Manus
Susanne Henning
Tamara Ehm
Thomas Nicolaus
and all members of
the Rädler chair and CeNS

CONTENTS

1. INTRODUCTION

Ever since its inception a vision of nanoscience is to control biological processes at a molecular level. A leading idea to gain this control is the design of artificial biomolecular constructs, which are capable to perform specific biomimetic or novel functions. Important applications of so-called 'nanoagents', such as biocompatible nanoparticles, DNA origami objects, and photoswitchable lipid membranes, have an impact on fields such as chemical sensing, bio-labeling, diagnostic devices, drug delivery and other biomedical systems. Visualizing and resolving the nanoagents' structures and arrangements in action is key controlling and optimizing their envisioned operation.

Since their discovery in 1895 by W. Röntgen [2], X-rays have been proven to be an invaluable probe to unravel the structure of crystals as well as non-crystalline samples in physics, material science and biology. Many of those discoveries, like the double helical structure of the DNA [3–5], have revolutionized their field and been rewarded with the Nobel prize. Small-angle X-ray scattering (SAXS) is a technique to resolve nanostructures which provides the unique ability to investigate nano-objects and their assemblies in the solution phase. This is advantageous as complementary techniques like atomic force microscopy (AFM) or transmission electron microscopy (TEM) operate under vacuum conditions. By the nature of reciprocal space SAXS is suited to probe objects in the range of 0.5-200 nm with sub-nanometer precision. Thus, it is an excellent tool for characterizing nanoagents in their aqueous physiological environment. Even though the concept of SAXS was developed in the late 1930's, it still leads to exciting applications in many fields of science today. This is partly derived from a continuous progress of instrumentation, computational methods, and photon detection techniques. Also, the invention of increasingly brilliant X-ray sources for both laboratory-based setups as well as for modern synchrotron beamlines in the last decades enabled the investigation of more and more complex samples in increasingly sophisticated environments. In a similar way, the work presented in this thesis builds on the construction of a state-of-the-art SAXS laboratory setup in the recent past [6] and the pioneering investigation of the static properties of well-dispersed identical nanoagents, such as monodisperse basic DNA origami shapes [7] or nanoparticles placed on DNA origami templates [8]. So-far unexplored intramolecular spacing, swelling and melting as function of ionic strength and temperature, and high order self-assembly of various DNA constructs could be determined [9]. Within this thesis, the SAXS technique is further pushed towards the analysis of polydisperse core-shell particles, time resolved photo-induced processes and complex DNA-silica nanocomposites. This included a careful evaluation of the role of the X-ray beam energy for photoresponsive processes and, more generally, for solution-based SAXS experiments, which has to be very specific for a given ex-

perimental setup and sample (chapter 2). Importantly, the potential benefits of using high-energy X-rays as low-dose probes discussed. Specifically, DNA-coated gold-silver core-shell nanorods were investigated by SAXS and wide-angle X-ray scattering experiments (WAXS) to validate their mono-crystalline synthesis design, determine their size distribution and confirm the presence of a homogeneous DNA shell (chapter 3). The X-ray study on plasmonic gold-silver nanorods is published together with the synthesis method, spectroscopic studies, TEM analysis and theoretical calculations [10]. Next, light-driven thickness changes in photoswitchable membranes were explored (chapter 4). To realize SAXS experiments on photoswitchable membranes with defined illumination conditions, a dual LED light pump - X-ray probe setup was built. This way, X-rays could be used to probe *in operandi*, how light-driven molecular switching translates into a mesoscopic structural response. The membrane thickness was established as readout for molecular switching efficiency. This allows to address the question if structural changes in photoswitchable membranes upon light illumination exploit the full theoretical range or if they can be improved by tailored conditions or stimuli. This revealed an unexpected dependency of photoswitching upon aqueous phase compositions and potential membrane thickness variations twice as large as obtained by purely optical means. Soft X-rays, i.e. lower energy X-rays, are demonstrated to extend the optical control by a process called catalytic switching, which is driven by radicals produced upon low-energy X-ray exposure. This enables more powerful X-ray-based membrane control and underlines the role of high energy X-rays for observation-only soft matter experiments. The research on photoswitchable membranes is part of three publications [11–13]. Lastly, the encapsulation of DNA origami objects in a protective silica shell was monitored in-situ by SAXS over several days (chapter 5). To accomplish this experiment, a new sample holder, which tumbles the liquid probe around the beam axis, was designed to prevent the nanostructures' sedimentation. The constant sample tumbling enabled to study the influence of the silica growth on the DNA origami shape and its inner fine structure for three different prototypic DNA origami objects. This way, a substantial condensation of the DNA origami object induced by one of two silica precursors, prior to its expansion in response to silica deposition was observed and quantified. Furthermore, it was demonstrated that silicification preserves the overall origami shape and its inner find structure in great detail, increases the origami's rigidity and lattice order, and yields a sub-nanometer thin silica coating, which provides an increased thermal stability up to physiological relevant temperatures. Beyond that, a tendency towards the formation of aggregates during the silica coating reaction for DNA origamis with flat surfaces, i.e. for cuboid-shaped objects is found. The research on silica-coated DNA origami is published as preprint [1].

2. THE ROLE OF X-RAY ENERGIES FOR SOLUTION-BASED SMALL-ANGLE X-RAY SCATTERING

2.1. Basic principles of small-angle X-ray scattering

The information presented in this section is based on reference [14–16].

A small-angle X-ray scattering (SAXS) experiment is conceptually simple and requires an X-ray source, a sample and a detector (cf. Figure 2.1). The sample is usually an aqueous solution of well-dispersed biological macromolecules or particles and needs no special processing like crystallisation or isotopic labelling, such as X-ray crystallography or neutron scattering, respectively. The X-rays must be collimated, parallel, and monochromatic and are either generated by a synchrotron or by a laboratory-based X-ray tube. The incident X-rays are scattered elastically, thus the wavelength of the incident and scattered X-rays are identical. Inhomogeneities in the sample solution causes a deviation of the scattered beam with respect to its incident direction. The scattered radiation is detected as a function of the scattering angle in a small cone around the transmitted X-ray beam.

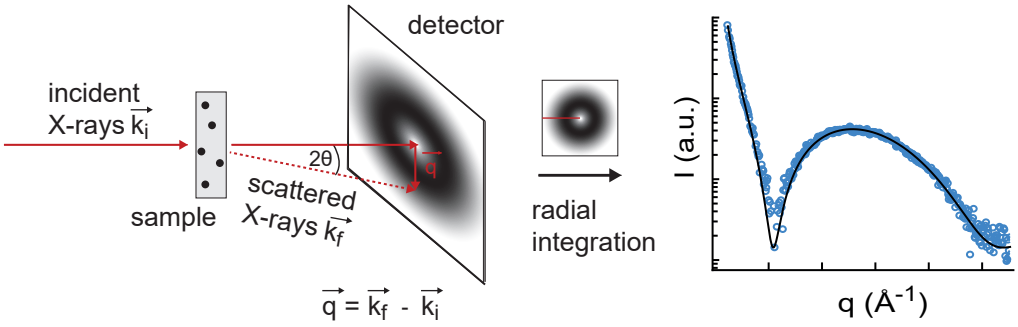

Figure 2.1.: Geometrical scheme of a SAXS experiment. Incident X-rays with wavevector $\vec{k_i}$ pass through the sample solution and are elastically scattered with an angle of 2θ. The scattered X-rays $\vec{k_f}$ are recorded and the resulting isotropic detector image is radially integrated to produce a one-dimensional scattering intensity profile in dependence of scattering vector q.

For a homogenous distribution of the scatterers in solution the detected radiation yields an isotropic and radially symmetric scattering pattern (cf. Figure 2.1). Usually, the data are radially integrated to obtain a one-dimensional curve, in which the scattered intensity I is given as a function of the scattering vector q. q is given by $q = |\vec{q}| = \frac{4\pi}{\lambda}\sin(2\theta(/2))$, where λ is the X-ray wavelength and

2θ the scattering angle between the incident and the scattered beam.
The central measurand of SAXS experiments is defined by the ratio of the incident intensity I_0 and the scattered intensity I_{sc} measured at an angle θ and a distance L on a detector with an area $A_{det} = \Delta\Omega L^2$. This ratio is called the differential scattering cross section of the sample per unit solid angle $\frac{d\sigma}{d\Omega}$ and given by

$$\frac{I_{sc} \cdot L^2}{I_0} = \frac{d\sigma}{d\Omega}. \tag{2.1}$$

Normalization to the unit sample volume V yields the differential scattering cross section per unit sample volume denoted as $\frac{d\Sigma}{d\Omega}$ in units of $[cm^{-1}]$

$$\frac{d\Sigma}{d\Omega} = \frac{1}{V}\frac{d\sigma}{d\Omega}. \tag{2.2}$$

This way, $\frac{d\Sigma}{d\Omega}$ represents the probability of a photon to undergo an elastic scattering event per unit solid angle $\Delta\Omega$ and unit sample volume V. It is a quantitative measure of the X-ray-sample interaction and thus contains sample specific information.
For dilute systems of identical particles, $\frac{d\Sigma}{d\Omega}$ can be calculated via

$$\frac{d\Sigma}{d\Omega} = V_s^{-1} V_p^2 \Delta\rho^2 \left\langle |F(q)|^2 \right\rangle. \tag{2.3}$$

Here, V_p is the particle volume, V_s the sample volume and $\Delta\rho$ is the uniform electron density contrast between the scattering particles and their surrounding solution. $\langle .. \rangle$ indicates the averaging over all possible particle orientations. The measurement of $\frac{d\Sigma}{d\Omega}$ thus provides information on the size, the structure and the shape of the particles averaged over orientation and any size distribution.
The so called particle form factor $F(q) = \left| \int_V \rho(\vec{r}) e^{i\vec{q}\,\vec{r}} dr \right|^2$ is calculated by the square of the scattered wave amplitude. As the scattered wave amplitude has the form of a Fourier transformation of the electron density distribution $\rho(\vec{r})$, the recorded SAXS data and the sample's electron density distribution correspond to reciprocal and real space, respectively.
To obtain the experimental SAXS intensity, $\frac{d\Sigma}{d\Omega}$ has to be multiplied with setup and sample specific scaling parameters and be integrated over the solid angle covered by the detector. The full expression is given by

$$I(q) = \Phi A \varepsilon z T \frac{d\Sigma}{d\Omega}(q). \tag{2.4}$$

The setup specific scaling parameters include the incident photon flux Φ, the beam size A, which is assumed to be smaller than the sample container, and the detector efficiency ε. Sample specific parameters include the sample thickness z and the transmission T.

$$I_{abs}(q) = \frac{d\Sigma}{d\Omega}(q). \tag{2.5}$$

It is advantageous to normalize the measured scattering data to 'absolute scale' $I_{abs}(q)$ in units of $[cm^{-1}]$ by dividing the measured scattering intensity $I(q)$ by all scaling parameters (see Equation 2.5). This way, the measured intensities are related to the differential cross section of the sample, which allows comparison of SAXS measurements conduced at different setups. It further enables the determination of the molecular mass via Equation 2.6, as $\frac{d\Sigma}{d\Omega}(q)$ can also be expressed in dependence of the mass concentration c, the molar mass M, and the scattering constant K.

$$\frac{d\Sigma}{d\Omega}(q) = cKM\left\langle |F(q)|^2 \right\rangle \tag{2.6}$$

The X-ray beam energy neither enters the Equation for the differential measured SAXS intensity (Equation 2.5) nor the cross-section (Equation 2.3) directly, but it influences many experimental parameters, such as the optimal sample thickness, the accessible q-range and the deposited dose in the sample. Thus, the role of X-ray beam energies for solution-based SAXS experiments is outlined in the next section.

2.2. Optimal experimental parameters as a function of X-ray energy

For solution-based SAXS experiments X-ray energies range typically from 4-20 keV and the most commonly used are close to Cu K_α radiation (8 keV) [17]. However, the choice of X-ray beam energy for SAXS has to be very specifically for a given experimental setup and sample, because the X-ray energy influences key parameters of the source as well as the detection system and the interaction of X-rays with the sample. In the following the role of X-ray beam energies for important experimental parameters and the potential benefits of using higher-than-usual energies are discussed.

2.2.1. *Sample thickness*

The parameter in Equation 2.5 directly influenced by the X-ray beam energy E is the sample transmission T, which is calculated via the Lambert-Beer law $I_0 = I(z)e^{-z\cdot\mu(E)}$. Here, $\mu(E) = \lambda(E)^{-1}$ is the energy dependent attenuation coefficient and the inverse of the attenuation length $\lambda(E)$. As the transmission T depends on the sample thickness z, too, the maximum of the measured SAXS intensity is achieved by maximizing the product of both: max ($I_{measured}$) = max(zT) (cf. Equation 2.5).

$$max(zT) = max(z\cdot e^{-z\cdot\mu}) \rightarrow z \stackrel{!}{=} \mu^{-1} = \lambda \tag{2.7}$$

Thus, the maximum intensity is reached for an optimal sample thickness, which corresponds to the attenuation length $\lambda(E)$ (cf. calculation 2.7). This way, for each SAXS beam energy exists an optimal sample thickness.

Figure 2.2 a shows the attenuation length in dependence of the X-ray beam energy for water (solid line) and chloroform (dashed line). For samples diluted in water the optimal sample thicknesses

are z≈1 mm, z≈10 mm, and z≈50 mm for an energy of 8.0 keV, 17.4 keV and 54 keV, respectively (solid lines, Figure 2.2 a). In this context considerations about the required sample volumes are important. For rare and expensive samples the requirement of sample thicknesses >2 mm and thus large volumes can be a major drawback for higher energy SAXS experiments, as those might not be available or result in reduced sample concentrations.

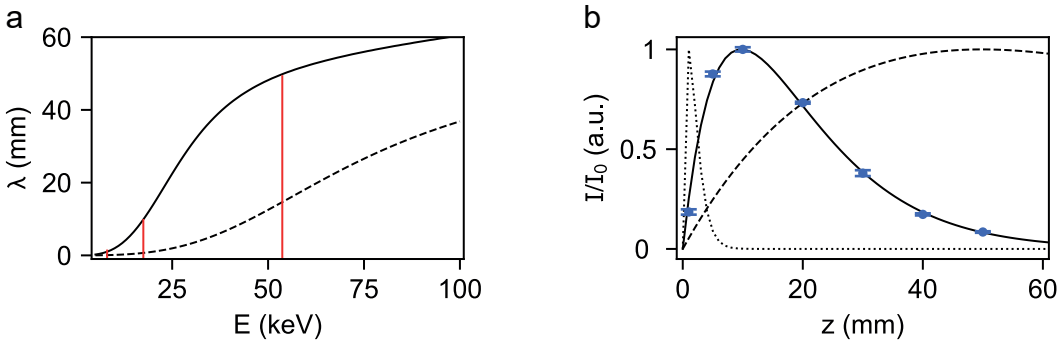

Figure 2.2.: a. Energy dependent attenuation length λ(E) for water (solid line) and chloroform (dashed line). Optimal sample thickness for 8.0 keV, 17.4 keV and 54 keV are highlighted in red. b. Relative scattering intensity I/I_0(z) as function of sample thickness z for 8.0 keV (dotted line), 17.4 keV (solid line) and 54 keV (dashed line). I/I_0 of lipid vesicles measured in sample chambers of varying lengths at a laboratory Mo-source (17.4 keV) are shown as blue dots.

However, large sample thicknesses and volumes are an asset for the installation of complex sample environments involving temperature control, light illumination or control of a chemical reaction, due to a spacious environment (cf. Figure 2.3) [7, 11, 18]. Thus, the choice of the beam energy plays an important role when it comes to the specifics of a sample or its experimental environment. A potential benefit of using higher X-ray energies is the penetration depth, which increases with increasing energy (compare Figure 2.2 a). Thus, for highly absorbing solvents such as chloroform, optimal sample thicknesses are in the submillimeter range for X-ray energies of 8.0 keV and 17.4 keV, whereas the optimal sample thickness for 54 keV is z≈15 mm. This is relevant for SAXS measurements of highly absorbing materials or particles dissolved in highly absorbing solutions as sample chambers in the submillimeter range with sufficiently thin walls are not commercially available [19].

Lastly, the relative scattering intensity I/I_0 is discussed. It is calculated via Equation 2.8 and depicted as a function of the sample thickness z in Figure 2.2 b for 8.0 keV (dotted line), 17.4 keV (dashed-dotted line) and 54 keV (dashed line).

$$\frac{I(z)}{I_{max}} = \frac{ze^{-z/\lambda}}{\lambda e^{-1}} \tag{2.8}$$

Clearly, for 8.0 keV the relative scattering intensity exhibits a sharp maximum and drops fast with increasing z. The higher the beam energy, the broader the maximum of relative scattering

intensity becomes. For example, halving the optimal sample thickness results in 82 % of the maximum scattering intensity for 17.4 keV, and only 50 % for 8.0 keV. To verify the effects of sample thickness experimentally, we studied 2-oleoyl-sn-glycero-3-phospho-L-serine (SOPS) large unilamellar lipid vesicle (LUV) solutions of varying sample thickness at a laboratory Mo-source. The relative scattering intensity was obtained by integrating the background corrected 2D image for a constant q-bin (cf. Figure 2.2 b, blue dots) and it agrees perfectly with the theoretical curve. Hence, higher X-ray energies ensure some flexibility in sample thickness, which especially important for non-standard sample environment devices as shown in Figure 2.3.

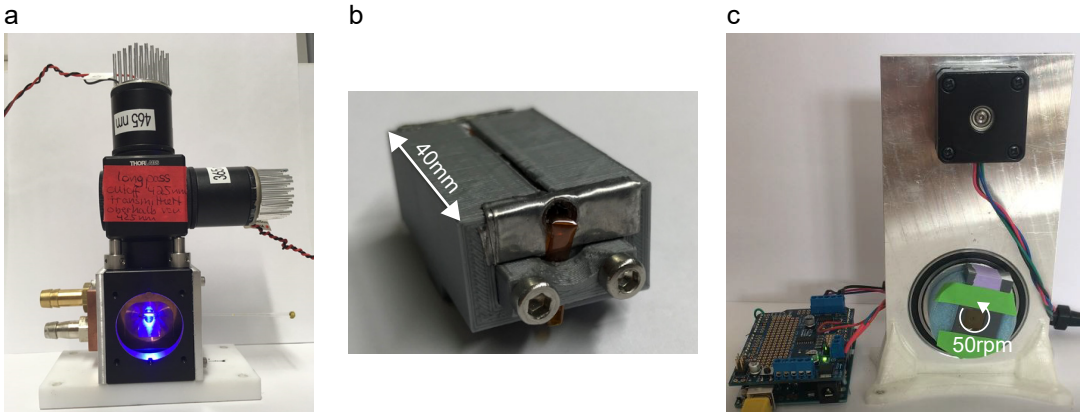

Figure 2.3.: Photographs of specialised sample environments used for SAXS experiments conducted in this thesis. a. Dual LED pump and X-ray probe setup with temperature control making use of a 2 mm Quartz glass capillary for SAXS on photoswitchable membranes. b. 40 mm long Kapton tube installed in a 3D printed sample holder for solution-based high energy SAXS experiments. c. Apparatus for tumbling 10 mm thick SAXS sample chambers with a constant speed of 50 rpm. This way, sedimentation of heavy nanoparticles can be prevented. Here, the tumbler was used for monitoring silica growth on DNA origami objects over several days.

2.2.2. *Q-range*

The X-ray beam energy must also be selected with regard to the q-range to be covered. The scattered intensity is detected as a function of momentum transfer $q = \frac{4\pi}{\lambda}\sin(2\theta/2)$. Here 2θ is the scattering angle and λ is the X-ray wavelength, which is related via $E = \frac{hc}{\lambda}$ to the beam energy. Due to this relation it is obvious to use low beam energy to access small q-values. This is crucial for large particles or intraparticle dimensions D_{max}, which relates to the minimal q-value $q_{min} < 1/D_{max}$ [16]. However, higher beam energies enable data recording to larger q-values for the same scattering geometry. Therefore, they are traditionally used for wide angle scattering (WAXS) on highly absorbing materials, e.g. on metallic nanoparticles (cf. section 3). Also in this thesis high energy WAXS is used to complement a detailed SAXS analysis of plasmonic gold-silver nanorods and determine their crystal structure as demonstrated in chapter 3.2.1.

In the newly evolving field of total scattering, energies up to 100 keV are standard to cover the

necessary q-range [20]. For BioSAXS applications the maximum q-value q_{max} is determined by the inner particle resolution required. Here, repeated inner distances might cause small peaks in the SAXS data and can be read off from peak positions via $q = \frac{2\pi}{d}$ typically in the q-range $0.1\,\text{Å}^{-1} < q < 0.5\,\text{Å}^{-1}$ [7] (cf. chapter 5).

To some extent it is possible to compensate the loss in q_{min} due to the usage of higher X-ray energy with an increased SDD as $q_{min} \propto \frac{1}{\lambda}\frac{1}{SDD}$ or a smaller beam and beamstop. The latter entails a decreased incoming photon flux, whose consequences are discussed in section 2.2.6. However, increasing the SDD could also reduce data quality, as the measured intensity scales with the solid angle Ω of a detector pixel, which is calculated via $\Omega = A_{px}/SDD^2$ for a fixed pixel size A_{px}. Thus, increasing the SDD might improve the minimal q-value and with it the particle resolution, but provides the disadvantage of significantly reduced measured SAXS intensity per pixel as exemplary shown in Figure 2.4 for a DNA origami object. Here, two SAXS data sets from 24 helix-bundles (24-HBs), recorded at a Mo-source laboratory setup, are given (cf. Figure 2.4 inset). The experiments were carried out at different SDDs, 0.97 m (blue triangles) and 2.55 m (orange squares), under otherwise identical conditions. We observe that the lengthening of the SDD by a factor 2.6 yields an improved minimal q-value of $q_{min}^{SDD=2.55\,m} = 0.0068\,\text{Å}$ compared to $q_{min}^{SDD=0.97\,m} = 0.0150\text{Å}$, but a mean intensity loss by a factor of ~ 7.

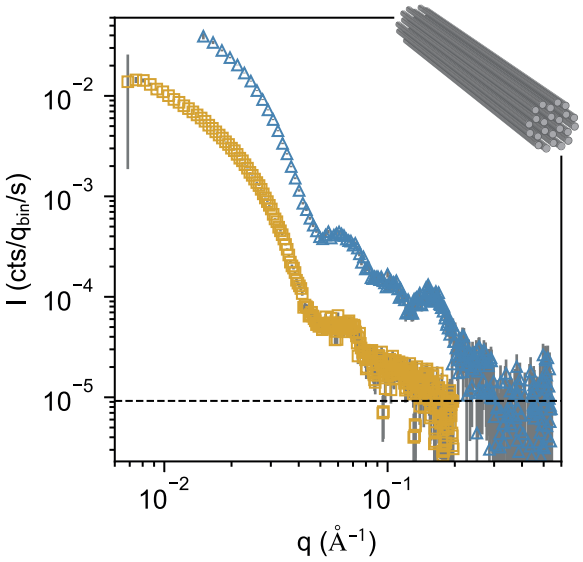

Figure 2.4.: SAXS intensities I(q) of a cylinder-shaped DNA origami object (inset) in (cts/s/q_{bin}) recorded at two different sample-to-detector distances, i.e. 2.55 m (orange squares) and 0.97 m (blue triangles). The background level is highlighted as dashed black line.

The observed background level (Figure 2.4, dashed line) is dominated by the natural background of cosmic rays as well as alpha decay and air scattering. Both contributions are not influenced by the SDD. Thus, not only the measured intensity per pixel but also the signal-to-noise is significantly

reduced for increased SDDs. This is further visible in Figure 2.4 as the second cylinder oscillation at $q \approx 0.10\,\text{Å}^{-1}$ and the Lorentzian shaped interhelical peak at $q \approx 0.16\,\text{Å}^{-1}$ are not resolved for the data set recorded with a SDD of 2.55 m, although the corresponding q-range is covered. Hence, this data underline that the gain in small q-values and the corresponding decrease in scattering intensity results in a substantial loss of structural information. In particular both, the resolution of the overall cylindrical origami shape and its inner structure are affected.

2.2.3. *Q-uncertainty*

Several instrumental parameters, like beam divergence, beam size, sample thickness and pixel size contribute to an uncertainty in the scattering vector Δq. As the optimal sample thickness is strongly energy dependent, its impact on Δq must be discussed in the context of the X-ray energy's choice.

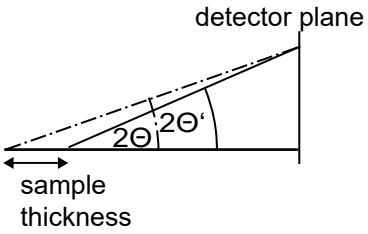

Figure 2.5.: Graphical scheme of the smearing effect caused by sample thickness.

The uncertainty in q results in smearing effects causing reduced definition, or sharpness, in the observed scattering pattern. As a result polydispersity or finite crystallite sizes might be overestimated in SAXS or WAXS measurements, respectively [21, 22].

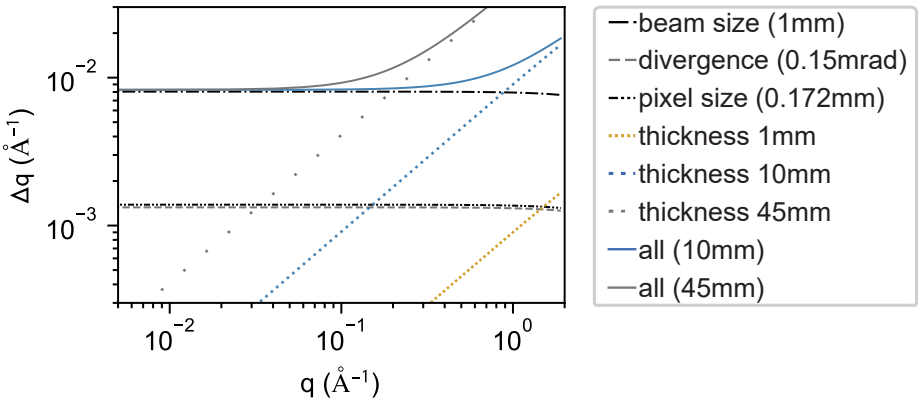

Figure 2.6.: Contributions to the q-uncertainty Δ q(q) for a beamsize of 1 mm (dashed dotted line), beam divergence of 0.15 mrad (dashed line), pixel size of 0.172 mm (dashed double dotted line), sample thickness of 1 mm (densely dotted), sample thickness of 10 mm (dotted), sample thickness of 45 mm (loosely dotted) and all contributions added for 10 mm (solid blue line) and 45 mm sample thickness (solid grey line). The values are calculated for 17.4 keV and 1.1 m SDD.

Here, Δq is shown for different contributions, i.e. beam size (dashed dotted line), divergence (dashed line) and pixel size (dashed double dotted line), as well as the behaviour for a sample thickness of 1 mm (densely dotted), 10 mm (dotted), and 45 mm (loosely dotted). The resulting uncertainty Δq taking into account all contributions (blue and grey solid line), is not effected by the sample thickness for small q-values. However, the uncertainty is considerably influenced starting from a value of $q = 0.3\,\text{Å}^{-1}$ for a sample thickness of 10 mm and $q = 0.06\,\text{Å}^{-1}$ for a sample thickness of 45 mm (see Figure 2.6).
Hence, the smearing effect caused by thick sample chambers is crucial in the WAXS regime and has a notable effect in the SAXS region for extreme samples lengths required for high energy SAXS [21].

2.2.4. *X-ray dose and scattering signal*

The X-ray dose is a result of secondary electrons caused by, firstly, photoelectric absorption of incident X-rays, and secondly, X-ray energy loss due to Compton scattering, which are two of three major interaction processes between X-rays and matter. Elastic, so-called Rayleigh scattering, leaves the photon energy unaltered and is utilized for most scattering techniques including SAXS. The energy dependent cross-sections, i.e. the probability of a photon to undergo a Rayleigh, Compton or photoelectric absorption event, is given in Figure 2.7. Importantly, decreases the probability for a photoelectric absorption event (Figure 2.7, dotted line) strongly for increasing X-ray energies.

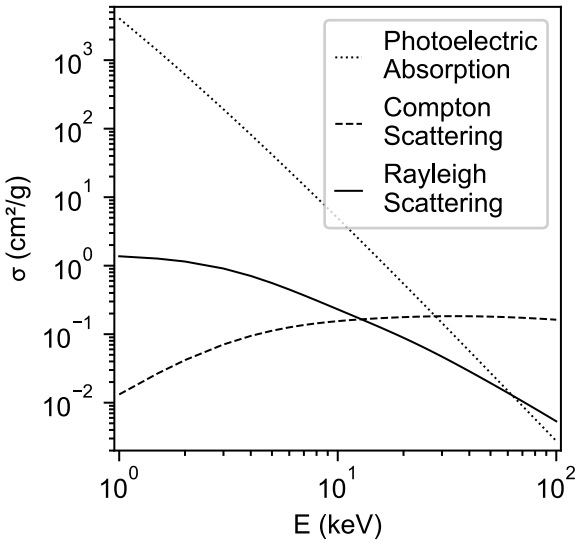

Figure 2.7.: Cross-sections σ (E) of different interaction types of X-rays with water as function of incident beam energy: Rayleigh (solid line), Compton (dashed line), and photoelectric absorption (dotted line). These tabled cross-sections are taken from the NIST XCOM database [23, 24].

Thus, a serious drawback of the conventional X-ray beam energy regime of 4-20 keV for BioSAXS is the high amount of X-ray dose applied to the sample, causing rapid radiation damage if not protected. One difficulty for a BioSAXS experiments lies in the high solvent proportion of biological samples. Upon X-ray exposure, water produces hydroxyl, hydroperoxyl radicals, and solvated electrons by the radiolysis of water. Such reactive species can trigger damage in biological like proteins, tissue or cell membranes rapidly [25]. The damage manifests itself often as irreversible sample aggregation, but also as fragmentation or increased stacking disorder [26–28]. At high flux sources the exposure time and therefore the amount of scattering signal that can be obtained before a sample degrades is limited by the X-ray dose [29]. Of course, there are well-established workarounds to resolve this problem. Flow-through cells ensure minimized X-ray exposure to any given sample volume via flowing or oscillating the sample solution [30]. Cryo-cooling [31] or radioprotective additives such as vitamins [32] are other strategies to increase the dose tolerance of the sample. Numerical calculations as well as scattering curve similarity test procedures have been developed to quantify a radiation damage onset. Scattering profiles recorded after this onset are dominated by X-ray induced conformation changes and of no further use for structural analysis [33, 34].

Nevertheless, these approaches are not constructive for some experimental setups or materials. To study, for example, the formation and growth of nanoparticles by X-ray scattering over time, must the reaction solution stir in a bulk container without additives, oscillation, or cooling [18, 35–37]. Thus, none of the above described workarounds such as flow-through techniques or the addition of radioprotective substances, are suitable to minimize the deposited X-ray dose for such an experiment. Within this thesis two more SAXS experiments are described, where common workarounds to reduce the amount of X-ray dose fail. First, light-pump and X-ray-probe experiments with photoactive materials. Here, it must be ensured that the X-ray probe is not compromising the photophysics of the system as outlined in chapter 4. Second, a long-term in-situ SAXS experiment, which monitored the encapsulation of DNA origami objects in a protective silica shell (cf. chapter 5) was conducted over several days. Such a long time period of X-ray exposure could potentially deposit a huge amount of dose to the sample.

As demonstrated in this thesis, can the use of higher X-ray energies for SAXS contribute to resolve these issues by taking advantage of the decreasing probability of photoelectric absorption with increasing incident energy, see Figure 2.7. A simple analytic dose calculation can be performed under the conditions of the so-called *charged particle equilibrium*, which applies well to the case of a broad, parallel and monochromatic X-ray beam [27, 38]. Thus, the absorbed dose rate within a sample of volume V, density ρ, and its attenuation length λ, is calculated via Equation 2.9 [38].

$$D = \frac{E_T}{m} = \frac{I_0 E t \left(1 - e^{-\left(\frac{\mu_{ic}}{\rho}\right)\rho\lambda}\right)}{V\rho} = \frac{I_0 E t \left(1 - e^{-\left(\frac{\mu_{ic}}{\rho}\right)\rho\lambda}\right)}{A\lambda\rho} \tag{2.9}$$

Here, E_T is the transferred energy per mass m, I_0 the beam intensity, E the X-ray energy, t the

exposure time, and $\frac{\mu_{ic}}{\rho}$ the incoherent contribution to the mass attenuation coefficient, i.e. the Compton and the photoelectric contribution.

In Figure 2.8 the tabulated energy dependence of the X-ray dose for water is shown, calculated for an optimal sample transmission of 37 % and an exemplary X-ray beam using the mass attenuation coefficients provided by the NIST XCOM database [23]. As evident from Figure 2.8 the absorbed dose drops drastically for increasing energies in the regime of 5-30 keV as does the photoelectric absorption cross-section (see Figure 2.7). After a minimum of 36 keV, the dose rate shows a mild increase for energies larger than 40 keV. This arises because of the Compton scattering cross-section's increase with increasing energy (Figure 2.7, dashed line) and becoming larger as the photoelectric absorption (Figure 2.7, dotted line) at above ≈27 keV. Such considerations clearly point to favourable X-ray energy regime of 30-42 keV for SAXS experiments, in which the deposited X-ray dose must be limited to avoid radiation damage of the sample.

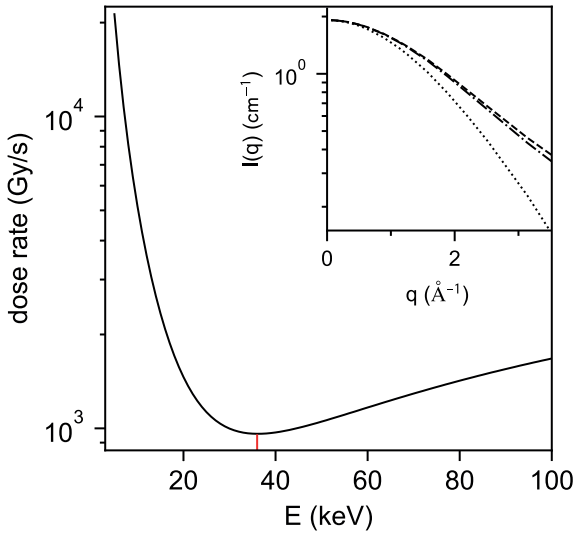

Figure 2.8.: Energy dependent dose rate for water calculated for an optimal sample transmission of 37 % and a beam flux of 10^{12} cts/s/mm^2. The dose rate minimum of 36 keV is highlighted in red. The inset shows the Rayleigh scattering intensity, i.e. the SAXS signal on absolute scale I(q) in (cm^{-1}), for a carbon scattering centre for X-ray energies of 8 keV (dotted line), 17 keV (dashed-dotted line) and 54 keV (dashed line).

Although, the probability of an elastic scattering event decreases with increasing X-ray energy (see Figure 2.7, solid line), the use of higher X-ray energies for SAXS does not per se imply a loss scattering signal. In fact, the amount of scattered photons is in the limit of small angles independent on the X-ray beam energy. In order to explain this, the SAXS intensity for a carbon scattering centre is calculated for three different X-ray beam energies 8.0 keV, 17.4 keV, and 53.7 keV via Equation 2.10 and 2.11 and plotted in dependence of the scattering vector q as dotted, dashed-dotted, and dashed line as inset in Figure 2.8.

To match the conditions of the X-ray beams used for the SAXS experiments presented in this

thesis, the intensities for 8 keV and 53.7 keV are calculated under the assumption of a horizontal polarized X-ray beam as typical for synchrotron SAXS beamlines. The intensity for 17.4 keV is calculated for an unpolarized X-ray beam delivered by an X-ray tube. The intensity of a SAXS experiment on absolute scale $I_{abs}(q) = \frac{d\Sigma}{d\Omega}(q)$, i.e. without scaling parameters, is given by the differential Rayleigh cross-section $\frac{d\sigma_R}{d\Omega}$, i.e. the detection probability of an elastically scattered photon per unit solid angle as well as the number density ρ of scatterers (see Equation 2.10). The Rayleigh cross-section (Equation 2.11) is calculated via the Thomson radius is denoted as r_e, $f(\theta)$ is the atomic form factor, and P the polarization of the X-ray beam. From the inset of Figure 2.8 and Equation 2.12 it is readily apparent that there is almost no difference in the number of elastically scattered photons within the limit of small angles, i.e. the SAXS regime $(0-0.5\text{Å}^{-1})$.

$$I_{abs}(q)[cm^{-1}] = \rho \frac{d\sigma_R}{d\Omega} \tag{2.10}$$

$$\frac{d\sigma_R}{d\Omega} = r_e^2 P(\theta)|f(\theta)|^2 \tag{2.11}$$

$$\frac{d\sigma_R}{d\Omega}(\theta \to 0) = r_e^2 P(0)|f(0)|^2 \tag{2.12}$$

Hence, the SAXS scattering signal does not change with the incident beam energy. Moreover, the same considerations are true for the differential Compton scattering cross-section within the SAXS regime, i.e. in the forward scattering limit of small angles is the amount of Compton photons independent on the X-ray energy. Thus, the use of higher energy does not result in additional SAXS background due to Compton scattering.

2.2.5. *X-ray detectors*

The latest generation of X-ray detectors are based on a hybrid photon counting (HPC) technology by which X-rays are directly registered through absorption of the photons by a semiconductor sensor material. This way electron-hole pairs and a charge proportional to the X-ray energy are generated. While the charge measurement and its processing occurs in the readout component of the hybrid pixel, the electrical charge conversion takes place in the sensor pixel component. The most common sensor material used in detectors at SAXS beamlines is silicon. This is often the limiting factor when it comes to the choice of X-ray beam energy, as the absorption of higher X-ray energies is drastically reduced even for thick silicon sensors and, hence, the X-ray detection registration diminished.

The energy dependent changes in quantum efficiency (QE), which are calculated for single photon counting PILATUS detectors following the approach of Marchal et al. [39], are shown for silicon sensors with two thicknesses and a cadmium telluride (CdTe) sensor in Figure 2.9. For Cu radiation, i.e. a beam energy of 8 keV, a QE of 97 % is reached by the usage of a 320 µm thick silicon

sensor (Figure 2.9, solid black line). For Mo radiation (17.4 keV) such a sensor would only yield a QE of 38 %. Using an increased silicon sensor thickness (Figure 2.9, dashed black line) improves the detection efficiency for 17.4 keV up to 76 %. But even a 1000 µm thick silicon sensor does not yield a QE above 50 % for energies higher than 20 keV.

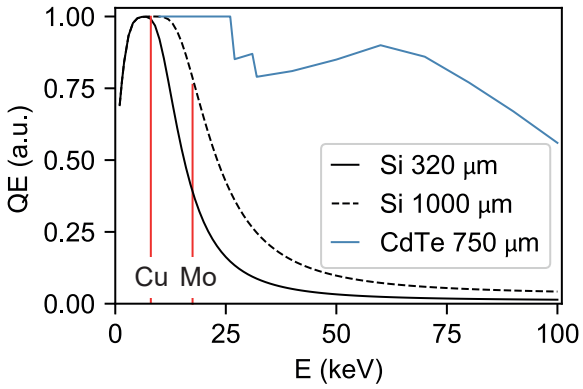

Figure 2.9.: Calculated quantum efficiencies QE(E) of single photon counting PILATUS detectors with silicon (black lines) or cadmium telluride sensor materials (blue line) of various thicknesses as a function of beam energy. The QE is calculated by the absorption of incident X-rays in the sensitive volume of the sensor using mass attenuation coefficients from the NIST XCOM database [23]. Common X-ray energies used for SAXS, Copper (8 keV) and Molybdenum (17.4 keV) radiation, are highlighted in red.

However, other sensor materials like Ge, GaAs and CdTe, exhibit significantly better QE in the high energy regime up to 100 keV, with large CdTe detectors (Figure 2.9, blue line) becoming now commercially available [40]. The use of CdTe instead of Si crystals increases the QE of X-ray detectors in the high energy regime substantially (cf. Figure 2.9).

2.2.6. *Photon flux*

The measured scattering intensity (cf. Equation 2.5) is directly proportional to the photon flux Φ. Thus, high fluxes result in improved signal-to-noise for SAXS data, enhance the resolution and provide more accurate measurements at higher angles. Additionally, high fluxes enable short data-acquisition times [41] or low sample concentrations [42], which in turn can prevent sedimentation or aggregation of the sample.
As a demonstration, two different SAXS pattern of a DNA origami object, the 24-HB (cf. Figure 2.10 inset) are superimposed in Figure 2.10. First, the SAXS measurement was performed at a laboratory setup, providing a photon flux of 1.8×10^6 cts/s/mm^2 (Figure 2.10, orange squares). Second, the experiment was repeated at a high flux SAXS beamline at Elettra, which provided a photon flux of 5×10^{12} cts/s/mm^2 (Figure 2.10, blue triangles).

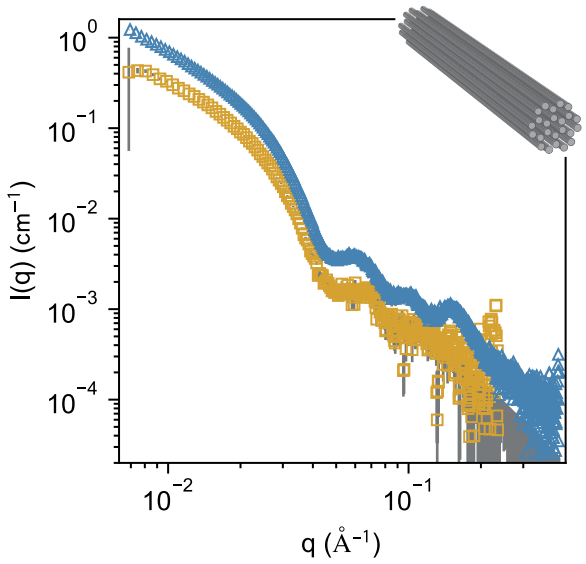

Figure 2.10.: Two different SAXS experiments on a cylinder-shaped DNA origami object are performed at a high photon flux beamline with 5×10^{12} cts/s/mm^2 (blue triangles) and at a laboratory SAXS setup with 1.8×10^{6} cts/s/mm^2 (orange squares), respectively. The laboratory SAXS intensities are vertically offset for clarity.

The high flux SAXS experiment provides clearly an improved signal-to-noise ratio, especially for higher q-values. Thus, a large difference in the distinctness of the 24-HB oscillations exhibiting minima at $q \approx 0.05\,$Å and $q \approx 0.08\,$Å are visible. The peak at $q = 0.16\,$Å, which corresponds to the interhelical distance of the 24-HB is only visible in the high flux data. However, the difference in the background level can not be attributed to differences in the photon flux, but might result from a small non-evacuated part of the flight tube and increased level of natural background for the laboratory data. Nevertheless, this experiment demonstrates the importance of photon flux for high resolution SAXS experiments.

Beamline	Insertion Device	Energy Range	Φ_{max}
SAXS @ Elettra	57-pole wiggler	5.4, 8.0, 16 keV	$10^{13}\,\frac{cts}{s}$ @8 keV
P08 @ DESY	undulator	5.4-29.4 keV	$2 \times 10^{12}\,\frac{cts}{s}$ @ 5.4, 8, 14 keV
P03 @ DESY	undulator	9-23 keV	$5 \times 10^{11}\,\frac{cts}{s}$ @13 keV
P21 @ DESY	undulator	52, 85, 100 keV	$2 \times 10^{11}\,\frac{cts}{s}$ @100 keV
Mo-source laboratory setup		17.4 keV	$2 \times 10^{6}\,\frac{cts}{s}$

Table 2.1.: Exemplary beamline parameters: insertion device, energy range and maximum photon flux [43–46].

At synchrotron light sources the photon flux depends on a vast set of parameters like the storage ring energy, the properties of insertion devices, i.e. wigglers or undulators, and the upstream X-ray optics. As a result, the photon flux generated at third generation synchrotron beamlines does

not exhibit a particular dependence on the X-ray energy, however, there is a trend for decreasing flux with increasing energy as evident from Table 2.1. For laboratory SAXS setups with sealed X-ray tubes the flux decreases with increasing K_α energy, i. e. the atomic number of the anode materials [47].

2.2.7. *Coherence*

The longitudinal and transversal coherence lengths are two more X-ray beam parameters, which are of great importance to resolve the size of an object. Coherence in X-ray scattering enables the constructive interference of pairs of electrons, because the phase differences between them have definitive values, which are constant in time.
Transversal coherence length ξ_t considers the phase at a transversely separated pair of scatterers. It is determined by collimation and as such a property of the source and the X-ray optics. It is calculated via Equation 2.13 and limited by the divergence 2θ of the X-ray beam [14, 48].

$$\xi_t = \frac{\lambda}{2\tan\Delta 2\theta} \approx \frac{\lambda}{2\Delta 2\theta} \tag{2.13}$$

Longitudinal coherence ξ_l is determined by monochromaticity and calculated via Equation 2.14.

$$\xi_l = \frac{\lambda^2}{2\Delta\lambda}; \tag{2.14}$$

Hence, the accessible longitudinal resolution s for an object with size a is determined by the bandwidth, i.e. the energy resolution, and can be read off Equation 2.15 [14, 48].

$$\frac{\lambda}{\Delta\lambda} < \frac{s}{a} \tag{2.15}$$

Estimated coherence lengths for different beamlines and X-ray energies are listed in Table 2.2. As evident from Equation 2.13 and 2.14 both coherence lengths are inversely proportional to the X-ray energy, however, the divergence and the bandwidth play a far more important role.

Coherence	ElettraSAXS (8 keV)	P03 (13 keV)	Mo-source (17.4 keV)	P21.1 (54 keV)
transversal	450 nm	11500 nm	240 nm	2000 nm
longitudinal	150 nm	240 nm	6 nm	11.5 nm

Table 2.2.: Estimated coherence lengths for different beamlines and beam energies [44, 46, 49].

3. DNA-FUNCTIONALIZED GOLD-SILVER CORE-SHELL NANORODS

The work in this chapter has been partly published in [10].

Metallic nanoparticles (NPs) or comprising complexes, with dimensions smaller than the wavelength of light can exhibit exceptional optical properties. Their strong interactions with light is a result of localized surface plasmon resonance, i.e. the coupling of electromagnetic waves to collective oscillations of free electrons in metals, when exited with light of a specific wavelength. This phenomenon is illustrated for a spherical metallic NP with an incoming electromagnetic field E_{in} in Figure 3.1.

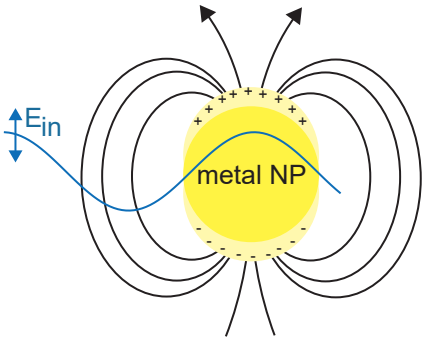

Figure 3.1.: Schematic illustration of localized surface plasmons for a nanosphere in response to the interaction with an incoming electromagnetic field.

One way to describe a localized surface plasmon mathematically is the simplified Mie formula (see Equation 3.1), which calculates the extinction (absorption and scattering) cross section for a nanosphere with radius r that is exited by light with wavelength λ under the condition ($2r << \lambda$).

$$\sigma_{ext}(\omega) = 9\frac{\omega}{c}\varepsilon_m^{\frac{3}{2}} VN \frac{\varepsilon_2(\omega)}{(\varepsilon_1(\omega)+2\varepsilon_m)^2+\varepsilon_2(\omega)^2} \tag{3.1}$$

Here, ω is the incident light angular frequency, $\varepsilon(\omega) = \varepsilon_1(\omega) + i\varepsilon_2(\omega)$ is the dielectric constant of the metal nanosphere, ε_m the dielectric constant of the surrounding solvent, $V = 4/3r^3\pi$ the nanosphere's volume and N the number density of the NPs. The maximum of optical extinction is achieved if the so-called resonance condition 3.2

$$\varepsilon_1(\omega) = -2\varepsilon_m \tag{3.2}$$

is fulfilled. From Equation 3.1 and 3.2 it becomes clear that absorption and scattering properties can be can be manipulated by controlling particle size, shape, material composition or changes in the surrounding medium [50–52].

The synthesis of well-defined NPs with distinct plasmon scattering has led to the development of new techniques in the field of advanced spectroscopy methods [53], label free biosensing [50, 54, 55] or optical data storage [56]. The DNA origami technique provides, due to its programmability, a powerful addition as it allows to organize metal NPs with high spatial precision. Manipulation of interparticle distance and their orientation is key to tailor the plasmonic characteristics of these NP-DNA complexes [57]. For example, the electromagnetic field in the gap region of a strongly coupled NP pair, a so-called hot spot, can be drastically amplified [58]. Such a hot spot configuration of metal NPs enables an extraordinary enhancement factor for Raman spectroscopy signals large enough for single molecule detection [59]. The DNA origami technique further enables the arrangement of plasmonic NPs in chiral geometries, e.g helices, such that strong circular dichroism signals can be triggered and exploited for sensitive analyte detection [60, 61].

Nanorods in contrast to nanospheres, exhibit additional shape dependent optical behavior mainly through variations of the aspect ratio. Due to their anisotropic shapes, their localized surface plasmon resonances cover the visible spectrum to the infrared, exhibit localized field enhancement and optical nonlinearity effects [62–64].

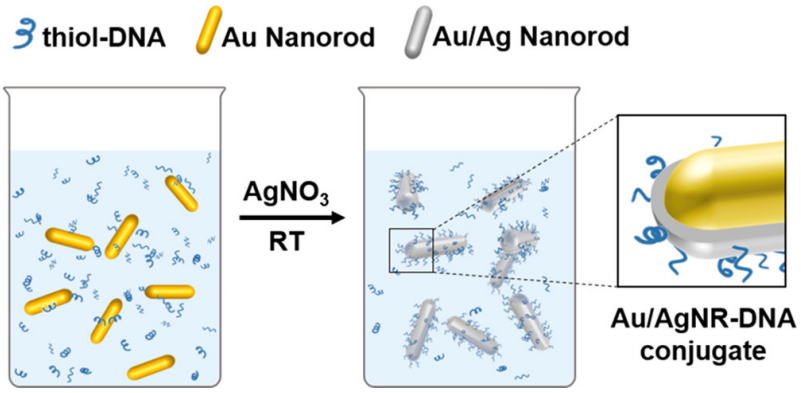

Figure 3.2.: Illustration of the strategy for the one-pot synthesis of DNA-functionalized Au/Ag core-shell nanorods. Taken from [10].

Gold (Au) and silver (Ag) are the most common metals for plasmonics and recent interest has been focused on bimetallic Au/Ag complexes. Plasmonic silver nanoparticles (AgNPs) hold great potential due to possible surface plasmons excitation in the visible region and beyond, and enhanced plasmonic coupling. These properties result in a greater extinction cross-section and ultimately optical performance [65, 66]. In contrast to AgNPs are AuNPs very stable due to oxidation, disintegration and aggregation, easy to synthesize and successfully prepared as DNA-Au NPs complex.

To utilize the complementary advantages of Ag and Au by combing the plasmonic properties of silver with the superior stability of gold, Nguyen et al. developed a method to synthesize highly stable, gold-silver core-shell nanorods, which are functionalized with DNA (Au/Ag NRs@DNA). While the Au core enables the control of aspect ratios and monodispersity, gives the Ag shell rise to more pronounced plasmonic responses, which is demonstrated by a strongly increased circular dichroism. The simple one-pot reaction as illustrated in Figure 3.2 employs thiolated DNA, which binds to the Ag surface. For Ag shell growth, $AgNO_3$ was used as precursor and L-ascorbic acid as reducing agent. As the lattice constants $a_{Au} = 4.0704\,\text{Å}$ and $a_{Ag} = 4.07778\,\text{Å}$ nearly match, epitaxial Ag growth and formation of monocrystalline Au/Ag NP were feasible [67]. Importantly, the extinction spectra and the overall signal strength of Au/Ag NR@DNA could be manipulated by the Ag shell thickness, which in turn could be controlled via the ratio between AuNR and $AgNO_3$ concentration.

3.1. Structure and polydispersity analysis by X-ray scattering

To validate the design of the Au/Ag NR@DNA over a large set of particles, to obtain the structural details as well as their size distribution and degree of cluster formation or aggregation, we performed SAXS experiments on 15 nm x 7 nm AuNRs with a thin Ag shell of 0.5 nm by design, and $polyT_{19}$ as DNA ligand, i.e. a DNA strand with HS-5'TTTTTTTTTTTTTTTTTT3' sequence (T: thymine). Furthermore, the homogeneity and dimensions of the surrounding DNA shell are examined.

3.1.1. *Small-angle X-ray scattering*

Experimental considerations

As Au/Ag NR@DNA conjugates are non-biological samples and thereby not at risk to encounter X-ray induced radiation damage, the choice of the beam energy due to the applied X-ray dose was not critical (cf. section 2.2.4). However, to resolve the NR's height of $\sim 15\,\text{nm}$ a minimum low q-value of $q_{min} = \frac{1}{15nm} = 0.0067\,\text{Å}^{-1}$ was required (section 2.2.2 for details). Also, potential cluster formation and aggregation should be detected, which is visible in the very low q-regime [68]. These considerations pointed in the direction of firstly, soft X-rays, thus longer X-ray wavelengths, and, secondly, a large SDD as $q_{min} \approx 1/(\lambda \cdot SDD)$. As explained in section 2.2.2, the acquired scattering signal is inversely proportional to the square of the SDD and consequently decreases with increasing SDD. However, Au/Ag NR@DNA NPs are strong scatterers, as they consist mainly of high electron density materials ($\rho_{Au} = 119 \times 10^{-6}\,\text{Å}^{-2}$ and $\rho_{Ag} = 77 \times 10^{-6}\,\text{Å}^{-2}$).Therefore, they are, in contrast to most biological samples, feasible for SAXS experiments with large SDD to access to very low q-regime. Simulations of the SAXS intensities using a cylindrical core-shell-shell model as described in 3.2.1 and applying the Au/Ag NR@DNA NPs design values

furthermore suggest a maximum q-value of $q_{max} \approx 0.2\,\text{Å}^{-1}$ to resolve its dimensions. Besides, as outlined in section 2.2.3, low q-uncertainty is an important prerequisite for a valid estimation of polydispersity. Apart from the most decisive requirements for this experiment, i.e. the q-range ($0.004\,\text{Å}^{-1} < q < 0.2\,\text{Å}^{-1}$), low q-uncertainty and non-sensitivity due to the applied X-ray dose, the quality of SAXS measurements would benefit from high photon flux (cf. section 2.2.6.
Hence, we measured with a beam energy of 13 keV at the P03 beamline at Petra III (DESY) in Hamburg and recorded the SAXS data at two detector positions, namely 2.0m and 5.1m from the sample. This way, a q-range of $0.0035\,\text{Å}^{-1} < q < 0.2\,\text{Å}^{-1}$ could be covered. Moreover, P03 provides an exceptionally high photon flux confined to beam size of 0.03 x 0.02mm^2 at sample position with minimal divergence and wavelength spread, fulfilling all requirements due to q-range, high signal-to-noise, low q-uncertainty and required coherence lengths. A Pilatus 1M CMOS detector (Dectris Ltd, Switzerland) with 981 x 1043 pixels with 172 x 172 µm^2 pixel size served as detector, achieving an detection efficiency of $\sim 0.97\,\%$ due to a 1000 µm thick silicon sensor. A good compromise between relative intensity (72 %) and sample volume was achieved by using 1.5mm thick Quartz glass capillaries (Hilgenberg GmbH, Germany) as sample containers.

Cylindrical core-shell-shell model

To extract the dimensions of Au/Ag NR@DNA quantitatively, we establish a model fit assuming cylindrical particles with a Au core and two concentric shells, representing the Ag and DNA shell, respectively, as illustrated in Figure 3.3.
The form factor $F(q)$ was calculated as function of the scattering vector $q = |\overrightarrow{q}| = 4\pi/\lambda \sin(2\theta/2)$, where λ is the wavelength of the X-rays and 2θ the scattering angle, via Equation 3.3

$$F(q) = \sum_{i=1}^{3} \Delta\rho_i V_i \frac{\sin(q\frac{L_i}{2}\cos(\frac{\alpha}{2}))}{q\frac{L_i}{2}\cos(\frac{\alpha}{2})} \frac{2J_1(qR_i\sin(\alpha))}{qR_i\sin(\alpha)} \tag{3.3}$$

with

$$L_1 = L_c; \quad R_1 = R_c; \quad \rho_1 = \rho_c - \rho_{s_1} \tag{3.4}$$

$$L_2 = L_c + d_1; \quad R_1 = R_c + d_1; \quad \rho_2 = \rho_{s_1} - \rho_{s_2} \tag{3.5}$$

$$L_3 = L_c + d_1 + d_2; \quad R_1 = R_c + d_1 + d_2; \quad \rho_3 = \rho_{s_2} - \rho_{buffer}. \tag{3.6}$$

Here, J_1 is the first order Bessel function, α the angle between the cylinder axis and the q-vector, L_c the length of the cylinder core, R the radius of the cylinder core, d_1 the thickness of the first, and d_2 the thickness of the second shell. V_i is the corresponding volume, and ρ_i the scattering length density contrast of the core, the first, and the second shell [69].

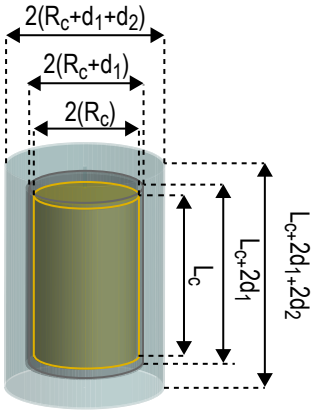

Figure 3.3.: Schematic sketch of a core-shell-shell Au/Ag NR@DNA particle.

As Au/Ag NR@DNA are dissolved in aqueous solution, they are randomly oriented between q and the axis of the cylinder height. The squared form factor must therefore be integrated over all angles between 0° and 90° to ensure orientationally averaged scattering intensity as given in Equation 3.7.

$$I(q) \propto \int_0^{\frac{\pi}{2}} F^2(q,\alpha)\sin(\alpha)\,d\alpha \tag{3.7}$$

To estimate polydispersity (PD) for the core radius and length, a Schulz size distribution as given in Equation 3.8 was applied to those parameters.

$$f(x) = c(z+1)^{z+1}\frac{x}{x_{mean}}\frac{\exp(-(z+1)x/x_{mean})}{x\Gamma(z+1)} \tag{3.8}$$

Here, c is a normalization constant, x_{mean} the distribution's mean value, and z the distributions width, such that the PD is given by $PD = \sigma/x_{mean}$ with σ corresponding to the root-mean-square deviation from x_{mean} [70].
The particle's dimensions are obtained from simultaneous fits to both measured data sets by running a population-based DREAM algorithm using the software package SasView [71]. The scattering length densities of Au ($\rho_{Au} = 119 \times 10^{-6}\,\text{Å}^{-2}$), Ag ($\rho_{Ag} = 77 \times 10^{-6}\,\text{Å}^{-2}$) and the buffer ($\rho_{buffer} = 9.4 \times 10^{-6}\,\text{Å}^{-2}$) were kept fixed during the fitting procedure.

3.1.2. *Gold-silver core-shell nanorods covered by a homogeneous DNA shell*

The SAXS intensities $I(q)$ of Au/Ag NR@DNA, recorded at two different SDDs, are shown in Figure 3.4. It is, firstly, easy to observe that the nanorods (NRs) are well-dispersed, which is indicated by the presence of an intensity plateau at small q-values. A cluster formation or particle aggregation would, in contrast, yield a power-law like intensity increase or a so-called structure factor, i.e. intraparticle correlation peaks, in the low q-regime. The SAXS intensity distribution

exhibits, secondly, distinct oscillations, which confirm a well-defined particle shape.
From the model fit of cylindrical core-shell-shell particles, detailed in section 3.1.1, we obtain a Au core radius of $R_{Au} = 3.4\,\text{nm}$ and a length of $L_{Au} = 15.5\,\text{nm}$. However, the AuNR cores are not monodisperse, but exhibit a distribution in size. We find a PD of $\sim 12\,\%$, corresponding to a variance of the Schultz size distribution of $\sim 0.4\,\text{nm}$ for the Au core radius and a PD of $\sim 29\,\%$, corresponding to a variance of the Schultz size distribution of $\sim 4.5\,\text{nm}$.

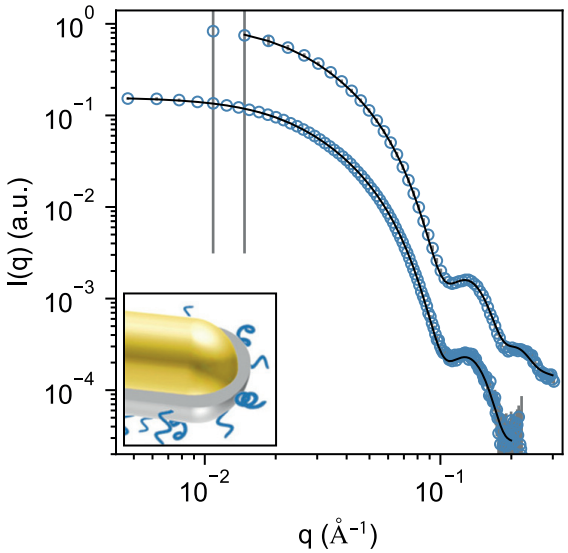

Figure 3.4.: SAXS intensities I(q) (blue circles) with model fits based on a cylindrical core-shell-shell model (solid black lines). Intensities were recorded at two sample positions, 5.1 m and 2.0 m from the sample, and the model was refined to both data sets simultaneously. Intensities are vertically offset for clarity. Inset: Schematic illustration of Au/Ag NR@DNA - adapted from [10].

The comparison with transmission electron microscopy (TEM) images taken from the same batch suggests that especially the PD of the cylinder length arises from a small fraction of spherical Au/Ag @DNA particles in the batch, as indicated with red arrows in Figure 3.5 a,b. Au nanospheres are a common by-product in the synthesis of AuNRs [72, 73]. For the Ag and DNA shell thicknesses, we obtain $d_{Ag} = 0.5\,\text{nm}$ and $d_{DNA} = 2.9\,\text{nm}$, respectively.
In polymer science, the form of anchored polymers and their thickness, depend on their grafting density at the solution/substrate interface σ. Such polymers form either low grafting density 'mushrooms' or high density 'brushes' [74]. Unfortunately, these two regimes can not be easily distinguished by the layer thickness alone, but need an estimation of the distance between grafting points s, which could be measured via UV-Vis spectroscopy [75,76]. In the past, such UV-Vis measurements confirmed highly dense $polyT_{19}$ DNA in the brush regime on Au spheres (5.7 nm) [8]. However, the obtained DNA shell thickness (2.9 nm) for Au/Ag NR@DNA is notably smaller than the thickness of a highly dense configuration and close to the Flory radius (4 nm), which is calculated for $polyT_{19}$ DNA under the assumption of ideal polymer random coils [77]. Therefore,

we speculate that the surface coverage of Au/Ag NR@DNA by DNA is significantly less dense compared to *polyT*$_{19}$ DNA on Au spheres and that the DNA covering the Au/Ag NRs is likely to be in a mushroom or mushroom-brush transition configuration.

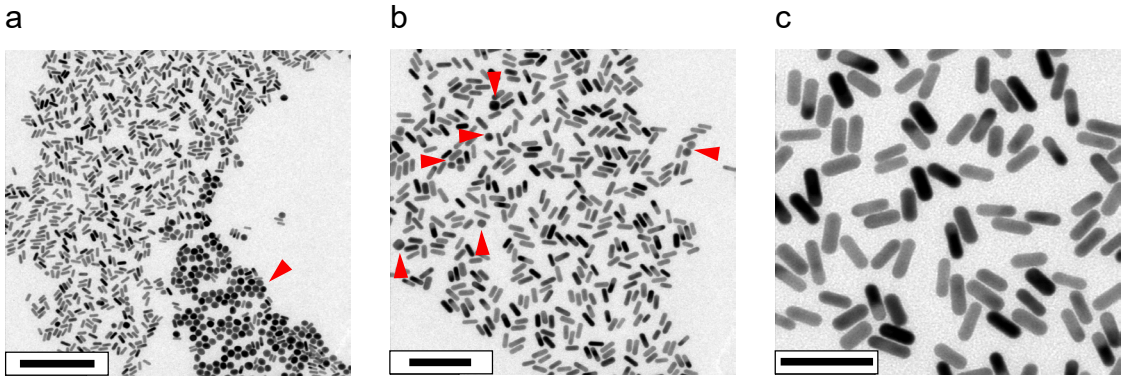

Figure 3.5.: TEM images of Au/Ag NR@DNA designed with 15 nm x 7 nm AuNRs and a thin Ag shell. Red arrows indicate spherical Au/Ag @DNA particles. Scale bars 200 nm (a), 100 nm (b) and 60 nm (c). TEM images were recorded by L. Nguyen.

In summary, the design of the Au/Ag NR@DNA is validated, as all parameters are in good agreement with the dimensions obtained from TEM and the NR synthesis. Although TEM analysis might make the DNA shell visible as a bright halo around the NRs, and the Au and Ag may be distinguished due to their difference in contrast, TEM analysis lacks of unambiguousness, structural details and resolution. Here, SAXS experiments fill this gap by confirming of a ultrathin Ag and a surrounding homogeneous DNA shell and by enabling the determination of their dimensions with Angström resolution.

3.2. Crystal structure and crystallinity analysis by X-ray scattering

The crystal structure and crystallinity of AuNRs, Au/Ag NRs and Au/Ag NR@DNA are investigated and compared by WAXS experiments, to confirm a epitaxial Ag growth on the Au core and the formation of monocrystal Au/Ag NR@DNA.

3.2.1. *High energy wide-angle X-ray scattering*

Experimental considerations

For WAXS experiments on metal NPs higher X-ray beam energies are an obvious choice because they enable data recording over a broad angular range within one measurement (cf. section 2.2.2). As detailed in section 2.2.3, the overall q-uncertainty in the WAXS regime is dominated by the sample thickness caused smearing contribution. Consequently, the sample thickness must be minimized to ensure a precise analysis of the crystal structure. An extremely thin sample with high

NP concentration is achieved by dropping the NP solution on a thin foil and let it dry repeatedly at the same spot. To keep the NRs in solution it is necessary to use stabilizing agents. Here, AuNRs were stabilized with cetyltrimethylammonium bromide (CTAB), Au/AgNRs with a large polymer called polyvinylpyrrolidone (PVP) and Au/Ag NR@DNA were intrinsically stable via the thiol-bond DNA.

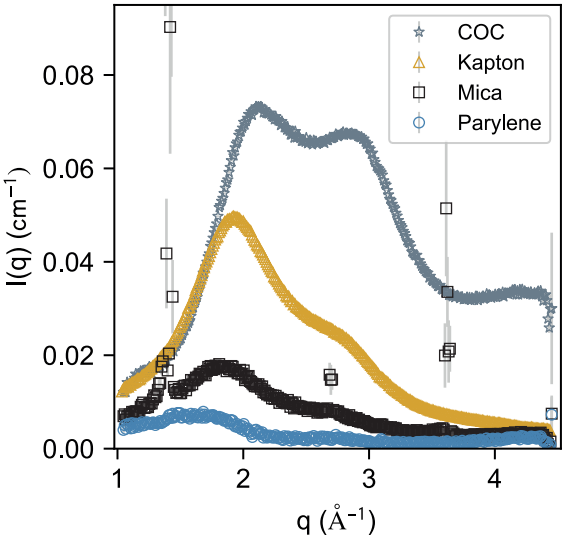

Figure 3.6.: Background scattering of window materials or foil substrates for WAXS experiments: 50 µm COC (gray stars), 25 µm Kapton (yellow triangles), 25 µm Mica sheets (black squares) and 40 µm Parylene (blue circles). Intensities are on absolute scale.

In addition to sample thickness, the foil material, or in case of solution-based WAXS the sample container window material, must be carefully selected with regard to its scattering contribution. Minimizing the background scattering is key for high quality WAXS data, as any background may potentially distort important data or introduce errors due to inaccurate subtraction or modeling.
Here, the background contributions of four different materials are compared in the relevant q-regime of $1.0\,\text{Å}^{-1} < q < 4.5\,\text{Å}^{-1}$. Figure 3.6 shows the scattering of a water filled sample chamber sealed with either 25 µm thick Kapton windows (DuPont, USA), 50 µm thick cycloolefin copolymer (COC) windows (Ibidi GmbH, Germany), 25 µm thick potassium aluminosilicate sheets (muscovite mica) (Goodfellows Cambridge Ltd., UK), or 40 µm thick custom made Parylene windows [78]. These WAXS measurements were performed at our laboratory X-ray scattering setup using an X-ray beam energy of 17.4 keV.
It is obvious that Kapton (orange triangles) and COC (gray stars), which are extensively used as window materials for SAXS experiments [79], show a strong signal in the q-range of $1.0\text{Å}^{-1} < q < 3.5\text{Å}^{-1}$. Therefore, these materials are not suitable as substrate or windows for WAXS experiments. Scattering from Parylene foil (blue circles) exhibits the lowest background signal followed by mica sheets (black squares). However, mica sheets prove themselves also unsuitable as sub-

strate or window material for WAXS measurements due to the distinct exhibition of Bragg peaks at $q \approx 1.4\text{Å}^{-1}$, 2.7Å^{-1} and 3.6Å^{-1} as a result of their crystalline structure. In the light of these findings, we dropped and dried the NP solution on Parylene foil to achieve a strong scattering signal, low background and with low q-uncertainty.
We recorded WAXS data of AuNRs, Au/AgNRs and Au/Ag NR@DNA at the P21.1 beamline at Petra III (DESY, Hamburg). P21.1 is a dedicated high energy beamline and therefore enables high photon flux confined to a beamsize of $1\,\text{mm}^2$ at sample position, low divergence and high energy resolution at a beam energy of 54 keV, which were exceptional conditions for this experiment. We used a Perkin Elmer flat panel XRD 1621 with 2048 x 2048 pixels with a size of 200 x 200 μm^2 as a detector and calibrated the SDD with lanthanum hexaboride.

Bragg peak analysis

The recorded 2D detector images with powder rings were transformed to 1D data sets, hence intensity as function of 2θ angles, via radial integration using the Igor Pro software tool Nika [80]. To analyze the measured lattice spacing of Au/Ag NR@DNA the resulting diffraction signal, which exhibits multiple Bragg peaks, were fitted to a sum of Gaussian peaks. The lattice spacing d was calculated from the peak positions $2\theta_c$ following the relations $d = 2\pi n/q_c$, where n is the diffraction order, and $q_c = 4\pi/\lambda \sin(2\theta_c/2)$. In some cases, the width of the diffraction peaks can be used to estimate an average NP size via the Scherrer equation, in which the width at half peak height β is connected to the crystallite size τ and an empirical constant κ via

$$\beta = \frac{\kappa\lambda}{\tau\cos(\theta_0)}. \tag{3.9}$$

Here, $\kappa \approx 0.9$ is a good approximation [81].

3.2.2. *FCC crystal structure and mono-crystallinity of bimetallic nanorods*

The WAXS intensities for AuNRs, Au/AgNRs and Au/Ag NR@DNA are shown as intensity $I(2\theta)$ vs. the scattering angle 2θ in Figure 3.7. The WAXS data confirmed a fcc crystal structure with a refined lattice spacing of $d_{AuNR} = 4.0745\,\text{Å}$, $d_{Au/AgNR} = 4.0756\,\text{Å}$, and $d_{Au/AgNR@DNA} = 4.0770\,\text{Å}$. As expected Au and Ag Bragg peaks can not be distinguished due to the similarity of the lattice constants. The data suggest a tendency of an increasing lattice spacing with increasing complexity of the particles, i.e. the addition of an Ag shell and DNA shell, respectively. However, this effect is in the sub-Angström regime. The obtained lattice spacings are in good agreement with the lattice constants $a_{Au} = 4.0704\,\text{Å}$ and $a_{Ag} = 4.07778\,\text{Å}$ [67] and confirm monocrystal Au/Ag NR@DNA particles.
The width of the diffraction peaks can be used for an average size evaluation via the Scherrer Equation 3.9 and is calculated to 8.5 nm, 8.2 nm and 8.6 nm for AuNRs, Au/AgNRs and Au/Ag

NR@DNA, respectively. [82]. Although this method is just a rough estimate, especially for anisotropic particles like nanorods, the obtained values agree well with the SAXS data.

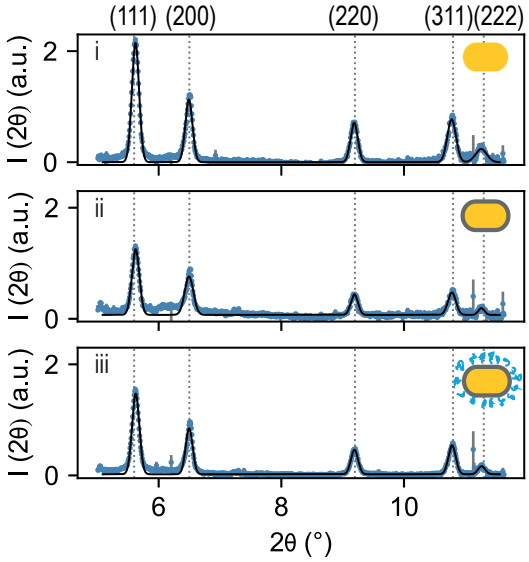

Figure 3.7.: WAXS intensities I(2θ) of AuNRs (i), Au/Ag NRs (ii), and Au/Ag NR@DNA (iii). Vertical dashed lines label selected Bragg peaks present in all WAXS pattern.

In summary, the crystal structure and the monocrystallinity of Au/Ag NR@DNA conjugates was confirmed by WAXS experiments. Furthermore, crystallite sizes that are estimated by the Scherrer equation are in good agreement with the values obtained by SAXS and TEM analysis. Most importantly, we observe no features in the SAXS or WAXS data, which could indicate a permeation of DNA through the Ag shell, thus a porous Ag shell. For example, an additional form factor for well-ordered nanopores would be expected, as they can be regarded as individual inverse scattering particles. Neither is a Gaussian peak in the SAXS or WAXS data observed that would indicate a repeated small intraparticle distance, i.e. a pore size, nor a peak broadening in the WAXS pattern due to increased lattice disorder. Moreover, the modeling of the SAXS data do not yield a vanishing Ag shell, as assumed for a homogeneous material with relatively small randomly distributed pores, but its thickness was found to be in good agreement with the NR design [83]. And lastly, there is no indication of a surface fractal, which can be revealed via power-law like q-dependency in the low and high q-regime [68], as observed for randomly distributed and polydisperse nanopores [83]. Hence, both X-ray scattering experiments, SAXS and WAXS, made an important contribution to derive that the DNA is being conjugated only on the Ag surface through the thiol-Ag bond and does not permeate through the Ag shell.

4. PHOTOSWITCHING OF LIPIDS

The work in this chapter has been partly published in [11], [12], and [13].

Lipid bilayers are the most essential lipid-water assembly in life, as it is the core of all cell membranes. Due to the lipids hydrophobic chains and hydrophilic head, two lipid layers assemble in solution with the heads outside, hydrated in water, and the fatty acid chains inside, tugged away from it (cf. Figure 4.1). Although cell membranes are very complex and contain billions of lipids, proteins, and sugars, and consist of hundreds of different kinds of lipids, simplified cell membrane models, such as unilamellar lipid vesicles, enable a profound investigation of the underlying membrane physics [84]. Photoswitchable lipid membranes are an example of photoresponsive smart materials that can be manipulated by light and thus have a variety of applications including advanced materials [85, 86], photo-controlled self-assembly [87], light-fueled nanomachines [88], cellular process control [89, 90] and photopharmacology [91]. Most photoresponsive materials use an incoming light stimulus as trigger to a macroscopic and eventually functional change by embedding a photoswitchable molecular unit into larger molecules or polymers [92].

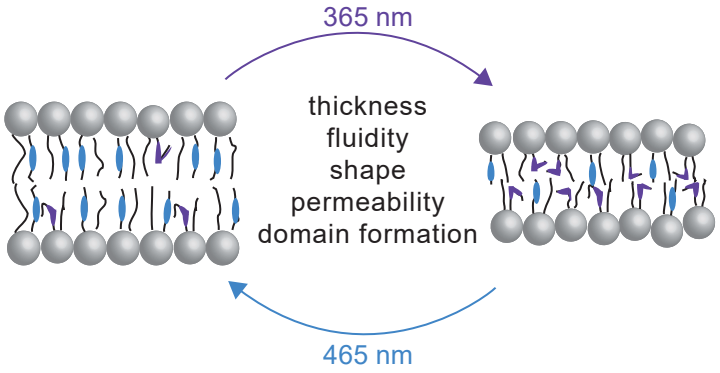

Figure 4.1.: Controlling membrane physics by light. Cartoon illustration of switching azobenzene lipid membranes with UV ($\lambda = 365\,\text{nm}$) and blue light $\lambda = 465\,\text{nm}$, respectively.

Azobenzene, first described in 1834 [93], is a prominent and well-established example of such a molecular photoswitch. The embedding of azobenzene in a membrane forming phospholipid and the precise determination of its optical properties and photo-reactivity [94] paved the way towards the control of many aspects of lipid membrane physics by light, including shape [94], permeability [95], fluidity and thickness [11], domain formation [96], and this way also protein activity modulation [97] (cf. Figure 4.1).

Within this thesis, the manipulation of photo membrane thickness by light was investigated using SAXS experiments. Azo-PC membranes have been proven to offer an enormous degree of structural control, which is not fully accessible by optical means. However, this control can be extended by utilizing a process called catalytic switching induced by radicals. X-rays are here not only used as readout, but also as switching agent. Furthermore, the performance of the photoswitchable membranes was found to dependent on the solvent conditions. Controlling the membrane thickness as well as other biophysical properties are key for potential applications of photoswitchable lipids in synthetic biology or nanomedicine, e.g. as drug encapsulation and delivery systems or for vaccine development [98–100]. Moreover, the demonstration of extended optical control via catalytic switching will hopefully motivate new research for optically dense photoswitchable materials.

Azobenzene

The ability of azobenzene to create light-responsive architectures lies in the structure and properties of its two isomeric forms, which can be switched upon light illumination even under strong steric constraints [101]. The chemical structure of azobenzene is composed of two benzene rings linked by a N=N double bond (cf. Figure 4.2). It exists in the thermally more stable E isomer, which is almost planar due to a C2h symmetry, and the Z isomer, where the two benzene rings are more closely together.

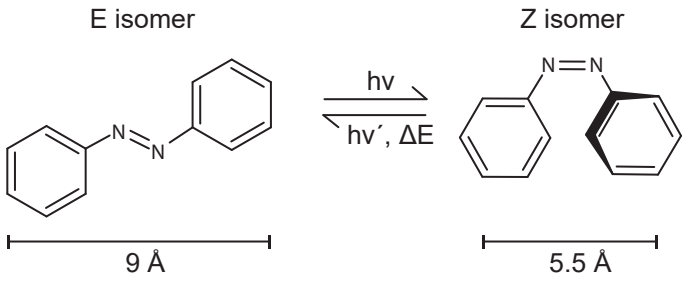

Figure 4.2.: Chemical structure of E and Z isomer of azobenzene and their photo and thermally induced isomerization.

The Z isomer exhibits a non-planar geometry with a dihedral angle of $\sim 45^\circ$ along the CNNC bond due to a C2 symmetry. The structural transformation upon isomerization occurs by two basic pathways: the in-plane increase of the NNC angle to 180°, i.e. the so-called inversion pathway, or the torsion of the molecule around the central CNNC bond, i.e. the so-called rotation pathway [102]. E/Z isomerization (E $\rightarrow$ Z) and Z/E isomerization (Z $\rightarrow$ E) results in a large geometrical change with a size variation of 9 Å vs. 5.5 Å (cf. Figure 4.2). Also, the isomers differ in polarity, i.e. the E isomer is non-polar with a dipole moment $\mu \sim 0\,\mathrm{D}$ whereas the Z isomer is polar ($\mu \sim 3\,\mathrm{D}$). At equilibrium in the dark azobenzene occurs almost exclusively in its more stable planar geometry, hence as E isomer [102–104].

The isomers of azobenzene posses two distinct absorption spectra in solution as demonstrated in Figure 4.3. The E isomer shows a strong UV band peaked at $\sim 320\,\text{nm}$ which arises from a $\pi\pi^*$ electron transition in molecular orbital theory (cf. Figure 4.3 inset). A second weak band can be observed in the visible around $\sim 450\,\text{nm}$. The weak absorption band is assigned to the $n\pi^*$ transition (cf. Figure 4.3 inset).

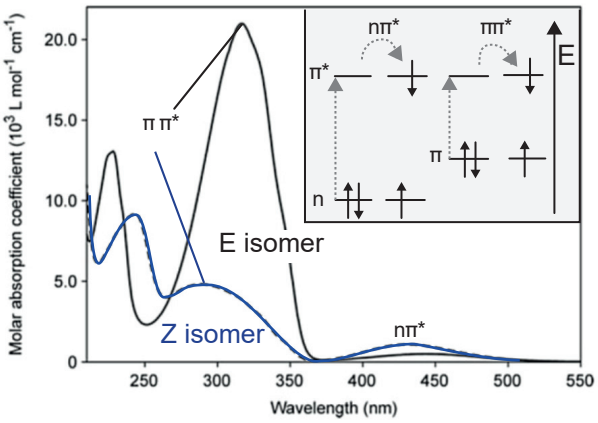

Figure 4.3.: Absorption spectra of azobenzene in acetonitrile. The spectrum of the azobenzene Z isomer is obtained after extended UV illumination. The UV band assigned to an electronic $\pi\pi^*$ and the visible band assigned to an $n\pi^*$ transition are highlighted. Simplified energy levels of azobenzenes' $n\pi^*$ and $\pi\pi^*$ electron excitation are depicted in the inset. Absorption spectra are taken from [103].

This transition is symmetry forbidden for the E isomer and thus exhibits a low absorption coefficient. The $n\pi^*$ transition corresponds to the excitation of an electron from a lone electron pair (n state) of a nitrogen atom into the anti-binding π^* orbital. For the $\pi\pi^*$ transition, an electron from the bonding π orbital is lifted into the anti-binding π^* orbital. Thereby, both transitions revoke the binding properties of the azobenzenes' CNNC bond and enable a free torsion of the benzene rings.

The spectrum of the Z isomer exhibits also two characteristic bands. Here, the UV band peak is shifted towards smaller wavelengths ($\sim 280\,\text{nm}$) and the visible band is more intense. The overlap of both absorption spectra demonstrates the non-orthogonality of the isomerization states, which means that irradiation of either isomer produces a PSS containing a mixture of both. The composition of the achieved PSS depends, among others, on the illumination wavelength and the irradiance. Thus, it is impossible to achieve pure isomerization states by light illumination. For example, UV illumination of azobenzenes induces a PSS, which contains maximal $\sim 95\,\%$ Z isomers under optimal switching conditions [105]. For a blue light induced PSS the reported fractions of E isomer range between 80-97 % [106, 107].

The involved electronic states and reaction pathways of the isomerization process are still an ongoing debate [108–111]. However, isomerization of azobenzene always leads to the excitation of a stable isomer in groundstate (S_0) to an excited higher state surface (S_1 or S_2) via an optical

impulse $h\nu$. It thus follows a $n\pi^*$ or $\pi\pi^*$ electron excitation (cf. Figure 4.4 gray and blue dotted lines). This way, a twisted meta-stable isomer is formed. A simple decay of the resulting meta-stable molecule involves a relaxation from the minimum of the S_1 surface to the maximum of the S_0 surface via a conical intersection. From there, the decay continuous into a minimum of the S_0 surface, i.e. a stable isomer, along with a reorientation of the benzene rings such that either an E or a Z isomer is reformed (cf. Figure 4.4) [106, 112]. However, the isomerization yields of E/Z conversion after excitation to the S_1 or S_2 state differ, which is a violation of the Kasha-Vavilov rule [109, 113]. Moreover, these isomerization yields have found to be further influenced by the isomerization mode (thermal vs.optical), the wavelength, solvent properties and steric hindrance [101, 103, 114]. Despite the complexity of the isomerization process it occurs extremely fast on a timescale of hundreds of femtoseconds to picoseconds [108, 109, 114].

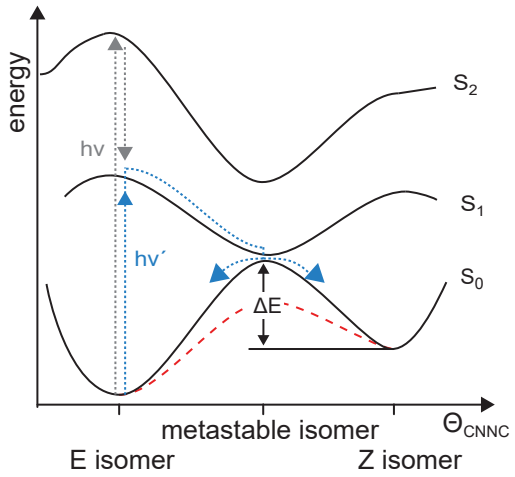

Figure 4.4.: A simplified cartoon illustrates the E azobenzenes' potential energy surfaces in dependence of the torsion coordinate θ_{CNNC}. Possible photoisomerization processes following a $n\pi^*$ ($S_0 \rightarrow S_1$) or $\pi\pi^*$ transition ($S_0 \rightarrow S_2$) are highlighted as blue and gray dotted lines. The energy barrier between Z and E isomer ΔE is decreased for catalytic Z/E isomerization (red dashed line).

Both isomers access the same exited-state surface upon light excitation, but the Z/E isomerization proceeds via different pathways. Besides light-driven Z/E isomerization the Z isomer can thermally relax to the E isomer by overcoming the energy barrier ΔE (cf. Figure 4.4, black line) or, as most recently reported, via a radical driven process called catalytic switching (cf. Figure 4.4, red dashed line).

Catalytic switching is a Z/E isomerization process with the ability to rapidly induce quantitative backswitching, i.e. the establishment of a dark-adapted pure E isomer state via suited electrochemical redox chemistry conditions [115–118]. Here, essentially the Z isomers are extremely fast converted into E isomers due to a decreased thermal barrier ΔE (cf. Figure 4.4, red dashed line). Goulet-Hansen and coworkers propose that catalytic switching works via a chain reaction.

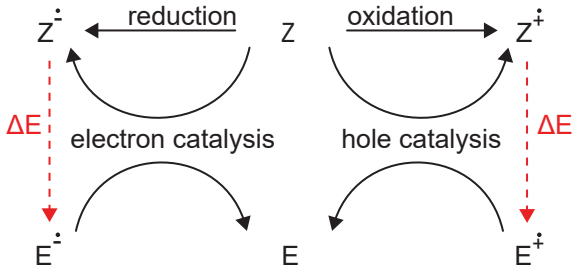

Figure 4.5.: Illustration of both catalytic Z/E switching pathways, the reductive pathway (left) and the oxidative pathway (right). Reduction/Oxidation initiate the formation of a radical anion $Z^{\dot{-}}$ / radical cation $Z^{\dot{+}}$, which rapidly isomerize to $E^{\dot{-}}$ or $E^{\dot{+}}$ (red dashed arrow), respectively. This is followed by an electron/hole transferred equilibrium to achieve E isomers and regenerate $Z^{\dot{-}}/Z^{\dot{+}}$ to continue to chain reaction.

Here, the Z isomer is reduced, i.e. an electron is transferred, and the created Z radical anion immediately converts to an E radical anion. This subsequently reacts with another neutral Z isomer, thereby carrying on the chain reaction (cf. Figure 4.5). The radical $Z^{\dot{}}/E^{\dot{}}$ isomerization is accelerated by 13 orders of magnitude compared with that light driven Z/E isomerization [116]. The analogous chain reaction via oxidation, i.e. the formation of Z and E isomer radical cations via hole catalysis, leads to the same outcome [117].

Azobenzene lipid

The photolipid azo-PC is a synthetic phosphatidylcholine derivative, which harbors an azobenzene in one of the lipid's tails (see Figure 4.6 a).

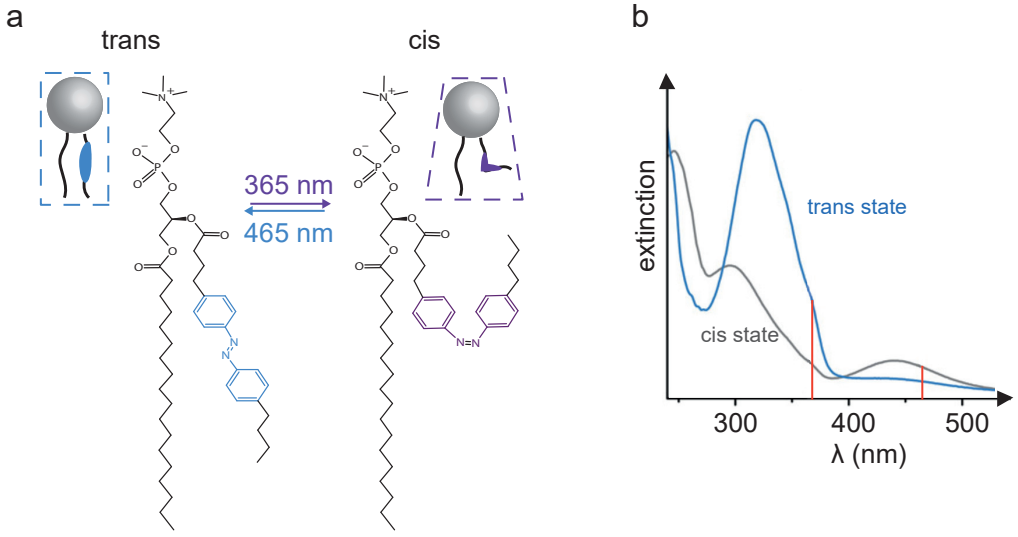

Figure 4.6.: a. Chemical structure of azo-PC. Isomerization between *trans* (E isomer) and *cis* state (Z isomer) is achieved upon UV ($\lambda = 365\,\text{nm}$) and blue light illumination ($\lambda = 465\,\text{nm}$), respectively. b. Absorption spectra of azo-PC in chloroform after extended UV (blue) and blue light illumination (gray). Absorption spectra of azo-PC are taken from [94].

The molecular azobenzene isomerization induces a configurational change within the photolipid as illustrated in Figure 4.6 a. The two configuration states of the photolipid are called *trans* (E isomer) and *cis* state (Z isomer) leaning on the terms of *trans* and *cis* carbon double bonds of unsaturated lipid chains.
As evident from the absorption spectra of azo-PC in chloroform (Figure 4.6 b), the photolipid can be efficiently and reversibly switched between *trans* and *cis* state by UV (λ = 365 nm) and blue light illumination (λ = 465 nm). Due to the insertion of azobenzene in larger molecules the absorption spectra of azo-PC differ slightly from that of azobenzene [103]. Despite the incorporation of the large azobenzene group in one of the lipid tails, can azo-PC assemble into pure azo-PC photolipid bilayers at the presence of water and, importantly, maintain their switching capabilities [94].

Red-shifted azobenzene lipid

If one aims at a wider use of photolipids for biomedical applications, the major stumbling block of azo-PC is its limit spectral range, hence, the requirement of UV and blue light to operate the azobenzene. Both, UV and blue light are problematic when it comes to applications in living cells as it has been proven to be phototoxic and poorly penetrates biological tissue [119, 120].

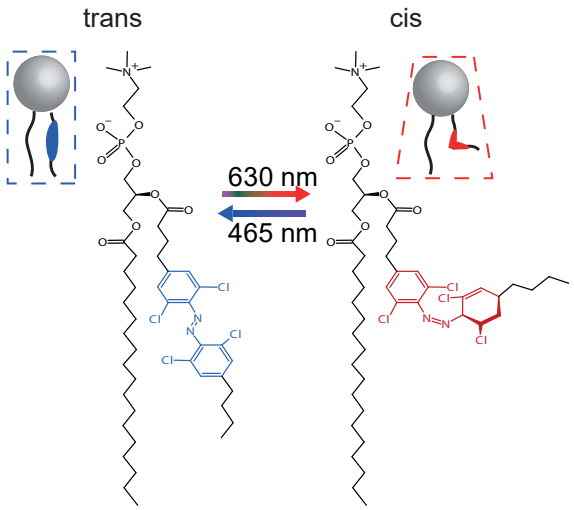

Figure 4.7.: a. Chemical structure of red-azo-PC. Photoswitching can be controlled with different wavelengths in the UV-Vis region. Irradiation with red light (λ = 630 nm) induces efficient *trans*-to-*cis* isomerization and blue light (λ = 465 nm) is suitable to reverse the process.

An important step towards in-vivo applications of photolipids have been achieved by the synthesis of 'red-azo-PC' by the Lohmüller and Trauner group [12]. Red-azo-PC is a phosphatidylcholine based photolipid that harbors a tetra-ortho-chlorinated azobenzene group in its sn2 acyl chain and undergoes photoisomerization on irradiation with tissue penetrating red light ($\geq$ 630 nm) (cf.

Figure 4.7). Like azo-PC, red-azo-PC assembles into lipid bilayers.

4.1. Preparation and structure analysis of unilamellar photolipid vesicles

Preparation of unilamellar lipid vesicles by extrusion is a well-established, fast and reliable technique. Small unilamellar vesicless (SUVs) and large unilamellar vesicless (LUVs) are distinguished according to their diameter, as SUVs are $\leq 50\,\text{nm}$ and LUVs range from 100-200 nm or larger [121]. The standard extrusion protocol was slightly modified, to achieve particular high concentrated lipid vesicle solutions (c=30 $\frac{mg}{ml}$) for SAXS experiments. Azo-PC was initially synthesized by a known method [96] and later purchased from Avanti Polar Lipids, Inc. (Alabama, USA).

4.1.1. *Preconditioning and mixing of azobenzene lipids*

Azo-PC was dissolved in chloroform to a concentration of 25 $\frac{mg}{ml}$ and stored at $-20\,°C$ until further usage. The all-*trans* stock is accessible by storing a solution of azo-PC in the dark for several days. A mostly-*cis* stock (83 %) was generated by saturating UV illumination of azo-PC dissolved in chloroform.

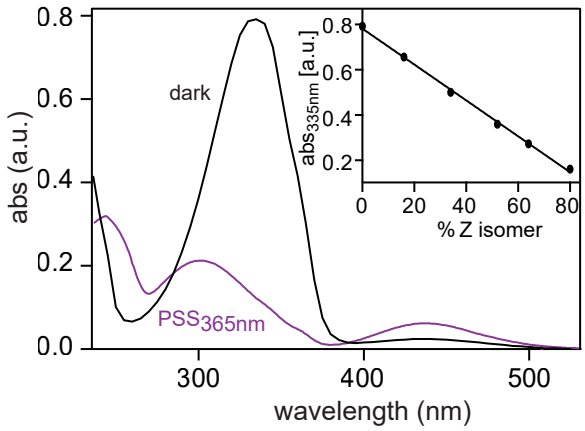

Figure 4.8.: UV-Vis measurements of azo-PC (chloroform stock solution) in the dark-adapted state and in PSS after 365 nm illumination (diluted into methanol for UV-Vis measurement). Calibration curve of absorbance at 325 nm as a function of %Z is given in the inset. The calibration measurement was performed by A. Müller-Deku.

The %Z, i.e. the Z isomer fraction, in the mostly-*cis* stock was determined by UV-Vis measurements of azo-PC in methanol and compared to a calibration series of spectra established for different *trans*/*cis* ratios of a simple, non-charged, non-polar model compound called FAzoM. FAzoM was synthesized by the Thorn-Seshold group and contains the identical chromophore as azo-PC. It consequently exhibits a well matching UV-Vis spectrum and can unlike azo-PC be analyzed quantitatively for its *trans*/*cis* ratio by high-performance liquid chromatography (HPLC). This

workaround was established in collaboration with A. Müller-Deku. The azo-PC *cis*-fraction of the mostly-*cis* stock was calculated via linear correlation of the absorbance at 335 nm (maximum absorbance of the E isomer) to the Z isomer fraction as measured by HPLC. The UV-Vis spectra of the dark-adapted and the mostly-*cis* azo-PC stock are shown in Figure 4.8. The inset gives the calibration curve of the absorbance at 335 nm as function of %Z which was obtained for FAzoM via HPLC. The dark-adapted stock was also measured spectroscopically and had $\%Z < 0.5\%$. Finally, the all-*trans* and the mostly-*cis* stocks of azo-PC were mixed in a range of proportions, before SUVs were prepared in the dark.

4.1.2. *Preparation of unilamellar photolipid vesicles*

Preparation of photolipid vesicles starts with the evaporation of the chloroform under a nitrogen stream and storage under vacuum for a few hours to dispose solvent residues. The resulting dry lipid film was either directly hydrated with DI water (Mili-Q, Rephile Bioscience Ltd., Boston, USA, phosphate buffered saline (PBS buffer, pH 0 7.5) or 1 x TE buffer (10 mM Tris, 1 mM EDTA, pH = 8) to a final concentration of 30 $\frac{mg}{ml}$ or after an intermediate lyophilisation step. For this purpose, the dried lipid film was dissolved in cyclohexane (Sigma-Aldrich, USA), exposed to vacuum of 6×10^{-3} mbar at a temperature of $-60\,^{\circ}$C yielding a fluffy lipid powder, and subsequently hydrated to 30 $\frac{mg}{ml}$. The increase of surface area via lyophilisation was only necessary for some azo-PC batches as the hydration of a dried azo-PC film can lead to phase separation [122]. The achieved lipid-water suspension was gently vortexed to achieve a homogeneous phase, which was then subjected to at least five freeze/thaw cycles. Finally, the sample solution was extruded through a polycarbonate membrane with a pore size of 50-100 nm in diameter for approximately 25 times using a Mini Extruder (Avanti Polar Lipids, Inc., Alabama, USA). The rather small pore size facilitated the formation of unilamellar vesicles [123].

4.1.3. *Illumination of azobenzene lipid vesicles*

For switching of the azo-PC membranes, a UV and blue light LED setup, which is shown schematically and as photograph in Figure 4.9, was built by A. Baptist and C. Sattler under the scope of a bachelor thesis and a laboratory practical course [122, 124]. For UV illumination, we focus a high power LED (Roschwege Star-UV365-03-00-00, $\lambda = 365$ nm, FWHM = 9 nm, Conrad Electronic SE, Germany) through two lenses that form an infinite optical system on the sample capillary (Quartz glass, Hilgenberg GmbH, Germany). This way, the total maximum power output of 170 mW and a focal spot size of $\sim 4\,\mathrm{mm}^2$ yields an irradiance of 4 $\frac{W}{cm^2}$. For blue light illumination, which is fed in by a dichroic mirror, a second high power LED (Roschwege LSC-B, $\lambda = 465$ nm, FWHM = 18 nm, Conrad Electronic SE, Germany) was used. The blue light is focused on the sample capillary with the same focal spot size and and a total maximum optical power of 120 mW, resulting in an irradiance of $\sim 3\,\frac{\mathrm{W}}{\mathrm{cm}^2}$. The LEDs and the X-ray detector were remotely controlled

by TTL signals from an Arduino microprocessor (Reichelt electronics GmbH & Co. KG, Germany).

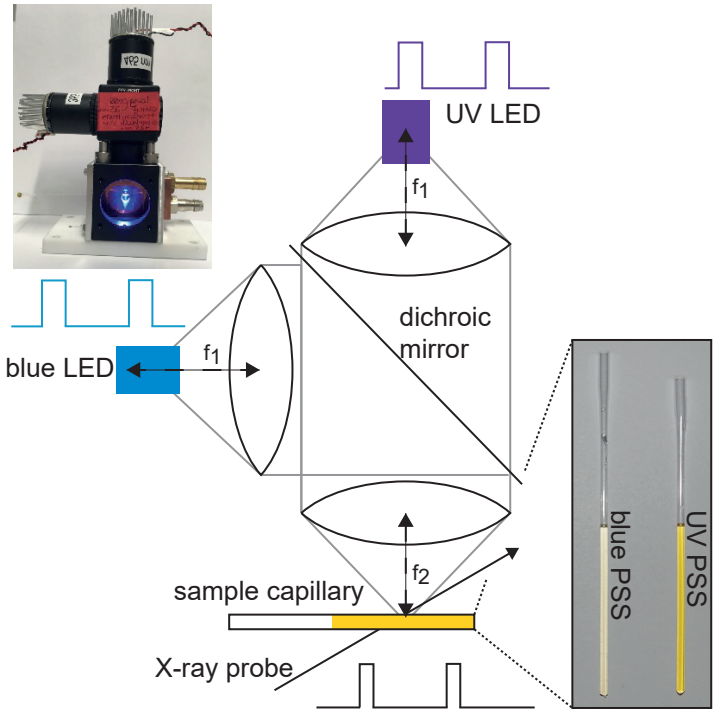

Figure 4.9.: Schematic drawing of our self-built dual LED pump X-ray probe setup for SAXS measurements while illumination. A photograph of the setup as well as two capillaries with azo-PC SUVs in the PSS at 465 nm (predominantly *trans*, left) and at 365 nm (predominantly *cis*, left) are shown.

4.1.4. *Illumination of red-shifted azobenzene lipid vesicles*

For *trans*/*cis* switching of red-azo-PC membranes, a helium-neon laser (λ = 630 nm, Thorlabs Inc., United States) with an irradiance of $0.33\,\frac{\mathrm{W}}{\mathrm{cm}^2}$ was used and a focal spot size of $1\,\mathrm{mm}^2$ was pointed on $\approx$ 0.5ml of photolipid solution in a glass vessel. The lipid solutions was exposed to the laser light for approximately 120min. For blue light illumination, i.e. *cis*/*trans* switching, we used a high power LED (λ = 405 nm, Thorlabs Inc., United States) with a maximum total output power of approximately 170 mW in a focal spot size of $4\,\mathrm{mm}^2$ resulting in an irradiance of $4\,\frac{\mathrm{W}}{\mathrm{cm}^2}$. Here, illumination time was ca. 10min. To avoid water evaporation during the illumination, the sample was continuously cooled with iced water.

4.1.5. *Experimental considerations and details*

Structure analysis of lipid vesicles by SAXS has been performed for decades and is well-covered in literature [125–128]. SAXS intensity distributions of lipid bilayers exhibit typically a strong

signal in the q-range of $0.05\,\text{Å}^{-1} < q < 0.5\,\text{Å}^{-1}$ and consist of a few distinct oscillations with sharp intensity dips. Although some detailed information like bilayer asymmetry between inner and outer leaflet [127, 129] or bilayer curvature [128] require SAXS data in the low q-region, one intensity oscillations in a medium q-region are sufficient to obtain the dimensions of a lipid bilayer in a very robust manner.
As the experimental details of the SAXS experiments performed on photoswitchable lipid membranes differ substantially regarding to the specific experiment and research question they are separately presented below.

Dual LED pump X-ray probe and catalytic switching by soft X-rays

To explore the structure changes of photolipid membranes upon in-situ UV/blue light illumination at biologically relevant temperatures, we built a complex UV/blue light pump X-ray probe setup, where the sample temperature could be controlled. Intense and homogeneous UV/blue light illumination of highly concentrated and optically dense photolipid vesicles is challenging and calls for high LED irradiance. High power LEDs and lenses arranged for infinite optics solved this problem so that an irradiance of $4.25\frac{\text{W}}{\text{cm}^2}$ for a focal spot size of 2 x 2 mm^2 was achieved (cf. chapter 4.1.3). This way, the light illumination setup determined the optimal SAXS sample thickness to be maximal 2mm to guarantee the X-ray readout within the illuminated sample volume. A sample thickness of 1.5-2mm provides a maximum relative scattering intensity at a beam energy of $8-10\,keV$ as detailed in section 2.2.1. Working with smaller sample volumes was furthermore motivated by the limited availability of large photolipid amounts due to its elaborate synthesis.
An 8 keV X-ray beam with a size of 0.5 x 2 mm^2 at sample position, as delivered by the SAXS beamline at Elettra [43], provided ideal conditions to investigate photolipid membranes during in-situ illumination. High photon flux (10^{13} cts/s/mm^2), an accessible q-range of $0.07\,\text{Å}^{-1} < q < 0.5\,\text{Å}^{-1}$, and a q-uncertainty of $\Delta q = 1\times10^{-3}\,\text{Å}^{-1}$, provided a well-defined membrane signal [43]. The signal-to-noise ratio suffered slightly from short X-ray exposure times. However, these were necessary to limit the deposited X-ray dose and, thus, the influence of X-rays on the photo physics of the lipids (cf. section 2.2.4). Detailed timing parameters are, if not specifically given, summarized in Table A.1 in the appendix.
The same experimental design was used to study catalytic switching, i.e. switching of the photolipids via redox pathways. Here, the high photon absorption cross-section for soft X-rays were exploited and X-ray exposure times extended. This way, a certain dose could be deposited. By the radiolysis of water soft X-rays give rise to more and more oxidative and reductive species, which provide pathways for catalytic switching.
For both experiments, the photolipid solution was loaded in 1.5-2 mm diameter Quartz glass capillaries (Hilgenberg GmbH, Germany) by flow-through and placed in the UV/blue light pump X-ray probe setup. A Pilatus 3 1 CMOS detector from Dectris Ltd., Switzerland, with 981 x 1043 pixels of 172 x 172 µm^2 and 300 µm sensor thickness, was used for efficient X-ray detection (QE ≈

97 %). The beampath was guided through evacuated tubes, as air scattering is a major contribution to the background for soft X-rays.
To compare our results for azo-PC vesicles in DI water to the structural changes induced upon UV/blue light illumination and catalytic switching for azo-PC vesicles in buffered solutions, we conducted the measurements of azo-PC in PBS and 1xTE with similar experimental conditions at the SAXS beamline at Elettra using 8 keV beam energy [43]. A smaller beamsize of 0.2 x 2 mm^2 was used and sample solutions were loaded into 1.5 mm thick standard Quartz glass capillaries (Hilgenberg GmbH, Germany) instead of using our self-built LED pump X-ray probe setup. Furthermore, the photomembranes were switched ex-situ prior to the SAXS measurement.

High energy SAXS as low dose X-ray probe

To counter check the catalytic switching mechanism, SAXS experiments without water radical production upon X-ray exposure were required. As detailed in section 2.2.4 the use of higher X-ray energies for SAXS experiments ensures a drastically reduced X-ray dose and provides high quality SAXS data. Hence, we took advantage of the unique possibility to perform SAXS experiments on photolipid vesicles at P21.1 at PETRA III [46]. Here, we used high energy X-rays with 54 keV and a beamsize of 1 x 1 mm^2 at sample position. A helium filled flight tube was utilized to reduce air scattering. For this experiment, the sample solution was first switched optically and then loaded into Kapton tubes (Rotima AG, Switzerland) of 40 mm length and 2.5 mm in diameter. The extended sample thickness contributed to a high signal-to-noise ratio, but required a large amount of sample and impaired the q-uncertainty.
The SAXS setup was designed with a rather long SDD of ~ 4.2, which made a q-range of $0.09\,\text{Å}^{-1} < q < 0.3\,\text{Å}^{-1}$ accessible. However, as discussed in section 2.2.2, the scattering signal decreases with increasing SDD. Here, the loss in scattering signal was balanced by P21.1's high photon flux (10^{10} cts/s/mm^2), the usage of a 500 µm thick GaAs sensor as detector (Lambda 350k detector, X-Spectrum GmbH, Germany) and the possibility to extend the X-ray measurement times without the risk of radiation damage.
The availability of the GaAs based Lambda 350k detector was crucial to obtain high data quality for SAXS experiments using an X-ray beam energy of 54 keV. This derives from still ~ 50 % detection efficiency for 54 keV X-rays and its composition of 772 x 516 pixels with a rather small 55 x 55 µm^2 pixel size that reduce the q-uncertainty (cf. section 2.2.1 and 2.2.3).

SAXS on photolipid vesicles at a Molybdenum-sourced laboratory setup

SAXS measurements on photolipid vesicles with premixed *trans*/*cis* ratios, which are prepared from preconditioned monomer solutions, were performed at a Mo-sourced laboratory setup. Here, the photolipids were illuminated ex-situ prior to the scattering experiment and it was crucial to maintain the preconditioned PSS during the SAXS measurement. Consequently, a low dose X-ray

beam was of great importance, which can be achieved either via high energy X-rays or via low flux, e.g. with laboratory SAXS experiments.
Here, some hands-on aspects of the photolipid vesicle preparation, e.g. their immediate preparation in the dark the measurement, was decisive to perform these experiments at our Mo-source laboratory setup. It delivers an X-ray beam energy of 17.4 keV and a beam size of 1 x 1 mm^2 with a flux of 2×10^6 cts/s/mm^2 at sample position. A SDD of 1m and X-ray exposure times of several hours enabled high quality SAXS data with a q-uncertainty of $\approx \Delta q = 4 \times 10^{-3}$ $Å^{-1}$. A Pilatus 3 R 300K CMOS detector with 487 x 619 pixels of size 172 x 172 μm^2 equipped with a 1000 µm thick silicon sensor, ensured high detection efficiency (cf. chapter 2.2.5). A 10 mm thick aluminum chamber sealed with Kapton foil windows (DuMont, USA) served as sample container. The SAXS experiments on red-azo-PC vesicles were also performed at a Mo-sourced laboratory setup, due to limited availability of synchrotron beamtime.

4.1.6. *Flat symmetrical lipid bilayer model*

All bilayer parameters are obtained from model fits of the total scattering intensity $I(q)$ to a flat symmetrical bilayer model in dependence of the scattering vector q, given by $q = |\overrightarrow{q}| = \frac{4\pi}{\lambda} \sin(2\theta(/2))$. Here, λ is the X-ray wavelength and 2θ the scattering angle [127, 128].

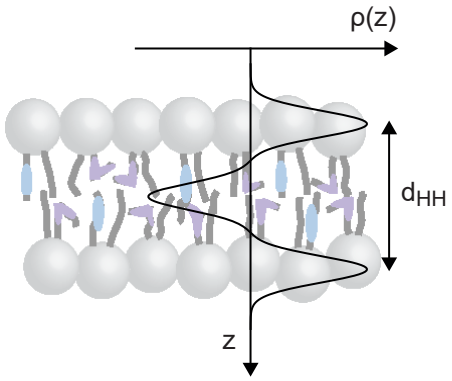

Figure 4.10.: Illustration of a flat symmetrical bilayer model. For SAXS data analysis the electron density is modeled as a sum of three Gaussians, representing the two head groups and the chain region, respectively. The bilayer thickness d_{HH} is given by the distance between the two headgroup's maxima.

The electron density profile $\Delta\rho(z)$, which enters into the form factor $F(q)$ by $F(q) = |f(q)|^2 = |\int \rho(z) \exp(iqz)\, dz|^2$ is composed of three Gaussians representing the

$$\rho(z) = \Delta\rho_H \cdot e^{\left(-\frac{(z-z_H)^2}{2\sigma_H^2}\right)} + \Delta\rho_{CH} \cdot e^{\left(-\frac{z^2}{2\sigma_{CH}^2}\right)} + \Delta\rho_H \cdot e^{\left(-\frac{(z+z_H)^2}{2\sigma_H^2}\right)} \tag{4.1}$$

two electron rich headgroup regions and the electron poor chain region (see Figure 4.10). $\Delta\rho_H$ is the scattering length contrast of the lipid headgroups compared to water, i.e. $\Delta rho_H = \rho_H - \rho_w$.

z_H is the spatial peak offset of the head centers in respect to the center of the bilayer, and σ_H is the corresponding variance of the Gaussian functions. $\Delta\rho_{CH}$ is the scattering length contrast of the lipid chains and σ_{CH} the variance of the Gaussian function describing the chain region.
The bilayer thickness d_{HH} is given by the distance between the two headgroup's maxima (HH = head-to-head) within the bilayer. The flat symmetrical bilayer model assumes that vesicles are a perfect powder of flat membrane patches with a symmetrical profile. Hence, the spherical shape of the vesicles is not taken into account, which reduces the number of free parameters and is a valid assumption for the vesicle diameter $R >> d_{HH}$. While the amplitude and width of the head group regions were fixed to $\Delta\rho_H = 1$ (a.u.), $\sigma_H = 3$ Å, the amplitude and width of the Gaussian representing the chain region as well as the two outer Gaussian positions $\pm z_H$ are free parameters. The final expression of the SAXS intensity is given by

$$I(q) \propto \frac{1}{q^2} F(q). \tag{4.2}$$

The head-to-head distance uncertainty composes of purely statistical parameter errors corresponding to the 95 % (two-σ) confidence interval and uncertainties reflecting the robustness of d_{HH} with respect to the fitting model, which is approximately $\pm(0.5 - 1.0)$ Å depending on the signal-to-noise level of the data.

4.2. Optical control of azobenzene lipid membranes

In order to quantify the effect of photoswitching on azo-PC membrane thickness for certain PSSs during UV and blue light illumination, SAXS measurements were performed. Therefore, we prepared SUVs in DI water consisting purely out of azo-PCs following a protocol described in section 4.1.2. For an X-ray readout while LED illumination at a controlled temperature, a custom-built LED pump X-ray probe setup up was used (see section 4.1.3).

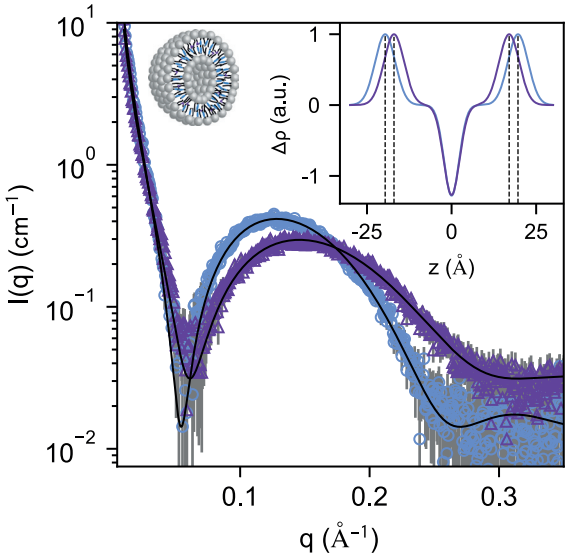

Figure 4.11.: SAXS intensity distributions I(q) of azo-PC vesicles after 50s of blue light exposure (blue circles) and 50s of UV light exposure (violet triangles) at 25 °C with the best fit of a flat, symmetric bilayer model (solid lines). Intensity is on absolute scale. The inset gives the corresponding electron density profiles $\rho(z)$ as a function of distance z from the bilayer center. Bilayer thicknesses are highlighted with dashed lines.

The SAXS intensity distributions for azo-PC SUVs upon saturating UV (purple triangles) and blue light illumination (blue circles) at 25 °C are shown in Figure 4.11. Both SAXS signals $I(q)$ exhibit a sharp dip at low q values followed by a distinct intensity oscillation characteristic for lipid bilayers. Hence, the photolipid bilayers stay intact upon photoisomerization. The head-to-head distance d_{HH} between the photolipids in the two bilayer leaflets can be obtained from the modeling of the electron density profiles as shown in the inset of Figure 4.11. The full electron density model is detailed in 4.1.6. For the *trans*-rich azo-PC membrane induced by extensive blue light illumination a head-to-head distance of $d_{HH}^{trans} = 39.3 \pm 1.0$ Å was found. For extended UV illumination, we forced the azo-PC membrane predominately into *cis* states and yielded $d_{HH}^{cis} = 34.0 \pm 1.3$ Å. Thus, the bilayer thickness is reduced by $\Delta d_{HH} = d_{HH}^{trans} - d_{HH}^{cis} = 5.3 \pm 1.6$ Å as a consequence of azobenzene isomerization in the lipid tails.

So far, we have used SAXS to determine the membrane thickness for blue or UV light photosta-

tionary states reached in azo-PC SUVs in DI water. Here, the SAXS measured membrane thicknesses of the dark-adapted all-*trans* azo-PC membrane was compared to membrane thicknesses yielded by UV and blue light illumination. This way, we checked if the blue light PSS thickness is close to the theoretical maxima of a pure all-*trans* state. The SAXS measured membrane thicknesses of four additional switching experiments on azo-PC SUVs in DI water at room temperature are condensed in Figure 4.12 and the full data set are shown in Figure A.1. For each experiment the SAXS signal of the dark-adapted state was recorded prior to illumination. Subsequently, the azo-PC SUVs were exposed to UV illumination and in two cases also to blue light illumination (cf. Figure 4.12, squares). The UV illumination times are indicated in Figure 4.12. The timing details are given in Table A.1.

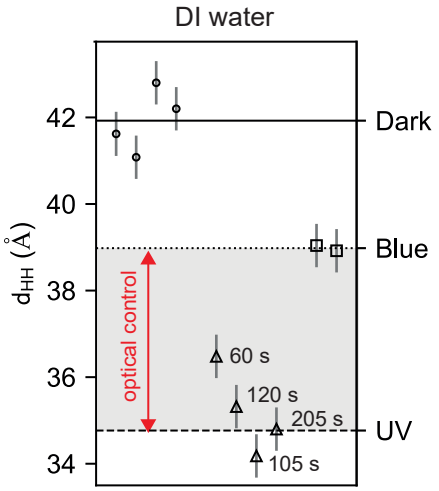

Figure 4.12.: Head-to-head distances d_{HH}, i.e. membrane thickness, obtained for azo-PC SUVs in DI water under varying PSSs. The dark-adapted state, and several PSSs induced via UV and blue light are labeled accordingly. Horizontal lines indicate mean values of d_{HH} for the dark-adapted, UV, and blue light PSSs, shown as solid, dashed, and dotted line, respectively. The exposure time of UV light while approaching the PSS is indicated in seconds. The optical control window is indicated by a red double-headed arrow.

The dark-adapted states (all-*trans*) yielded a mean membrane thickness of $d_{HH}^{dark} = 41.9 \pm 0.9$ Å (cf. Figure 4.12, circles; mean value, solid line). To photoswitch towards high *cis* contents UV illumination was used. Here, a rather large spread of d_{HH}^{UV} (cf. Figure 4.12, triangles; mean value, dashed line) is consistent with the dependence of the PSSs on the duration of light illumination. However, when using blue light to photoswitch from a *cis*- to a *trans*-enriched state, the maximal blue light PSS membrane thickness is $d_{HH}^{blue} = 39.0 \pm 0.3$ Å (cf. Figure 4.12, squares; mean value, dotted line). Unexpectedly, it is substantially smaller than the dark-adapted state thickness. Thus, saturating blue light illumination does not photoswitch the membrane back in an all-*trans* state. Optical control of azo-PC vesicles is therefore restricted in DI water and covers only 70 % of the thickness control achievable with optimized backswitching conditions.

4.3. Thermal stability of the photoswitching of azobenzene lipid membranes

Next, we measured the SAXS signal of azo-PC SUVs between 25 °C and 55 °C to probe the thermal stability of both photolipid conformations at biologically relevant temperatures. As shown in Figure 4.13 the mean thickness change of $\Delta d_{HH} = 4.0 \pm 1.0$ Å is constant over the whole temperature range. Hence, the structural control of azo-PC membranes preserves at elevated temperatures and no thermal relaxation of the photolipids is observed.

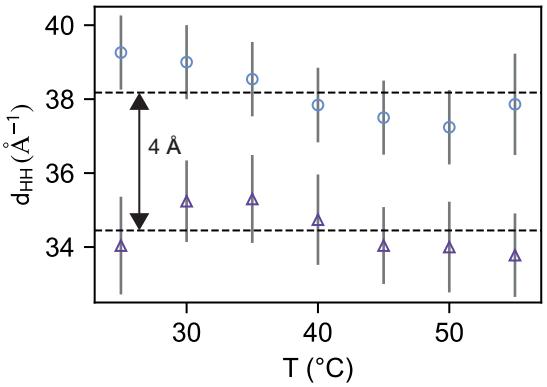

Figure 4.13.: Head-to-head distances d_{HH}, i.e. membrane thickness, of azo-PC membranes as function of temperature derived from SAXS measurements. d_{HH} is evaluated during a temperature ramp from 25 °C to 55 °C. Extended blue light illumination yields a PSS containing predominantly *trans* state azo-PC (blue circles), whereas extended UV exposure yields predominantly *cis* state azo-PC (violet triangles). Dashed black lines correspond to the mean values.

4.4. Optical control of red-shifted azobenzene lipid membranes

The effect of photoswitching on red-azo-PC vesicles was analyzed by performing SAXS experiments at our laboratory setup. For this experiment, a *cis*-rich photomembrane was received by extended ex-situ red light illumination ($\lambda = 630$ nm) and the isomerization reversed via ex-situ LED blue light illumination. The PSSs obtained via external illumination sustained stable over the SAXS experiment due to the low dose X-ray probe of a Mo-soured laboratory SAXS setup (section 2.2.4 and section 4.1.5). Details of vesicle preparation and illumination are explained in section 4.1.2 and 4.1.4, respectively. In Figure 4.14 the SAXS signal $I(q)$ of red-azo-PC vesicles upon red light (red circles) and blue light illumination (blue triangles) are given on absolute scale. Similar to the 'standard' azo-PC membrane, the SAXS intensity of red-azo-PC membranes shows a typical lipid bilayer signal, i.e. a sharp dip at low q-values followed by a distinct oscillation. Despite large chlorine substituents attached to the azobenzene, red-azo-PC forms lipid bilayers, which maintain the photoisomerization capability and stay intact upon illumination. Although, a difference of the SAXS pattern upon photoisomerization can be observed, it is significantly smaller compared to the 'standard' azo-PC.

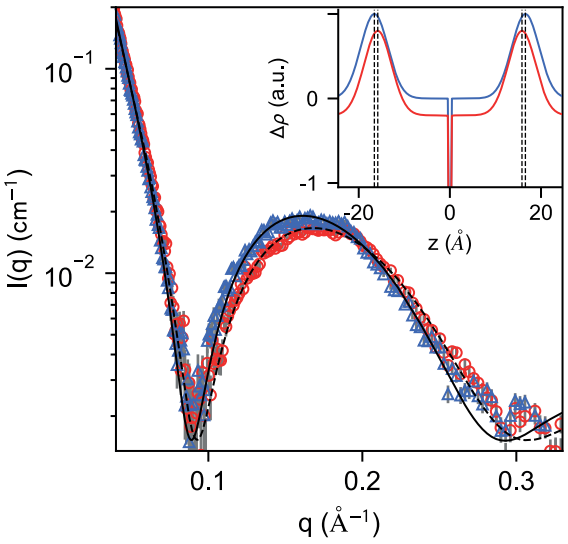

Figure 4.14.: SAXS intensity distributions I(q) of red-azo-PC SUVs after extended red light exposure (red circles) and blue light exposure (blue triangles) at 25 °C with the best fit of a flat, symmetric bilayer model (solid and dashed black lines). Intensity is on absolute scale. The inset gives the corresponding electron density profiles $\rho(z)$ as a function of distance z from the bilayer center. Electron density profiles are vertically offset for clarity. Bilayer thicknesses are highlighted with dashed lines.

By modeling of the electron densities (Figure 4.14 inset) the *trans*-rich PSS membrane thickness $d_{HH}^{trans} = 33 \pm 1$ Å was obtained. The *trans*-red-azo-PC bilayer is therefore ~ 6 Å thinner than a *trans*-azo-PC bilayer, which is indicative for a largely increased lipid disorder. Furthermore, the head-to-head difference for a red-azo-PC bilayer after photoswitching with 630 nm light is only $\Delta d_{HH} = 1.5 \pm 1$ Å.

4.5. Membrane thickness as readout for photoswitching efficiency

Quantitative photoisomerization to all-*cis* or to all-*trans* azobenzene populations is limited by the overlap of the azo-PC's absorption spectra. For example, photostimulated thickness changes of azo-PC membranes upon blue or UV light illumination reaches ca. 4 Å thickness change for ca. 42 Å (10 %) thick membranes (see section 4.2). However, so far it is not known what population levels of *trans*/*cis* ratios where responsible for this changes and whether they could be substantially improved by tailored conditions and switching stimuli. This partly derives from a technical challenge: while it is straightforward to measure *trans*/*cis* ratios in molecular solutions by a variety of methods, measuring the *trans*/*cis* ratios of azo-PC vesicles by proton nuclear magnetic resonance (H-nmR), HPLC or UV-VIS absorption measurements were purely reproducible. Here, SAXS experiments on azo-PC vesicles with a predefined *trans*/*cis* ratio fill this gap, as they revealed a linear increase of the membrane thickness with *trans* fraction.

Azo-PC vesicles of known *trans*/*cis* ratios were prepared from mixing dark-adapted, all-*trans* and

mostly-*cis* (83 %) azo-PC stock solutions, see section 4.5 for details. In total, we prepared six different membrane compositions: 0 % (dark-adapted), 10 %, 19 %, 39 %, 58 %, and 83 % *cis* azo-PCs with an error of ±5 % accounting for mixing precision and *cis* fraction uncertainties in the preconditioned samples. The SAXS intensities for these *trans*/*cis* ratios are shown in Figure 4.15 a. Again, the SAXS pattern are typical for lipid bilayers even for the highest *cis* fraction of 83 %. Thus, not only all-*trans* but also mostly-*cis* membranes form stable lipid bilayers. The SAXS pattern vary strongly with the *trans*-to-*cis* (*trans*/*cis*) ratio, i.e. the intensity dip around $q = 0.05\,\text{Å}^{-1}$ shifts consecutively to higher q-values with increasing *cis* azo-PC content. This shift is indicative for a thinning of the photomembrane with increasing *cis* fraction.

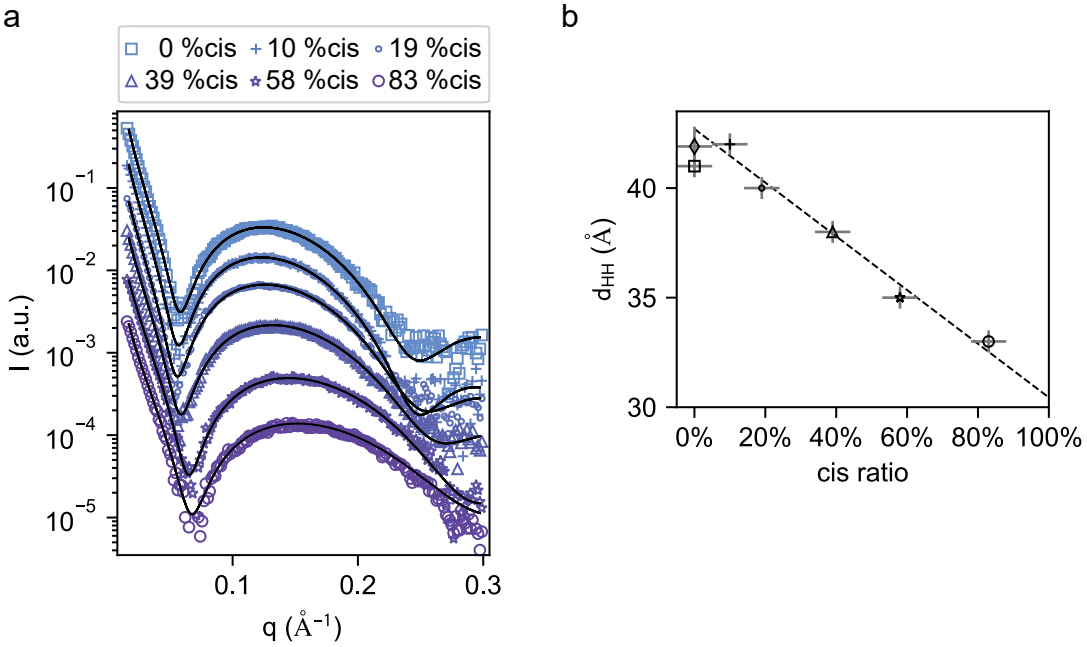

Figure 4.15.: SAXS intensities I(q) for azo-PC SUVs prepared from predefined *trans*/*cis* ratios: Dark-adapted state (100:0), (90:10), (81:19), (61:39), (42:58), and (17:83) are shown as squares, crosses, dots, triangles, stars, and circles. Intensities are offset for clarity. b. Head-to-head distance d_{HH} of azo-PC membranes as function of the percentage of azo-PCs in *cis* isomerization state are shown with the same symbols as in (a). Additionally, the mean value of d_{HH} for the dark-adapted PSSs obtained for azo-PC SUVs in DI water (Figure 4.12) is shown as diamond. The linear fit of d_{HH} in dependence of *cis* isomer ratio is indicated as dashed line.

To extract the head-to-head distance d_{HH} as function of *trans*/*cis* ratio, SAXS intensities are model fitted by a well-established electron density profile (see section 4.1.6). The results of this analysis are summarized in Figure 4.15 b. Increasing percentage of azo-PC in *cis* state results in a thinning of the membrane down to $d_{HH}(83 \pm 5\,\%cis) = 33.0 \pm 0.5$ Å for the highest achievable *cis* fraction. The dark-adapted state exhibits a thickness of $d_{HH}(0 \pm 5\,\%cis) = 40.9 \pm 0.6$ Å. Thus, under ideal switching conditions the membrane thickness changes by minimum 8 Å, which is almost twice as

large as the thickness change observed in optical switching experiments (cf. section 4.2). Furthermore, the SAXS measured membrane thicknesses of predefined *trans*/*cis* ratios reveal a linear correlation of the membrane thickness d_{HH} and the percentage of azo-PCs in *cis* isomerization state (Figure 4.15 b, dashed line) as given by Equation 4.3. By least-square fitting of five membrane compositions 10 %, 19 %, 39 %, 58 %, and 83 % *cis* fraction we find the relation

$$d_{HH} = 42.7 - 0.1226x(\%Z). \tag{4.3}$$

As evident from Figure 4.15 b and Figure 4.12 the measured thickness for the dark-adapted state (0 % *cis*) is widely spread. Therefore, the first data point (0 % *cis*) was treated as outlier and omitted in the linear fit. Applying this calibration curve to the measured relevant head-to-head distances for azo-PC vesicles enables to calculate their respective *trans*/*cis* ratios. This referencing method is novel in this field and the first robust method, which enable the determination of the *trans*/*cis* ratio of photolipid vesicles. In the following measurements, this relation between membrane thickness and *cis* fraction is used to infer the *cis* fraction of various photostationary states.

	d_{HH} (Å)	*%cis*
dark-adapted	41.9 ± 0.9	7 %
PSS_{blue}	39.0 ± 0.3	30 %
PSS_{UV}	34.8 ± 0.6	64 %

Table 4.1.: Head-to-head distances d_{HH} of azo-PC membranes in DI water, obtained from SAXS measurements collected for the dark-adapted state and during UV or blue light illumination (section 4.1.3) and their calculated percentage of *cis* isomerization states.

Table 4.1 gives the *cis* fraction for UV and blue light PSSs of azo-PC membranes in DI water. Here, a *cis* content of only 64 % for the PSS induced by extended UV illumination (PSS_{UV}) is obtained. Hence, a *cis* fraction of 83 % as obtained by preconditioned azo-PC stock solutions could not be reached. For the PSS after extended blue light illumination (PSS_{blue}), as expected from SAXS measurements presented in section 4.2, a rather high *cis* fraction about 30 % is found. Thus, establishing the thickness as readout of the *trans*/*cis* ratio of photomembranes, uncovered the fact that the optical window for azo-PC vesicles in DI water is limited for both isomerization pathways.

4.6. Catalytic switching of azobenzene lipid vesicles by X-rays

Next, methods to improve the limited optical control in DI water were explored. For this purpose, the catalytic backswitching mechanism (cf. Chapter 4) was triggered by the deposition of a certain X-ray dose deposited to the azo-PC vesicle solution. Thus, the chain reaction for catalytic switching is initiated by the production of oxidative and reductive radicals by the radiolysis of water.

The X-ray dosing experiment was conducted as follows. First, azo-PC vesicles with a high *cis* fraction were prepared by prolonged UV illumination. Then, we exposed the sample for 60 s to a high X-ray energy of 54 keV. This experiment served as negative control, as the photo cross-section for photo absorption is dramatically reduced for high X-ray energies. This way, no water radicals should be produced and no catalytic backswitching observed as explained in section 4.1.5. In deed, five of such consecutive X-ray exposures yield an identical SAXS signal (cf. Figure 4.16) and there is no sign of any X-ray induced effects after 5min, even though this experiment was performed at a Petra III synchrotron beamline with full beam on the sample. This finding is in agreement with the fact that the cross-section for photoabsorption is dramatically reduced for high X-ray energies (cf. section 2.2.4). Next, we record the change of an extended UV illumination induced PSS in response to six consecutive two second 8 keV X-ray exposures, each delivering an X-ray dose of approximately 100 kGy to the sample. The acquired SAXS intensities are shown in Figure 4.16. After each X-ray exposure we observe a shift of the SAXS pattern.

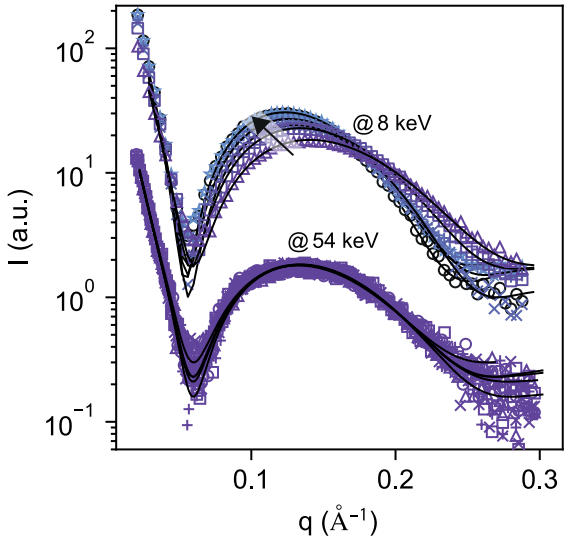

Figure 4.16.: After initial UV illumination, two different SAXS experiments are performed at 8 keV and 54 keV on azo-PC SUVs dissolved in DI water. Solid curves indicate modeling of the SAXS data by symmetrical bilayers.

To study the membrane thickness adapting after extensive X-ray exposure the described SAXS experiment at 8 keV was repeated two more times using more and prolonged X-ray exposure times (see Table A.1 for timing details). These SAXS data are shown in Figure A.1 in the Appendix.
To quantify the azo-PC membrane thickness adapting after each X-ray exposure, we model the electron density to the SAXS data shown in Figure 4.16 and Figure A.1 (cf. section 4.1.6). The resulting membrane thicknesses increase dramatically after each X-ray exposure, depending on the accumulated delivered X-ray dose (Figure 4.17). Remarkably, the azo-PC membrane yields a mean membrane thickness of $d_{HH}^{X-ray} = 42.5 \pm 0.3$ Å after extensive X-ray exposure (Figure 4.17

star and square shaped from repeated measurements, dashed line). Applying the linear correlation of the SAXS measured membrane thickness (cf. section 4.5) and the isomer ratio, reveals only 2 % *cis* isomers remain. Thus, d_{HH}^{X-ray} agrees closely with the thickness of the dark-adapted state obtained from samples after storage in the dark for several days. Here, the mean head-to-head distance calculates to $d_{HH}^{dark} = 41.9 \pm 0.9$ Å (*cis* fraction 7 %), given in Figure 4.12 (circular data points from repeated measurements, solid line).

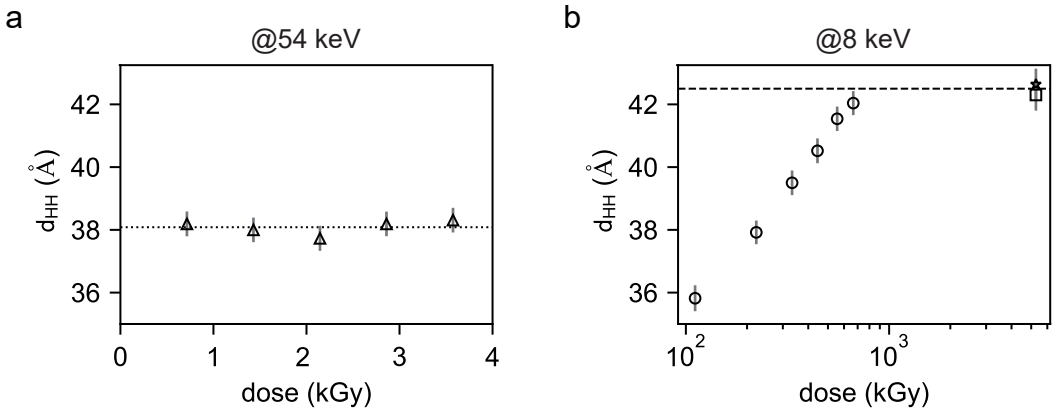

Figure 4.17.: a. Head-to-head distances d_{HH}, i.e. membrane thickness, obtained for azo-PC SUVs in DI water as function of X-ray dose measured at 54 keV. The dotted line indicates the mean value of d_{HH} for a stable UV induced PSSs. b. d_{HH} obtained for azo-PC SUVs in DI water as function of X-ray dose measured at 8 keV. The average d_{HH} after extensive 8 keV X-ray exposure is depicted as dashed line.

This is a direct indication of quantitative switching, i.e. the achievement of an all-*trans* state for photolipid membranes by soft X-ray induced catalytic switching. For azo-PC vesicles in DI water, catalytic switching enables an improved structural control, which covers 80 % of the thickness change effects achievable by ideal switching conditions.

4.7. Buffer dependent photoswitching of azobenzene lipid vesicles

As a second approach to improve the optical control of azo-PC membranes, we studied the influence of buffer conditions on the photoswitching performance. We chose two widely used buffer systems as solvent for azo-PC vesicles, PBS and a mixture of Tris with EDTA (1 x TE), as detailed in the methods section 4.1.2. The SAXS data for azo-PC vesicles in PBS and 1xTE were recorded under similar conditions as in DI water (SAXS@Elettra, 8 keV) and are shown in Figure 4.18. For each sample solution, we recorded the azo-PC vesicles in the dark-adapted state (black squares), in a *cis*-rich state obtained by prolonged (> 300 s) ex-situ UV illumination (purple crosses) and in a *trans*-rich state by blue light illumination (blue circles). For both buffer systems, we observe only a very small difference between the azo-PC membranes' SAXS signal obtained after extended blue light illumination and for the dark-adapted state.

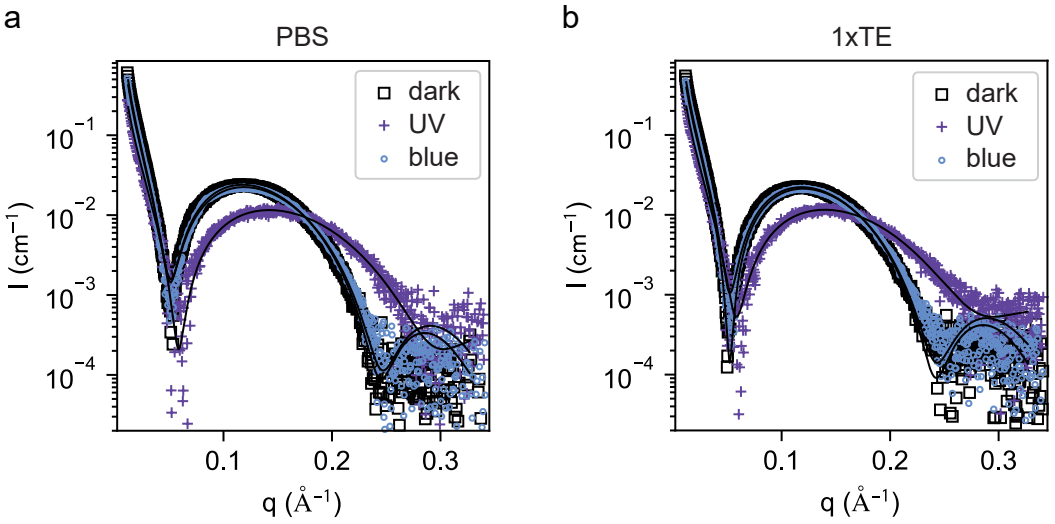

Figure 4.18.: a. SAXS intensities for azo-PC SUVs prepared in PBS b. SAXS intensities for azo-PC SUVs prepared in 1xTE buffer. The dark-adapted state, and PSSs induced by extended UV and blue light illumination (> 300 s) are shown as black squares, purple crosses and blue circles, respectively.

The analysis of the SAXS data is condensed in Figure 4.19 a. Both buffer systems exhibit similar results for the membrane thicknesses in the dark-adapted state and its changes induced by photoisomerization. For comparison with azo-PC vesicles in DI water Figure 4.12 is reprinted as Figure 4.19 b.

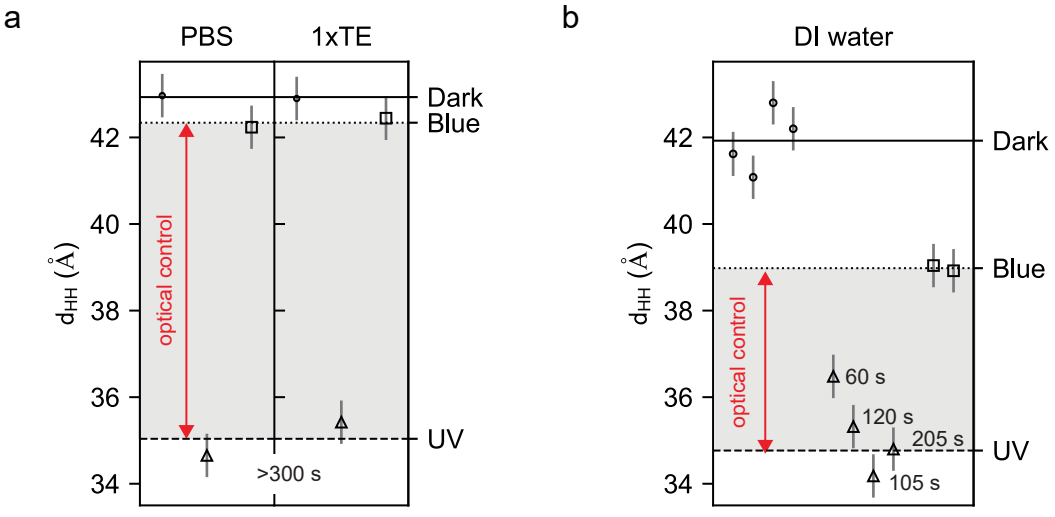

Figure 4.19.: a. Head-to-head distances d_{HH} obtained for azo-PC SUVs in PBS and 1xTE buffer. b. Reprinted Figure 4.12. d_{HH} obtained for azo-PC SUVs in DI water. The dark-adapted state, and several PSSs induced by UV and blue light are labeled accordingly. Horizontal lines indicate mean values of d_{HH} for the dark-adapted, UV, and blue light PSSs, shown as solid, dashed, and dotted line, respectively. The exposure time of UV light while approaching the PSS is indicated in seconds. The optical control window is indicated by a red double-headed arrow.

The *cis* fractions of various PSSs, calculated via the established relation between membrane thickness and *cis* fraction (cf. Figure 4.15 b), for PBS and 1xTE, as well as DI, are summarized in Table 4.2. The mean membrane thickness obtained for the dark-adapted state of azo-PC vesicles in DI water $d_{HH}^{dark}(DI) = 41.9 \pm 0.9$ Å is close to the dark-adapted calculated for azo-PC vesicles in buffered solution $d_{HH}^{dark}(PBS, 1xTE) = 42.9 \pm 0.7$ Å (Figure 4.19, circles and solid line). Also, the thickness for the UV induced PSS in DI water $d_{HH}^{UV}(DI) = 35.0 \pm 0.7$ Å is similar to the one in buffer $d_{HH}^{UV}(PBS, 1xTE) = 34.8 \pm 0.6$ Å (Figure 4.19 a,b, triangles and dashed line). As evident from Table 4.2 extended UV illumination in aqueous solution does not reach the maximal *cis* fraction of 83 % as obtained by preconditioning azo-PC in chloroform stock solutions independent of the usage of buffered systems.

	DI water		PBS /1x TE	
	d_{HH}(Å)	%*cis*	d_{HH}(Å)	%*cis*
dark-adapted	41.9 ± 0.9	7 %	42.9 ± 0.2	0 %
PSS_{UV}	34.8 ± 0.6	64 %	35.0 ± 0.4	63 %
PSS_{blue}	39.0 ± 0.3	30 %	42.3 ± 0.4	6 %
PSS_{X-ray}	42.5 ± 0.3	2 %	40.8 ± 0.3	15 %

Table 4.2.: Relevant mean head-to-head distances d_{HH} of azo-PC membranes in DI water and buffer, obtained for various PSSs and their calculated percentage of *cis* isomerization states.

For the *trans*-rich PSS induced by prolonged blue light illumination (PSS_{blue}), we discover a huge difference in *cis* fraction according to buffered or deionized aqueous solution. By continuous blue light illumination in DI water, we are able to increase the membrane thickness up to $d_{HH}^{blue}(DI) = 39.0 \pm 0.3$ Å (Figure 4.19 b, squares and dotted line), i.e. the *cis* azo-PC content is still 30 %. Instead, in buffered solution, the membrane thickness increases to $d_{HH}^{blue}(PBS, 1xTE) = 42.3 \pm 0.4$ Å (Figure 4.19 a, squares and dotted line), i.e. the *cis* fraction here is only 3 %. The optical control (Figure 4.19, double headed red arrow) is highly efficient in buffered systems and significantly improved compared to DI water.

4.8. Buffer dependent catalytic switching of azobenzene lipid vesicles

In the context of X-ray dose effects on soft matter samples we investigated, if common buffer systems like PBS and 1xTE buffer provide sufficient buffer capacity to suppress radical induced catalytic backswitching of azo-PC SUVs. Therefore, X-ray dosing experiments described in 4.6 were repeated for photolipid vesicles dissolved in buffered solutions.
Here, azo-PC vesicles with high *cis* fraction were prepared by prolonged (> 300 s) ex-situ UV illumination and subsequently exposed to 8-10 consecutive soft X-ray measurements of 5 s (8 keV). Thus, we again exploited the production of reductive and oxidative species by soft X-rays, which has been proven to trigger catalytic backswitching for azo-PC vesicles in DI water (cf. section

4.6). The corresponding SAXS intensities for both buffer systems are given in Figure 4.20. For each sample solution the dark-adapted state is shown as black, the *cis*-rich state as purple, and the consecutive X-ray exposures as gray solid lines. Similar to azo-PC membranes in DI water (cf. Figure A.1 b), we observe a shift of the SAXS pattern for each X-ray exposure for both buffer solutions. However, in contrast to the catalytic switching experiments in DI water (cf. Figure A.1 b) the SAXS data obtained after extended X-ray exposure, i.e. the deposition of an accumulated X-ray dose $> 1000\,\mathrm{kGy}$, (gray lines) do not match the SAXS pattern of the dark-adapted state (black line).

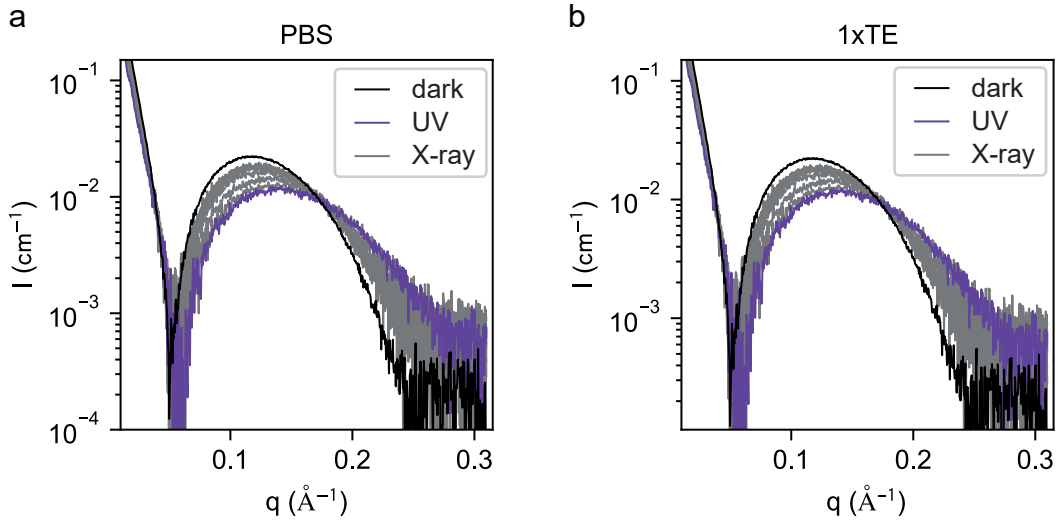

Figure 4.20.: a. SAXS measurements on azo-PC SUVs in PBS. b. SAXS measurements on azo-PC SUVs in 1xTE buffer. The dark state and PSSs induced by extended ex-situ UV light illumination ($> 300\,\mathrm{s}$) and 8-10 subsequent consecutive 5 s X-ray exposures are shown as black, purple and gray lines, respectively.

To quantify the thickness change of the photomembranes upon radical formation by X-rays under buffered conditions, we model and extract the head-to-head distances d_{HH} as function of X-ray dose (Figure 4.21). For comparison, the membrane thickness obtained from azo-PC SUVs in DI water (cf. Figure 4.12 b) is added to Figure 4.21 as square shaped data points.
Similar to azo-PC membranes in DI water, we find an increase in the membrane thickness of azo-PC SUVs dissolved in buffered systems for each X-ray exposure. Thus, neither PBS (gray triangles) nor 1xTE buffer (blue circles) are able to fully suppress water radical formation upon X-ray exposure. However, buffered vesicle solutions seem to decelerates catalytic switching substantially. For example, the deposition of an X-ray dose of $\sim 350\,\mathrm{kGy}$ to azo-PC membranes yields the smallest head-to-head distance for PBS, followed by 1xTE and the thickest membrane for DI water (cf. Figure 4.21, filled data points). One can furthermore observe that the azo-PC membrane thickness, when using DI water as solvent, $d_{HH}^{DIwater}$ increases faster as response of the delivered X-ray dose. Most remarkably, we find an azo-PC membrane thickness after extensive

X-ray exposure of $d_{HH}^{DIwater}(> 1000\,kGy) = 42.5 \pm 0.3$ Å (*cis* fraction 2 %) for DI water and of $d_{HH}^{PBS,1xTE}(> 1000\,kGy) = 40.8 \pm 0.4$ Å for buffered solutions, i.e. 15 % *cis* isomer still remains (Figure 4.21, dashed and dotted line and Table 4.2). Hence, extensive X-ray exposure also induces catalytic switching in azo-PC membranes under buffered conditions, but it is not quantitative, i.e. an all-*trans* state is not achieved.

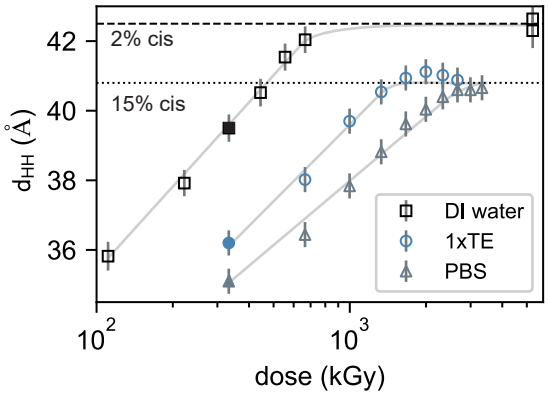

Figure 4.21.: Head-to-head distances d_{HH}, i.e. membrane thicknesses, obtained for azo-PC SUVs in DI water (black squares), PBS (gray triangles) and 1xTE buffer (blue circles) as function of X-ray dose. The mean value for the X-ray induced thickness under buffered conditions $d_{HH}(buffer)$ is indicated as dotted line. The mean value for the X-ray induced thickness of azo-PC membranes in DI water $d_{HH}(DIwater)$ is indicated as dashed line. Grey solid lines serve as guide to the eye.

4.9. Conclusion and discussion

Within this thesis, it was proven for the first time that photoswitching enables the tuning of lipid bilayer thickness with high accuracy and without the need to change the bilayer composition or its environment. SAXS provides a direct readout of the azo-PC membrane bilayer thickness, which is shown to have a linear correlation to photolipid isomerization fraction. This referencing method is novel in this field and enables the determination of the *trans*/*cis* ratio of azo-PC vesicles for various PSSs for the first time. It may further prove generally useful for analysis of systems where measurements in bulk (e.g. membrane UV-Vis spectra) cannot be interpreted with reference to more easily characterized molecular measurements (e.g. UV-Vis spectra in monomer solution).
The 8 Å thickness change accessible to azo-PC membranes under ideal photoswitching conditions (20 % of membrane thickness) is massive and far beyond the effects achievable by temperature variations [130], non-equilibrium temperature-jump techniques [131, 132] or the condensing effect induced by cholesterol concentrations up to 45mol % in phospholipid bilayers [129, 133, 134]. Only the application of high pressure and pressure-jumps might be in the same variation range. However, these are typically induced by major phase transitions (gel-to-fluid phase) and have not been reported for unilamellar bilayers in a reversible manner, yet [135–137]. Hydrophobic match-

ing of membrane thickness with *trans*-membrane proteins is thus a wide research field that could benefit enormously from the large thickness change effects observed here [138].

The huge membrane thickness change may benefit from ordering effects in the *trans* state related to H-aggregate formation. Parallel aligned *trans* state azobenzenes, as in a lipid bilayer, are known to exhibit dipole-dipole interactions, so called H-aggregates (H = 'hypsochromic') [139]. These exhibit a blue, so-called hypsochromic, shift of the $\pi\pi^*$ absorbance band [96]. A decreasing hypsochromic shift is characteristic for H-aggregate melting and has been observed for *trans*-rich membranes at higher temperatures and accompanied by an increasing diffusion constant due to higher lipid mobility [11]. H-aggregate melting may be confirmed as a membrane thinning effect for all-*trans* azo-PC membranes at higher temperatures. This may be a valuable experiment in the future [140, 141].

To exploit the full thickness change effects by photoswitching, efficiency of *trans*-to-*cis* isomerization of azo-PC still needs to be improved. In both DI water and buffered solutions, the UV light PSSs in azo-PC membranes (max. 64 % *cis*) remain below the theoretical limit (83 % *cis*) and below values reported by others [90, 107]. Also, the *cis* fraction of the mostly-*cis* azo-PC stock solution, i.e. azo-PC dissolved in chloroform, remains noticeably below the predicted values of 95 % for azobenzene [105]. This may on the one side be a consequence of azobenzenes' incorporation into a phospholipid, as substituents are known to alter the isomerization yields. On the other side this may be a result of high lipid or vesicle concentrations in the photoswitching experiments. The latter may be improved by using LEDs with higher irradiance rate.

In solutions with ionic strength, the blue light PSSs (3 % residual *cis*) approach the dark-adapted state (0 % residual *cis*), i.e. photoswitching experiments in physiologically stabilized environments are efficient. This sensitivity of azobenzene inside the lipid membrane to the aqueous buffer conditions outside was unexpected and has so far not been reported. Investigated factors, which influence the photoisomerization and thermal relaxation yields of azobenzene in solution, are polarity and viscosity [114, 142–144], temperature [145, 146], hydrogen-bonding effects [147, 148], and electronic interaction as well as steric hindrance as consequence of densely packed azobenzene substitutes [149, 150]. However, none of them deal with optically dense, ordered anisotropic azobenzene assemblies such as azo-PC membranes. Apart from the optical control, there are some more differences of general membrane properties between buffered and deionized azo-PC SUVs solution to be observed. We find for example an increased membrane thickness for the dark-adapted state of the buffered system ($d_{HH}^{dark}(PBS, 1xTE) = 42.9 \pm 0.7$ Å vs. $d_{HH}^{dark}(DI) = 41.9 \pm 0.9$ Å). Furthermore, unilamellar vesicles are easier to form in DI water, which may be a result of decreased bending rigidity. In contrast, extremely well-ordered lipid multilayers can exclusively be prepared in solutions with high ionic strength. These indication are in line with well-known salt-induced effects on lipid bilayers, such as increased lipid chain order [151, 152], decreased lateral lipid mobility [153], rigidification [154], membrane thickening [152], and changes in vesicles size [155]. There is much evidence, both experimentally and

from simulations that these salt-induced changes in structure and dynamic of lipid bilayers are caused by ions penetrating deep into the lipid bilayer and their formation of tight ion-lipid complexes in the lipid head region [151, 156]. The ion-lipid complexes are furthermore likely to influence the intramembrane dipole potential and its dielectric properties [156–159]. Thus, the difference in photoswitching efficiency in DI water and in buffered solutions seems be a consequence of salt-induced changes in the dielectric environment of the azo-PC's membrane, which in turn affect the photoisomerization yields of azobenzene.

The blue light PSSs of vesicles in DI water (30 % residual *cis*) do not approach the dark-adapted state. For this purpose, quantitative *cis*-to-*trans* switching schemes are needed. Here, soft X-ray (8 keV) are demonstrated to induce quantitative switching for azo-PC SUVs in DI water, which has not been realized before. We attribute this to radical redox reactions following the X-ray dose deposition in the medium. Thus, this work provides a proof-of-principle that catalytic backswitching can indeed be utilized in optically dense systems with a high impact on the accessible control of photomaterials. For higher X-ray energies such as 17.4 keV and 54 keV, we do not observe such catalytic backswitching, which also highlights the versatility of high energy X-rays as low-dose probes. These experiments further demonstrate that high quality SAXS data may be obtained even for weakly scattering biological samples.

For azo-PC membranes in buffered solutions, a decelerated, non-quantitative catalytic backswitching was observed. PBS provides slightly better buffing capacities than 1xTE buffer. However, catalytic backswitching could not be fully suppressed by the use of buffered solutions. Although, buffer systems together with short X-ray exposure times might compensate some of the effects of soft X-rays on soft matter samples high energy X-rays outperform commonly used buffer solutions in their ability to prevent radiation damage by far.

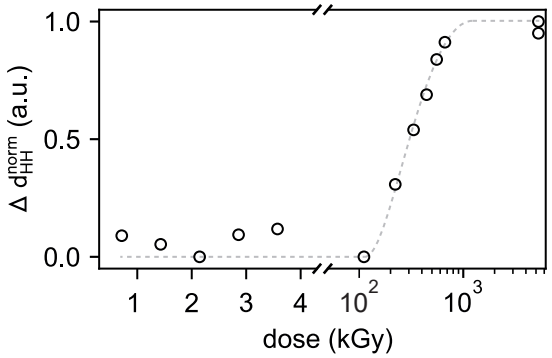

Figure 4.22.: Normalized change in d_{HH} for azo-PC SUVs in DI water as function of X-ray dose obtained from data shown in Figure 4.17. Up to a dose of 100 kGy the photolipid membrane remains stable in a *cis*-rich PSS. Above 100 kGy the membrane thickness changes in response to catalytic cis-to-trans switching by X-rays. No change in membrane thickness corresponds to a constant *cis*-rich PSS, whereas maximum change corresponds to the dark-adapted PSS. Thereby, azo-PC SUVs are suitable as X-ray dose reporters. Dashed lines serve as guide to the eye.

In context of catalytic switching it is important to emphasize that X-ray induced changes in photomembranes are fully reversible, in contrast to irreversible radiation damage, e.g., protein aggregation. In the light of these findings, we propose that azo-PC SUVs may serve as dose reporters. Hence, the measurement of azo-PC *cis*-to-*trans* transition for SUVs in DI water allows to read off the effective X-ray dose up to 6000 kGy by determination of the normalized change in membrane thickness as shown in Figure 4.22. Here, the normalized change in membrane thickness is obtained from data shown in Figure 4.17. Starting from a *cis*-rich state induced by UV illumination, no change in membrane thickness corresponds to a constant *cis*-rich PSS, i.e. a thin photomembrane, whereas maximum change correspond to a dark-adapted, all-*trans* PSS. This may help to calibrate critical doses for biological SAXS experiments, as they are, due to the samples' complexities and impossibility to measure the exact photon flux at most beamlines, notoriously difficult to calculate. Critical doses for biological samples discussed range from 2.37 - 51.24 kGy [34], 400 kGy [26] and 284 - 7056 kGy [25], most of them well within the dose range accessible by azo-PC SUVs dose reporters.

For red-azo-PC membranes in DI water, SAXS measurements unravel only a slight variation in thickness in response to photoisomerization. However, this is not surprising, because *trans*-red-azo-PC photolipids have a rather twisted geometry, compared to the 'standard' azo-PC, due to steric hindrance between the large chlorine substituents [160]. This skewed conformation is likely to diminish the impact of photoisomerization on the red-azo-PC membranes configuration. However both, fluidity of a supported lipid bilayer and the stiffness of giant unilamellar vesicless (GUVs) can be altered significantly via photoisomerization, which leaves red-azo-PC still as a promising candidate as light sensitive reagent for biological in vivo applications [12]. Furthermore, their light-driven thickness control in DI water may be improved for aqueous solutions with higher ionic strengths.

5. SILICIFICATION OF DNA ORIGAMI OBJECTS

The work in this chapter is partly published as preprint [1], which is attached in Appendix B.

The DNA origami technique [161, 162] has proven to be a versatile bottom-up fabrication method to engineer nanometer-size objects with unprecedented precision, utilizing the programmable self-assembly of complementary DNA strands [163]. A long single-stranded DNA scaffold is folded into a desired shape by short DNA staples strands that can only bind at specific points along the scaffold. After 15 years of development a plethora of DNA nanostructures with different sizes, shapes and complexity have been presented [164–167]. Many of those have been used as template for nanoparticles [168, 169], fluorescent dyes [170, 171] or protein assembly [172, 173]. Potential application of these DNA origami objects include areas such as biophysics [174], biosensing [175, 176], drug delivery as well as biomedical applications [177–179], and nanophotonics [57, 180].

Despite the huge variety of applications, the DNA origami technique is still hindered to reach its full potential by its limited chemical, thermal and mechanical stability. Especially in a biological environment DNA origami objects suffer from susceptibility to enzyme degradation [181, 182] and their structural stability is limited to high-salt concentrations and ambient temperatures [7]. On the other hand, for material applications, potential devices are restricted to operate in aqueous surroundings to maintain their physical performance and rigidity.

The encapsulation of DNA origami constructs with silica has been recently attracted significant interest. It is a promising protection strategy to help DNA origami survive low-salt, high-heat conditions, and display an increased resistivity to nuclease-mediated degradation [183, 184]. Mechanical reinforcement of e.g 3D silica-DNA crystals has been demonstrated as those otherwise very fragile structures could be preserved in a dry state [183, 185]. Moreover, play silicificated DNA origami structures an important role for the customized synthesis of inorganic non-metallic 2D [186, 187] and 3D nanomaterials [179, 188, 189].

Nguyen et al. were the first to show that single DNA origami objects undergo silicification in a low Mg^{2+} solution by sol-gel chemistry (cf. Figure 5.1) [183]. Here, a modified Stöber method [190], which involves a hydrolysis and condensation reaction of silanes, is utilized for silica synthesis. However, the silica species involved in this reaction are negatively charged and can therefore not accumulate around anionic DNA. This problem is resolved by employing a positively charged co-structure directing agent (CSDA), i.e. N-trimethoxysilylpropyl-N,N,N-trimethylammonium chloride (TMAPS. TMAPS is capable of electrostatic attraction to the anionic DNA backbone and imparts siloxane groups as co-condensation sites for a silica precursor. Using tetraethoxy or-

thosilicate (TEOS) as silica source enables its growth directly on the DNA structure and results in highly stable silica encapsulated structures (origami@SiO_2) as illustrated in Figure 5.1.

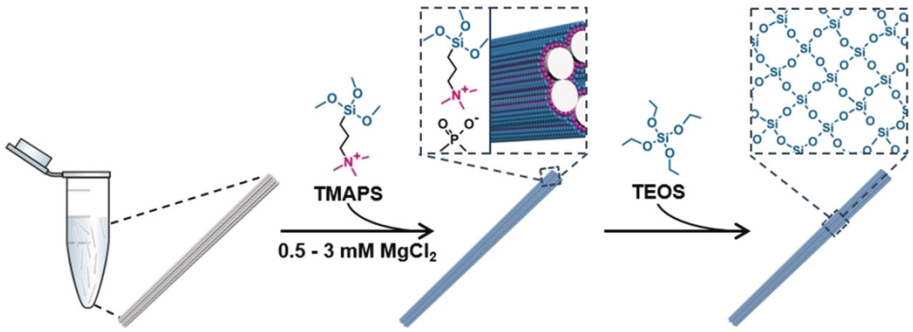

Figure 5.1.: Illustration of the strategy for encapsulating DNA origami in silica. The DNA origami objects are dispersed in a low Mg^{2+} solution before the addition of TMAPS. In a second step, TEOS is added to promote silica growth directed by the DNA origami template. Taken from [183].

The analysis of the structure of origami@SiO_2 has so far been based on transmission electron microscopy (TEM), scanning electron microscopy (SEM) and atomic force microscopy (AFM) studies and focused on evidence for increased structural integrity and the determination of a silica shell thickness. Despite important advancements, achieving controlled silicification in solution has remained challenging. Reported technical problems are, e.g. an incomplete silica coating [179], silica agglomeration, or deformation of the DNA origami objects after silicification [183]. So far, a homogeneous silica encapsulation for 14 and 24 helix-bundles@SiO_2, 13 and 14 helix-rings@SiO_2, and DNA crystals@SiO_2 in the subnanometer range and beyond has been reported [183, 184].

However, TEM, SEM, and AFM are limited to measurements of the dry state under vacuum conditions and do not provide reliable Angström resolution [183]. Moreover, no study on the impact of silicification on the inner origami fine structure has been performed, yet. Clearly, to understand the silicification mechanism it is instructive to monitor the structural changes of DNA origami in-situ during the silica growth, as even moderate shape and structure changes will have an impact on the use of origami@SiO_2 as platforms in biomedical applications [177].

Furthermore, it has been demonstrated by MD simulations and SAXS that the presence of ions in the buffer solution strongly influence the overall shape and the inner helix structure of DNA origami objects [7, 191, 192]. Thus, investigating the influence of the positively net-charged TMAPS on the bare origami shape and inner lattice structure prior the formation of silica will provide further insights on the silicification process. Non-invasive in-situ structure studies of organic-inorganic nanocomposite particle formation as well as solvent induced changes of their internal organic 3D strucutre are a challenging task. However, SAXS has been proven to be a valuable tool to investigate DNA origami objects [7–9] as well as to monitor nanocomposite particle formation [193, 194] in the past.

In the following, the change of the overall shape and the inner fine structure of three prototypic DNA origami objects in response to silicification in solution are determined by in-situ SAXS experiments. The net-cationic silica precursor TMAPS could be identified to induce condensation of the DNA origami shape and its inner helix spacing in the beginning of the silicification reaction. Subsequently, a shape re-expansion due to TEOS driven silica deposition is observed. X-ray contrast matching indicates that the silica forms inside and outside of the DNA origami. The inner order of the origami and the overall shape is well-preserved. Furthermore, the silica penetration into the DNA origami object is identified to stabilize the structure from inside and serves as the main indicator for increased thermal stability up to 60°C. Moreover, DNA origami with flat surfaces show increased tendency towards aggregation during silicification. Also, the precursor ratio was identified as crucial and very sensitive parameter to achieve conformal silica growth and a reliable outer encapsulation thickness of subnanometer thickness.

5.1. Preparation and structure analysis of silica-coated DNA origami

In total, three prototypic DNA origami structures of rather simple shapes with two different lattice arrangements are prepared: a cylinder-shaped 24 helix-bundle (24-HB) with honeycomb lattice design, a four layer bloc (4-LB) with honeycomb lattice design, and a three layer bloc (3-LB) with square lattice design.

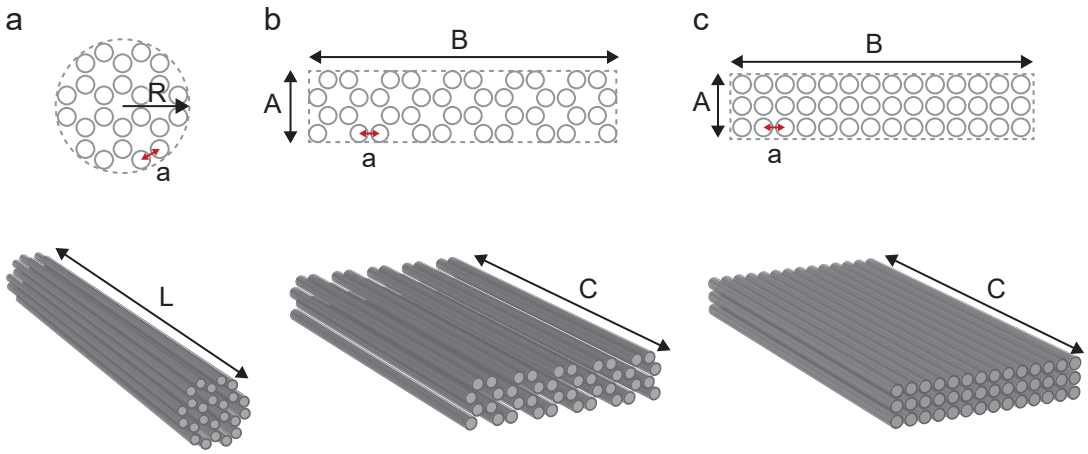

Figure 5.2.: Schematic DNA origami shapes and front views of a 24-HB with honeycomb lattice design (a), a 4-LB with honeycomb lattice design (b) and a 3-LB with square lattice design (c) are shown. Each solid cylinder represents a DNA double helix.

All three DNA origami structures and their front view are schematically shown in Figure 5.2 and their dimensions by design are given in Table 5.1.

DNA origami	A (Å)	B (Å)	C (Å)	R (Å)	L (Å)	#(helices)
24-HB	-	-	-	79	~ 1000	24
4-LB	78	270	571	-	-	40
3-LB	72	358	571	-	-	42

Table 5.1.: DNA origami dimensions by design. The values are calculated in Angström by assuming a base pair distance of 3.4 Å, an average inter-helical distance of 2.6 nm and a radius of a DNA double helix of 1 nm.

5.1.1. *Folding and purification of DNA origami*

Monitoring the DNA origami silicification by SAXS requires well-dispersed and highly concentrated origami solutions. The folding, purification and concentration of the here studied origami objects were partly done by the Heuer-Jungemann group.

24 helix-bundle

The 24-HB structure was folded using 30 nM of the scaffold p8064 (tilibit nanosystems GmbH, Germany) and 100 nM of each staple oligonucleotide (Eurofins Genomics Germany GmbH and Integrated DNA Technologies, Inc., USA) in buffer containing 400 mM Tris-Acetat, 1 mM EDTA (pH = 8) and 14 mM $MgCl_2$. The mixture was heated to 65 $^\circ C$ and held at this temperature for 15 min, then slowly cooled down to 4 $^\circ C$ over a period of 15h. For details see [7]. The 24-HBs were concentrated and purified from excess staples by two rounds of PEG precipitation and re-dispersion in buffer (1x TE, 3 mM $MgCl_2$).
In brief, the origami folding solution was mixed in a 1:1 volumetric ratio with PEG precipitation buffer (15 % w/v PEG (MW: 8000 g/mol), 500 mM NaCl, 2xTE), adjusted to a $MgCl_2$ concentration of 10 mM and centrifuged at 16000 rcf for 25 min. The supernatant was removed and the DNA pellet re-suspended in 0.5 ml 1x TE buffer with 11 mM $MgCl_2$. After 30 min of shaking the PEG precipitation step was repeated and the purified structures were re-suspended in the final buffer (1x TE, 3 mM $MgCl_2$). The origami solution was incubated for 24 h shaking at room temperature with 350 rpm. This way, concentration of the origami solution up to 270 nM (1.4 g/l) and purification from excess staples are managed in one step. The concentration of the purified DNA origami solution was measured via a absorption measurement (Thermo Scientific NanoDrop 1000 Spectrophotometer) of wavelength 260 nm.

Three layer bloc

The 3-LB origami was prepared in two different ways. For in-situ silicification monitored by SAXS, the 3-LB was folded using 30 nM of the scaffold p8064 (tilibit nanosystems GmbH, Germany), 100 nM of each staple oligonucleotide (Eurofins Genomics Germany GmbH and Integrated DNA Technologies, Inc., USA) in buffer containing 400 mM Tris-Acetat, 1 mM EDTA (pH = 8) and 14 mM $MgCl_2$ and exposed to the same temperature ramp as the 24-HB [7]. Concentration

and purification of the origami solution from excess staples was, again, performed by two rounds of PEG precipitation (see paragraph 5.1.1 - 24 helix-bundle).
Secondly, readily silicificated 3-LB samples (3-LB@silcia) were prepared in collaboration with the Heuer-Jungemann group. Here, the 3-LB was folded using 10 nM of the scaffold p8064 (tilibit nanosystems GmbH, Germany), 100 nM of each staple oligonucleotide (Eurofins Genomics Germany GmbH and Integrated DNA Technologies, Inc., USA) in buffer containing 400 mM Tris-Acetat, 1 mM EDTA (pH = 8) and 18 mM $MgCl_2$. The mixture was heated to 67 °*C* and held at this temperature for 15 min, then slowly cooled down to 4 °*C* over a period of 15 h. The 3-LB structures were purified from excess staples by Amicon filtration, silicificated over several days, and in a final step concentrated again by Amicon filtration.
For Amicon filtration, the folding mixture ($\sim 2\,ml$) was divided over 4-5 Amicon Ultra filters (0.5 ml, 100K, Millipore, USA) and each centrifuged at 8000rcf for 8 min. The centrifugal steps were repeated 3-5 times with fresh buffer (1xTAE, 3 mM $MgCl_2$) added in every step. The resulting solution ($\sim$ 30 µl) were re-suspended in buffer and the procedure repeated. This way, a purified origami solution with of 100-120 µl in total with a concentration up to 270 nM (1.4 g/l) was collected. Purification and concentration by Amicon filtration introduces in contrast to the PEG precipitation technique fewer aggregates in the origami solution.

Four layer bloc

The 4-LB structure was developed and prepared by the Heuer-Jungemann group. Here, the 4-LB was folded using 10 nM of the scaffold p8064 (tilibit nanosystems GmbH, Germany), 100 nM of each staple oligonucleotide (Integrated DNA Technologies, Inc., USA) in buffer containing 40 mM Tris, 20 mM Acetic Acid, 1 mM EDTA (pH = 8) and 18 mM $MgCl_2$. The mixture was heated to 65 °*C* and held at this temperature for 15 min, then slowly cooled down to 20 °*C* over a period of 16 h. The 4-LB origami solution were concentrated and purified from excess staples by two rounds of Amicon filtration for the in-situ SAXS experiments as described for the 3-LB in paragraph 5.1.1 - Three layer bloc. To prepare 4-LB@SiO_2 the purified structures were silicificated before they were concentrated.

5.1.2. *Silica coating*

For silica coating, two silanes N-trimethoxysilylpropyl-N, N, N-trimethylammonium chloride (TMAPS) (TCI, USA) and tetraethoxy orthosilicate (TEOS) (Sigma Aldrich, USA) were added to the purified origami solutions in a ratio of 1 phosphate group/ nucleotide: 5 TMAPS : 12.5 TEOS. While the positively charged TMAPS acts as CSDA, which is electrostatically attracted to the polyanionic DNA backbone, TEOS leads to a formation of a silica network on the DNA helices.
For in-situ silicification experiments 110 µl of purified DNA origami structures (270 nM) were

mixed with 0.67 µl TMAPS (50 % in methanol) and shaken at 350 rpm for 1 min in an Eppendorf tube. For in-situ silicification of 24-HBs, 2.67 µl TEOS (50 % in methanol) were added followed by shaking for 15 min. Finally, the sample solution was transferred to a SAXS sample chamber. As the 3-LB and the 4-LB structures appeared to be very sensitive to movement of the complete silicification mixture, the only TMAPS containing origami solution was here transferred to the SAXS chamber prior to the addition of TEOS. For ex-situ SAXS measurements on 3-LB@SiO_2 and the 4-LB@SiO_2 the reaction mixture was kept undisturbed for 3 days.

5.1.3. *Experimental consideration and details*

A long-term SAXS experiment such as monitoring the encapsulation of DNA origami objects in-situ can, due to the limited beam time availability at third-generation synchrotron sources, exclusively be performed at anode-based laboratory setups. After, the usage of a Mo-sourced (17keV) instead of a common Cu-sourced (8keV) laboratory SAXS setup provides some important benefits due to the higher X-ray beam energy.

First, origami@SiO_2 undergo fast sedimentation. Hence, without intervention, the amount of material in the X-ray beam and consequently the scattering intensity is constantly reduced during the experiment. To prevent sedimentation, simple rotation of the sample solution around the beam axis has proven to overcome this issue [195]. Therefore, we built a tumbler, which rotates the sample chamber with 50 rpm centered around the X-ray beam as shown in Figure 2.3 [196]. Again, this is an example for a complex sample installation, which requires a spacious environment only available at SAXS setups using higher X-ray energies (cf. section 2.2.1). A further important criterion for the tumbler was its reliable operation with low risk of failure for measuring periods up to a week. Apart from mechanical stability, this included the prevention of evaporation of the sample solution and the formation of air bubbles. This is difficult to achieve for sample thicknesses of less than 5 mm as required for Cu-sourced setups.

Second, collecting SAXS data over several days deposits a significant amount of X-ray dose in the sample. Hence, reducing the dose rate of the X-ray beam is essential to prevent radiation damage. As discussed in detail in section 2.2.4 radiation damage is mostly a result of secondary electrons caused by photoelectric absorption. Due to the decreasing probability of photoelectric absorption with increasing incident energy(cf. Figure 2.7), the dose rate of a 17.4keV (Mo-source) X-ray beam is drastically reduced compared to an 8keV (Cu-source) beam.

Thus, measuring periods of several days, the prevention of sample sedimentation by the usage of a tumbler and the avoidance of radiation damage made a Mo-source laboratory setup the favorable choice for in-situ SAXS experiments on origami@SiO_2.

However, to resolve not only the overall DNA origami shape, but also its inner helix arrangement, the experiment further relied on the availability of a maximum q-value of at least $q_{max} = 0.3\,\text{Å}^{-1}$. Here, q_{max} is given by the interhelical peak of the squared lattice arrangement of the 3-LB as described in section 5.1.4 with $q_{max} = 2\pi/a_{sq}$ and $a_{sq} \approx 2.9\,\text{nm}$. As detailed in section 2.2.2 the

desired minimal q-value q_{min} calculates via $q_{min} = 1/D_{max}$ to $10^{-3}\,\text{Å}^{-1}$ for $D_{max} = L = 1000\,\text{Å}$. Clearly, this value is to large to be reliable resolved by laboratory SAXS experiments. However, the smaller shape dimensions, such as the cylinder radius of the 24-HBs and the cuboid height of the 3-LBs and 4-LBs, can be determined with Angström precision as demonstrated in the past [7, 49, 197].

Thus, X-ray data were recorded at our Mo-source laboratory SAXS setup with an X-ray beam energy of 17.4keV and a beam size of 1.0 x 1.0 mm^2 [6]. The SDD was 1m. Data were recorded using a Dectris Pilatus 3 R 300K CMOS detector (487 x 619 pixels of size 172 x 172 μm^2). During the first 24 h of silica growth the in-situ SAXS data were averaged over 2 h, subsequently over 8 h.

5.1.4. *Data analysis*

Model fitting

All DNA origami dimensions, as well as their inner structure, are obtained from model fits of the scattering intensity $I(q)$ to a geometrical model describing the overall origami shape with additional peaks accounting for the inner helix arrangement [7]. The scattering intensity is given in dependence of the scattering vector $q = |\vec{q}| = \frac{4\pi}{\lambda}\sin(2\theta/2)$. Here, λ is the X-ray wavelength and 2θ the scattering angle.

To analyze the scattering data of 24-HB@SiO_2, we use a cylinder model together with a Debye background to account for free oligonucleotides, a power law to include the effects of aggregation, and Lorentzian peaks to account for the inner honeycomb lattice structure, as given in Equations 5.1 - 5.5.

$$I(q) \propto \frac{s_{cyl}}{V_{cyl}} \int_0^{\pi/2} F_{cyl}^2(q)\sin(\alpha)d\alpha + s_{deb}F_{deb}(q) + s_{pow}F_{pow}(q) + s_{hk}F_{lor}(q) \tag{5.1}$$

$$F_{cyl}(q) = (\rho_{DNA} - \rho_w)V_{cyl}\frac{\sin(q\frac{L}{2}\cos(\alpha))}{q\frac{L}{2}\cos(\alpha)}\frac{2J_1(qR\sin(\alpha))}{qR\sin(\alpha)} \tag{5.2}$$

Here, J_1 is the first order Bessel function, α the angle between the cylinder axis and the q-vector, L the length of the cylinder core, R the radius of the cylinder core, V_{cyl} is the cylinder volume and ρ_{DNA}/ρ_w the scattering length density of DNA and water, respectively.

$$F_{deb}(q) = \frac{2(\exp(-q^2R_g^2) - 1 + q^2R_g^2)}{(q^2R_g^2)^2} \tag{5.3}$$

$$F_{pow}(q) = q^{-x} \tag{5.4}$$

R_g is the radius of gyration and x the power law exponent.

$$F_{lor}(q) = \frac{1}{1+(\frac{q-q_0}{B})^2} \tag{5.5}$$

Here, q_0 is the peak position and B the half-width-half-maximum of the Lorentzian peak. q_0 is directly related to the lattice spacing d via $d = 2\pi/q_0$. For DNA origamis with a honeycomb lattice design, i.e. the 24-HB and the 4-LB, $a_{hc} = \sqrt{4/9}\,d = 2/3 \cdot 2\pi/q_0$ as a result of the relation $1/d^2 = 4/3 \cdot (h^2+hk+k^2)/a_{hc}^2$ which is valid for a 2D honeycomb lattice with h and k as Miller indices.

To analyze the data of 3-LB@SiO_2 and 4-LB@SiO_2 a cuboid model as given in Equation 5.6 and 5.7 is used instead of the cylinder model [198].

$$F_{cuboid}(q) = \int_0^1 \Phi_q(\mu\sqrt{1-\sigma^2}, a)\left[S\left(\frac{\mu c\sigma}{2}\right)\right]^2 d\sigma \tag{5.6}$$

$$\text{with } \Phi_q(\mu,a) = \int_0^1 \left\{S\left[\frac{\mu}{2}\cos(\frac{\pi}{2}u)\right] S\left[\frac{\mu a}{2}\sin(\frac{\pi}{2}u)\right]\right\}^2 du, \tag{5.7}$$

$$S(x) = \frac{\sin(x)}{x}, \text{ and } \mu = qB.$$

The substitution of $\sigma = \cos(\alpha)$ and $\beta = \pi u/2$ are applied. Here, A, B, and C are the axis dimensions of the cuboid, as schematically shown in Figure 5.2, α the angle between C and $\overrightarrow{q}$, and β the angle between the projection of the particles in the xy-plane and the y-axis. Furthermore, $a = A/B < 1$, $b = B/B = 1$ and $c = C/B > 1$ is assumed (cf. Figure 5.3).

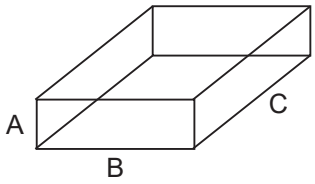

Figure 5.3.: Cuboid with the corresponding definition of sides.

For the squared lattice arrangement of the 3-LB the interhelical distance is calculated via $a_{sq} = d = 2\pi/q_0$.

Parameter	ρ_{DNA}	ρ_w	L_{24HB}	B_{3-LB}	C_{3-LB}	B_{4-LB}	C_{4-LB}
Value	$13 \times 10^{-6}\,\text{Å}^{-2}$	$9.4 \times 10^{-6}\,\text{Å}^{-2}$	1000 Å	379 Å	627 Å	379 Å	555 Å

Table 5.2.: Fixed model fitting values for data analysis of SAXS experiments on origami@SiO_2.

During the model fitting the electron density of the DNA ρ_{DNA} and the water ρ_w, the length of the 24-HB L and the widths B and C of the 3-LB and 4-LB were fixed as listed in Table 5.2. Model fitting was achieved by running the software-internal population-based DREAM algorithm using the software package SasView [71].

Porod invariant

The Porod invariant Q is a model-free measure of the total scattering contrast, which enables here to monitor the silica growth. For a two-phase system it is calculated via

$$Q = \int_0^\infty I(q)q^2 dq \propto 2\pi^2 \Delta\rho^2. \tag{5.8}$$

The calculation of Q relies on the extrapolation of the experimental scattering data $I(q)$ to small and large q. For extrapolation to small q, we fit the data to the Guinier function $I(q) = I_0 \cdot \exp\left(-\frac{q^2 R_g^2}{3}\right)$. Here, R_g denotes the radius of gyration, which quantifies the objects distribution of electron density. The extrapolation of the data to large q is omitted due to increased noise and therefore the integration limited to $q_{max} = 0.35\,\text{Å}^{-1}$. This way, the Porod invariant Q(t) is obtained as function of silicification time [18, 199]. The Porod invariant was calculated using the software package SasView [71].

Contrast matching

The concept of contrast matching, i.e. the vanishing of the scattering contrast between the DNA helices and their surrounding matrix, can be utilized to estimate the volume fraction of silica grown on the individual DNA helices.

$$x_{SiO_2} \cdot \rho_{SiO_2} + x_{H_2O} \cdot \rho_{H_2O} = \rho_{DNA}. \tag{5.9}$$

For contrast matching, the volume fraction weighted electron density of water ρ_{H_2O} and silica ρ_{SiO_2} is equal to the electron density of DNA ρ_{DNA} (cf. Equation 5.9). Here, x_{SiO_2} denotes the volume fraction of silica and x_{H_2O} denotes the volume fraction of water. With $x_{H2O} = 1 - x_{SiO2}$ the Equation 5.9 can be solved for x_{SiO2}.

5.2. Silicification of 24 helix-bundles

To reveal the effect of silica encapsulation on the overall DNA origami shape and its inner lattice arrangement, we monitored the silicification of 24-HBs over several days by SAXS. Therefore, highly concentrated 24-HBs were prepared in low Mg^{2+} buffer (1x TE buffer, 3 mM $MgCl_2$) following a protocol described in section 5.1.1. The silica growth was initiated by the addition of two precursors, first, TMAPS and, second, TEOS to the origami solution (see section 5.1.2). Due to the reasonably large size of silicificated DNA origami objects, there exists a tendency to sediment. For an X-ray readout during silicification, we therefore constructed a special cell allowing for tumbling of the sample with 50 rpm around its center to ensure that the silicificated DNA origami structures remain well-dispersed in solution (see Figure 2.3 c).

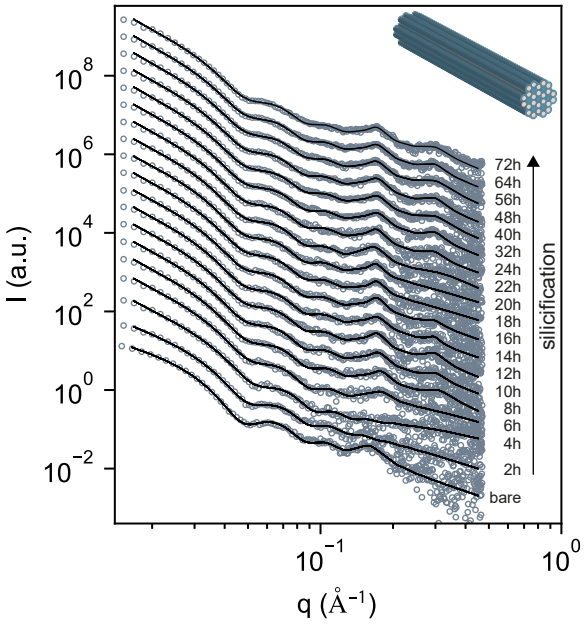

Figure 5.4.: In-situ silicification of 24-HBs monitored by SAXS. The SAXS data were recorded for bare 24-HBs and during silicification (gray circles). The SAXS data are shown together with the best fits of a cylinder model and with Lorentz peaks accounting for the inner honeycomb lattice arrangement (solid black lines). Intensities are vertically offset for clarity.

Prior to silicification, a reference measurement of the bare 24-HBs was taken. The SAXS intensity distributions of bare 24-HBs are shown in Figure 5.4 together with the SAXS intensity distributions recorded during silicification over a period of 72 h. All SAXS signals $I(q)$ exhibit three distinct oscillations with a dip at $q \approx 0.05\,\text{Å}^{-1}$, $q \approx 0.09\,\text{Å}^{-1}$, and $q \approx 0.13\,\text{Å}^{-1}$, characteristic for the cylinder shape of 24-HBs. Furthermore, all but two SAXS data sets, which were recorded in the first 4 h of silicification, show at least one sharp Lorentzian-shaped peak at $q \approx 0.16\,\text{Å}^{-1}$. This peak represents the inner DNA double helix arrangement in a honeycomb lattice of the 24-HBs, as

schematically depicted in Figure 5.2 a. Interestingly, this interhelical peak becomes more intense and distinct during the ongoing reaction and a second order peak at $q \approx 0.32\,\text{Å}^{-1}$ becomes visible after ~8 h of silicification. The described features of the SAXS data strongly indicate, that the inner order of the origami as well as the overall shape are well-preserved and that the lattice order as well as rigidity of 24-HBs increase upon silicification.

5.2.1. *The Porod invariant - a measure of silica growth*

As an initial analysis, we calculate the Porod invariant Q for each SAXS data set shown in Figure 5.4 (cf. methods in section 5.1.4). Q is a model-free measure of the total scattering contrast $\Delta\rho^2$ of the sample solution. Here, the encapsulation of rather electron-poor DNA origami objects with $\rho_{DNA} = 13 \times 10^{-6}\,\text{Å}^{-2}$ by electron-rich amorphous silica ($\rho_{SiO_2} \approx 19 \times 10^{-6}\,\text{Å}^{-2}$), yields an increasing total scattering contrast during silicification. Thus, the Porod invariant is in this experiment a measure for the silica growth on the DNA origami objects. Briefly speaking, if the silicification reaction yields a product that scatters more intensely than the solvent, Q will increase, and once the reaction stops, Q will saturate. Thus, the time to completion of the silicification reaction can also be obtained.

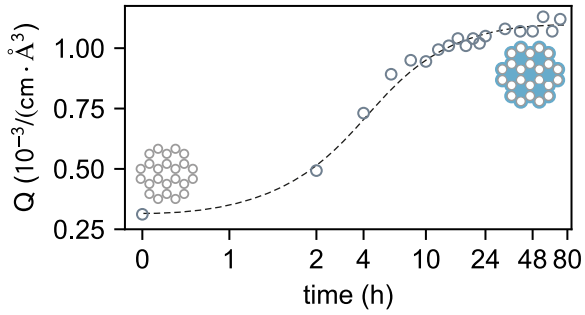

Figure 5.5.: Silica growth time dependence of the model-free Porod invariant Q obtained from SAXS data shown in Figure 5.4. Q is a measure of the overall scattering contrast, increasing in response to silicification. The data point at t=0h corresponds to the Porod invariant of bare 24-HBs. Dashed line serves as guide to the eye.

Q calculated for every SAXS data set recorded during the silicification of 24-HBs is shown in Figure 5.5. For bare 24-HBs we obtain the Porod invariant to be $Q^{24HB}_{bare}(t = 0\,h) = 0.3 \times 10^{-3}\,cm^{-1}\,\text{Å}^{-3}$. During the silicification experiment, Q increases as function of time until it reaches a plateau at $Q^{24HB}_{SiO_2} Q(t > 24\,h) = 1.1 \times 10^{-3}\,cm^{-1}\,\text{Å}^{-3}$ after ~ 24 h. This is consistent with an immediate start of silica deposition on the 24-HBs after precursor addition. Moreover, the Porod invariant analysis suggests an exhaustion of TEOS, i.e. a completed the reaction, after 24 h. The complete conversion of the silica precursors to silica is rather rapid compared to previous studies. The silica growth on e.g. 14 helix-bundles is reported to continue over several days, although the same nucleotide: TMAPS : TEOS ratio was added to the origami solution [183].

5.2.2. Silica coating of individual DNA helices

All studies on DNA origami silicification to date were lacking information on whether silica is covering exclusively the outer surface of the DNA origami object (scenario 1, Figure 5.6), or if the compositional DNA helices are also embedded in silica (scenario 2, Figure 5.6) [179, 183, 184, 186, 188].

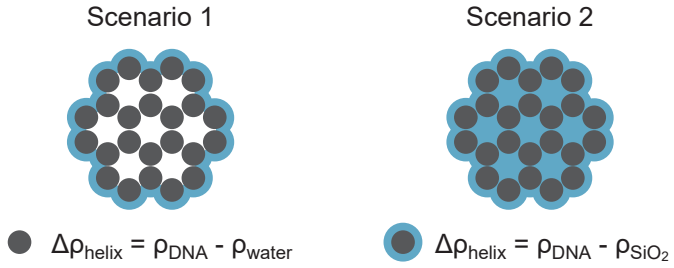

Figure 5.6.: Cartoon illustration of two different silica coating scenarios using the example of a 24-HB. Scenario 1 shows silica coating exclusively on the surface of the 24-HB. Scenario 2 depicts the silica encapsulation of all compositional helices individually.

To bring light into this question, we focus on the temporal changes of the intensity of the helix peak at $q \approx 0.16\,\text{Å}^{-1}$, which is sensitive to changes of the electron density contrast $\Delta\rho_{helix}$ between the single DNA helices and their surrounding matrix $\Delta\rho_{helix} = \rho_{DNA} - \rho_{matrix}$. As schematically depicted in the inset of Figure 5.7, ρ_{matrix} increases during silicification from $\rho_{water} = 9.4 \times 10^{-6}\,\text{Å}^{-2}$ to $\rho_{SiO_2} \approx 19 \times 10^{-6}\,\text{Å}^{-2}$. Importantly, the electron density of DNA with $\rho_{DNA} = 13 \times 10^{-6}\,\text{Å}^{-2}$ lies between those two. SAXS is not sensitive to the sign of the electron density contrast, nor in this case to its absolute values.

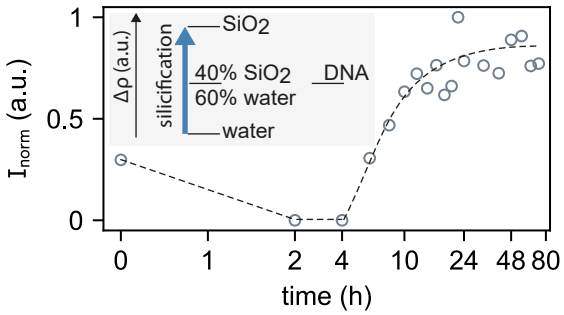

Figure 5.7.: Normalized interhelical peak intensities extracted from Figure 5.4 are shown as a function of silica growing time. The electron density of the matrix surrounding the individual DNA helices increases from $\rho_{x=water}$ to $\rho_{x=silica}$ as a result of continuous replacement of water by silica formation (inset). Contrast matching, i.e. $I_{norm} = 0$ occurs if the matrix vanishes composes of 40% SiO_2 and 60% water. The data point at t=0 h corresponds to the I_{norm} of bare 24-HBs. Dashed line serves as guide to the eye.

Nevertheless, the two scenarios depicted in Figure 5.6 can be distinguished on the basis of the interhelical peak intensity variation during the reaction. If scenario 1 holds, the interhelical peak

intensity remains constant during the silicification process. If water adjacent to the DNA surface is continuously replaced by silica formation, i.e. scenario 2 holds, contrast matching and contrast inversion will occur. The interhelical diffraction peak will vanish, if 40% of the helices are covered by silica instead of water (cf. Figure 5.7 inset and methods section 5.1.4), and later recover due to continuous silica formation.
Our results clearly reveal that the silica network frost the whole origami structure, i.e. Figure 5.6 scenario 2, holds as validated by Figure 5.7. Here, the normalized peak intensities are shown in dependence of the silica growth time and we directly observe contrast matching and contrast inversion. The normalized helix peak intensity calculated for bare 24-HBs to $I^{bare}_{norm}(t = 0\,h) = 0.3$, vanishes for two hours after precursor addition before increasing as function of silica growth time. After ~ 24 h the normalized peak intensity remains constant at $I^{SiO_2}_{norm}(t > 24\,h) = 0.8$, in accordance with the data obtained from analysis of the Porod invariant, confirming the completion of the reaction.

5.2.3. *Structural changes*

Next, the changes of the cylinder radius R and the interhelical distance a of the 24-HBs, each schematically depicted in Figure 5.2 a, are studied in response to silicification, i.e. after the addition of both silica precursors TMAPS and TEOS to the origami solution (Figure 5.8 a and Figure 5.9 a). To disentangle the effects of TMAPS and TEOS, bare 24-HBs were also exposed to TMAPS only and monitored over several hours (Figure 5.8 b and Figure 5.9 b).
To extract R and a, a cylinder model together with Lorentzian-shaped peaks accounting for the honeycomb lattice design is fitted to the SAXS intensities shown in Figure 5.4 and Figure A.2 as solid black lines. The full model is detailed in section 5.1.4.
For bare 24-HBs a cylinder radius of $R_{bare} = 80.1 \pm 0.2$ Å and an interhelical distance of $a_{bare} = 26.2 \pm 0.3$ Å was obtained. These values agree well with formerly reported results for 24-HBs dissolved in buffer with low Mg^{2+} concentration ($R_{bare} = 81.5 \pm 0.3$ Å and $a_{bare} = 26.5 \pm 0.2$ Å [7]).
The cylinder radius R in dependence of the silica growth time is shown in Figure 5.8 a. In the first four hours after precursor addition, the cylinder radius decreases in response to silicification to $R_{min}(t = 4\,h) = 74.2 \pm 0.5$ Å. Thus, we observe a so far unreported DNA origami condensation in the early stages of silicification. After condensation, the radius re-expanses as function of the silicification time until it reaches a plateau with a mean radius of $R_{SiO_2}(t > 24\,h) = 80.4 \pm 0.1$ Å.
Clearly, a determination of a silica coating thickness by a naive comparison of the radius before (R_{bare}) and after silicification (R_{SiO_2}) is not reliable. This comparison would in fact suggest, that there is no outside silica shell at all. Thus, the definition of the outer silica shell thickness needs some caution. We suggest that the difference between the cylinder radius at the end of the reaction (R_{SiO_2}) to the most condensed radius (R_{min}) is a more realistic estimate of the outer silica encapsulation thickness. Here we find $R_{SiO_2} - R_{min} = 6.2 \pm 0.3$ Å, which suggests silica encapsulation in the subnanometer regime.

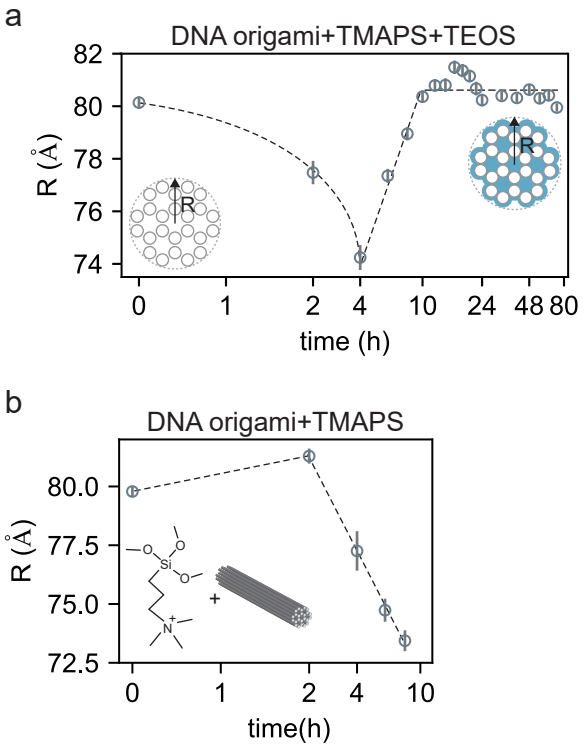

Figure 5.8.: a. Radii of the overall cylinder-shaped 24-HB structure as function of silica growth time, i.e. after the addition of TMAPS and TEOS to the origami solution. b. Radii of the 24-HB structure as function of TMAPS incubation time. Radii are obtained from model fits to the SAXS intensities shown in Figure 5.4 and Figure A.2. The points at t= 0h correspond to the radius of bare 24-HBs. Dashed lines serve as guide to the eye.

As evident from Figure 5.8 b, the cylinder radius exhibits a comparable structure condensation when bare 24-HBs are exposed to TMAPS only over several hours, but no re-expansion is observed. Importantly, the DNA condensation in response to interaction with TMAPS is not an immediate effect and only observable after 4 h. We obtain a minimal cylinder radius of $R_{min}^{TMAPS}(t = 8\,h) = 73.4 \pm 0.4\,\text{Å}$ after 8 h and thus observe that TMAPS condensates the outer 24-HB radius by $6.7 \pm 0.4\,\text{Å}$. This value agrees well with the radius condensation by $6.2 \pm 0.3\,\text{Å}$ observed during silicification (cf. Figure 5.8 a). However, the condensation in response to TMAPS only is much slower (8 h) than in response to the silicification with both precursors present (4 h). The interhelical distance a in response to silicification is evaluated to quantify inner structure changes of the 24-HB (cf. Figure 5.9 a). In the first hours after precursor addition a decreases as function of reaction time. However, a can not be determined for the first four hours of silicification, because the corresponding SAXS data sets do not exhibit any helix peaks (cf. Figure 5.4). The minimal interhelical distance is $a_{min}(t = 8\,h) = 23.8 \pm 0.2\,\text{Å}$. This value corresponds to an extremely condensed 24-HB structure, which has not even been reported at high Mg^{2+} concentrations of 11 mM [7]. After a short relaxation period, i.e. an increase in a, the interhelical spacing

reaches a mean value of $a_{SiO_2}(t > 14\,h) = 24.7 \pm 0.05\,\text{Å}$, which remains constant for the ongoing experiment. The honeycomb lattice design of 24-HBs@SiO_2 stays intact during the silicification, although it is substantially more condensed than the bare lattice arrangement.
Next, the effect of TMAPS on the interhelical distance is studied as function of time (Figure 5.9 b). Similar to the cylinder radius, the interhelical distance is substantially condensed after a few hours of TMAPS exposure and no re-expansion is observed. We obtain a minimal interhelical distance of $a_{min}^{TMAPS}(t = 8\,h) = 25.2 \pm 0.3\,\text{Å}$ and thus observe TMAPS-induced condensation of the interhelical distance by $1.0 \pm 0.3\,\text{Å}$.

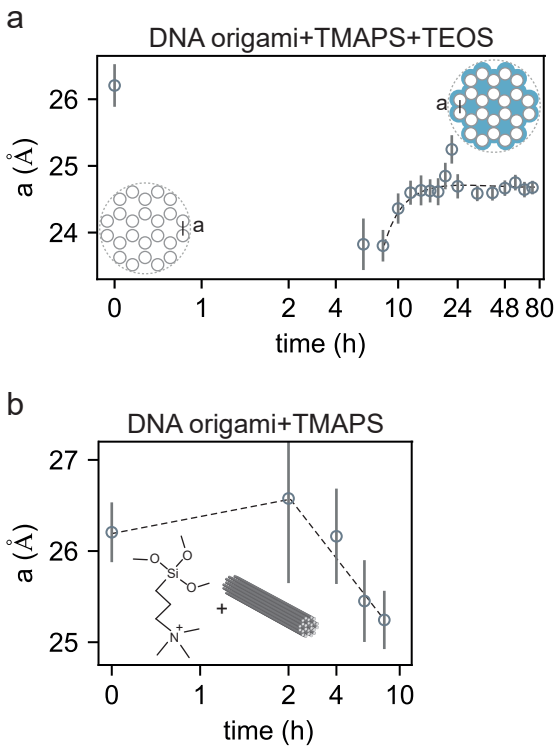

Figure 5.9.: a. Interhelical distances of the overall cylinder-shaped 24-HB structure as function of silica growth time, i.e. after the addition of TMAPS and TEOS to the origami solution. b. Interhelical distances of the 24-HB structure as function of TMAPS incubation time. Interhelical distances are obtained from model fits to the SAXS intensities shown in Figure 5.4 and Figure A.2. The data points at t=0h correspond to the interhelical distances of bare 24-HBs. Dashed lines serve as guide to the eye.

These results strongly indicate that silicification is preceded by TMAPS related condensation, whereas the formation of a silica network on and within the DNA origami objects are responsible for structure re-expansion.

5.2.4. *Thermal stability*

From previous reports, the thermal stability of silicificated DNA origami objects up to 1200°C has been convincingly demonstrated [183,184,200]. Here, increased thermal stability for 24-HBs@SiO_2 with an ultrathin outer silica coating (6.2 ± 0.3 Å) is shown by heating the sample solution after the in-situ SAXS experiment to 60°C for 30 min and subsequent TEM analysis (cf. Figure A.3). However, so far it remains unclear, if only an outer silica shell provides increased origami stability, or if the silica penetration into the structure provides sufficient stabilization. Here, we answer this question by heating maximal condensed 24-HBs@SiO_2 with a cylinder radius of $R = 74.5 \pm 0.4$ Å ($R_{min} = 74.2 \pm 0.5$ Å) to 60°C for 30 min and subsequent SAXS analysis. Bare 24-HBs completely dissolve at this temperature (Figure 5.10 a), whereas the silicificated structures remain, despite the lack of a measurable outer silica shell ($R - R_{min} \approx 0$ Å), stable (Figure 5.10 b). In the light of these findings, the outer silica shell thickness is not the main indicator for increased stability, but rather the silica penetration into the structure and its ability to stabilize it from the inside.

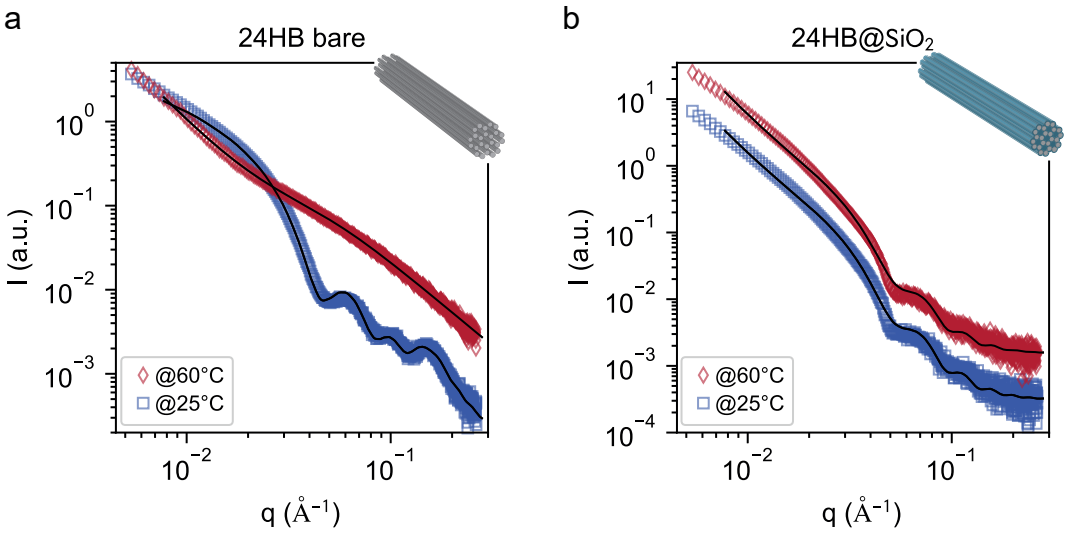

Figure 5.10.: a. SAXS intensities of bare 24-HBs measured at room temperature (blue squares) and after heating the structures to 60° for 30 min (red diamonds). b. SAXS intensities of 24-HBs@SiO_2 measured at room temperature (blue squares) and after heating the structures to 60° for 30 min (red diamonds).

Importantly, the SAXS data of maximal condensed 24-HBs@SiO_2 do not exhibit any interhelical distance peaks (cf. Figure 5.10b) and are therefore expected to be in the contrast matching phase. These findings suggest increased thermal stability of 24-HBs@SiO_2 frosted by a 40 % silica and 60 % water mixture.

5.3. Silicification of cuboid-shaped DNA origami objects with different lattice designs

Next, the role of DNA origami shape and its inner lattice design for the structural changes induced by silica encapsulation are investigated. To provide insights on the effect of the DNA origami shape, the silicification of a cuboid-shaped 4-LB with the same honeycomb lattice design as the 24-HBs (see Figure 5.2 b) was monitored by SAXS. The 4-LB was newly designed by the Heuer-Jungemann group. To gain information on the effect of different inner lattice designs, we performed a third SAXS experiment monitoring the silicification of cuboid-shaped 3-LB with a square lattice design (see Figure 5.2 c).
The silica formation on both cuboid-shaped origamis was, as for 24-HBs, initiated by the addition of TMAPS and TEOS with a ratio of 1 nucleotide: 5 TMAPS : 12.5 TEOS to the origami solution and the reaction solution was gently tumbled during the measurement. See section 5.1.1, 5.1.2 and 5.1.3 for details on origami preparation, silica coating and experimental details.

5.3.1. *Silicification of four layer blocs*

The SAXS intensities for bare 4-LBs are shown in Figure 5.11 together with the SAXS data recorded during silicification. All SAXS signals $I(q)$ exhibit one to two distinct oscillations with a dip at $q \approx 0.07\,\text{Å}^{-1}$ and $q \approx 0.13\,\text{Å}^{-1}$ characteristic for the cuboid shape of 4-LBs.

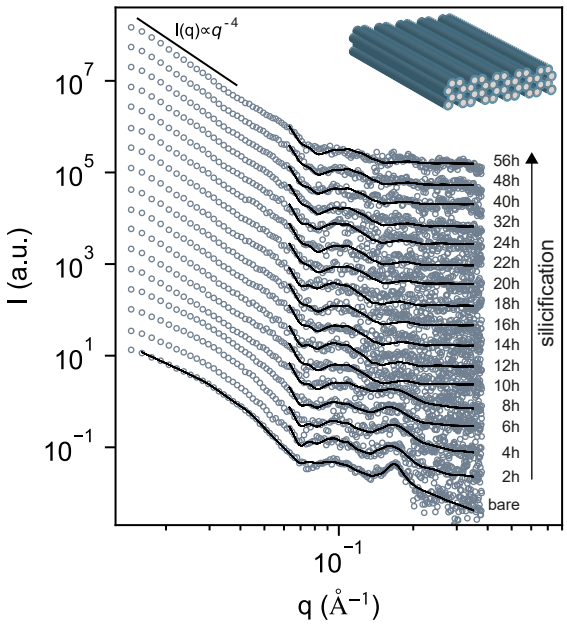

Figure 5.11.: In-situ silicification of 4-LBs monitored by SAXS. SAXS data are recorded for bare 4-LBs and during silicification (gray circles). The SAXS data are shown together with the best fits of a cuboid model and Lorentz peaks accounting for the honeycomb lattice arrangement (solid black lines). Intensities are vertically offset for clarity.

For bare 4-LBs a particular strong Lorentzian-shaped peak can be observed at $q \approx 0.17\,\text{Å}^{-1}$. This indicates a well-ordered honeycomb lattice arrangement as schematically depicted in Figure 5.2b. However, the peak disappears after $\sim$10 h.

In contrast to the 24-HBs@SiO_2, the SAXS data recorded during the silicification of the 4-LBs show evidence of aggregation, i.e. a power law like upturn of the SAXS intensity towards small q-values rather than an intensity plateau. Thus, the achievement of well-dispersed 4-LBs@SiO_2 seems to be limited.

A cuboid model together with Lorentzian peaks accounting for the inner honeycomb lattice design is fitted to the SAXS intensities to study the overall 4-LB shape and its inner helix arrangement (Figure 5.11, solid black lines). The q-range dominated by aggregation is excluded from model fitting. The full model is detailed in section 5.1.4.

For bare 4-LBs the following cuboid dimension are obtained for the first time: $A_{bare} = 89.9 \pm 0.4\,\text{Å}$, $B_{bare} = 379 \pm 5\,\text{Å}$ and $C_{bare} = 555 \pm 14\,\text{Å}$. The cuboid length C and width B are too large to be reliable resolved by a laboratory SAXS experiment and serve just as rough estimates. On the contrary, the value of the cuboid height A can be determined with subnanometer precision. The here obtained value for A exceeds the design value substantially (cf. Table 5.1), which is likely to be a consequence of the low Mg^{2+} concentration (3 mM) in the buffer. Also, the oversimplified model used to calculate these design values, which ignores e.g. the well-known chicken-wire like structure of the DNA helices within the origami [7, 162], may underestimate the 4-LBs' dimensions.

Furthermore, we observe an interhelical DNA helix spacing of $a_{bare}^{4-LB} = 25.0 \pm 0.2\,\text{Å}$ for the bare 4-LB by fitting a Lorentzian-shaped peak centered at $q_0 = 2\pi/a$ in addition to the cuboid model. This value is smaller compared to the lattice parameter of a 24-HB measured under similar buffer and temperature conditions ($a_{bare}^{24HB} = 26.2 \pm 0.3\,\text{Å}$). Thus, the 4-LBs' inner honeycomb helices are more densely packed than that of 24-HBs.

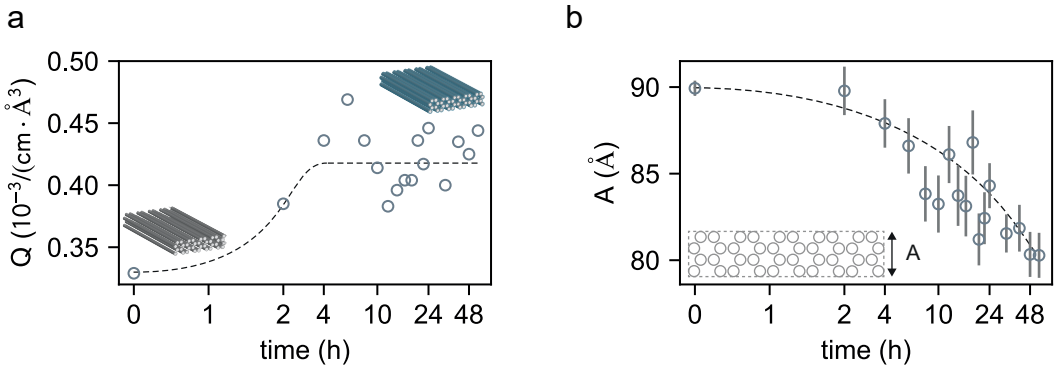

Figure 5.12.: a. Silica growth time dependence of the model-free Porod invariant Q(t) obtained from SAXS data shown in Figure 5.11. b. Heights A(t) of the cuboid-shaped 4-LB as function of silica growth time. The data points at t=0 h correspond to bare 4-LBs. Dashed lines serve as guide to the eye.

Again, the Porod invariant Q is calculated for each SAXS data set (cf. section 5.1.4) and shown in Figure 5.12 a. The Porod invariant of bare 4-LBs $Q_{bare}^{4-LB}(t = 0\,h) = 0.3 \times 10^{-3}\,cm^{-1}\,\text{Å}^{-3}$ is similar to the value of bare 24-HBs. Also, Q increases as function of silica growth time. However, the plateau $Q_{SiO_2}^{4-LB}(t > 4\,h) = 0.42 \times 10^{-3}\,cm^{-1}\,\text{Å}^{-3}$, indicative of completed silica growth, is reached rapidly after ~ 4 h, i.e. much earlier than for 24-HBs@SiO_2. Furthermore, the increase of the Porod invariant is much lower than for 24-HBs@SiO_2, indicative of a low but still detectable amount of silica deposition on the 4-LBs.

Next, the changes in height A of the cuboid-shaped 4-LB (cf. inset of Figure 5.12 b) in response to silicification were studied. In response to silicification the 4-LB height decreases steadily as function of silica growth time (see Figure 5.12 b). After 56h a minimal height of $A_{min}(t = 56\,h) = 80.3 \pm 1.3$ Å is obtained. Comparison with the bare 4-LB height reveals a condensation by $A_{bare} - A_{min} = 9.6 \pm 0.7$ Å. However, this time the silica growth does not reverse the condensation, although the Porod invariant clearly indicates that some silica is incorporated in the 4-LBs.

The lack of re-expansion and the low increase of the Porod invariant in response to silicification are consistent with the vanishing interhelical peak in the SAXS data after $\sim$ 10 h (Figure 5.11). The peak vanished presumably due to uptake of silica and does not recover, implying that the amount of silica formation on the 4-LB helices are insufficient to overcome the contrast matching condition (cf. section 5.2.2).

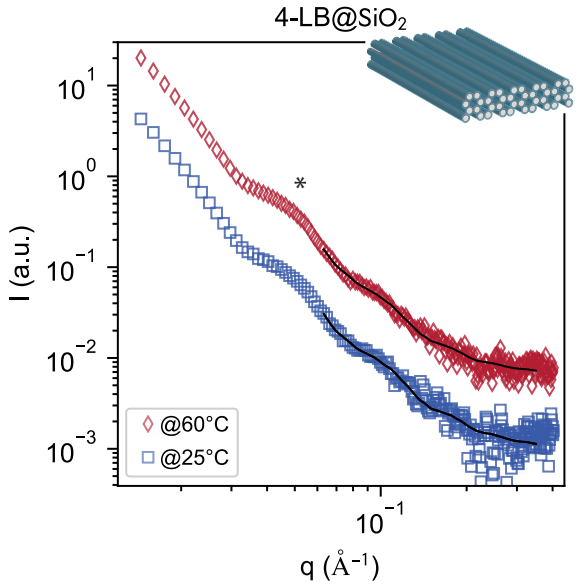

Figure 5.13.: SAXS intensities of 4-LBs@SiO_2 measured at room temperature (blue squares) and after heating the structures to 60° for 30 min (red diamonds). The 4-LB@SiO_2 stacking peak visible in the low q-regime is highlighted (*).

Unfortunately, low amount of silica deposition does not per se prevent aggregation. It is known that aggregation as well as silica agglomeration are highly influenced by concentration, movement,

pH and temperature [183]. To check if the observed aggregation for 4-LBs during silicification can be reduced, we performed SAXS measurements on a second batch of 4-LBs@SiO_2. Therefore, the origami concentration was reduced by a factor of ten and instead of gentle tumbling, the reaction solution was kept at rest for three days (cf section 5.1.2). This silicification protocol yielded 4-LBs@SiO_2 with a cuboid height of 86.2 ± 1.7 Å, i.e. an outer silica shell thickness of 5.9 ± 1.5 Å.

The corresponding SAXS data of this 4-LB@SiO_2 recorded at 25 °C (Figure 5.13, blue squares), however, still exhibit clear signs of particle aggregation, i.e. an upturn of SAXS intensity at small q-values. Moreover, the data show a broad peak centered at $q \approx 0.05\,\text{Å}^{-1}$. In this low q-regime, SAXS probes repeated interparticle distances and such pronounced peaks arise from stacking of single particles into larger assemblies [201]. From the peak position, a center-to-center interparticle distance of 137 ± 3 Å is calculated and particle aggregation further confirmed by an intraparticle stacking peak.

Nevertheless, in agreement with previous reports [183, 184], thermal stability of 4-LBs surrounded by a subnanometer thick silica shell after heating to 60 °C for 30 min (red diamonds) could be confirmed (cf. Figure 5.13).

5.3.2. *Silicification of three layer blocs*

In the following section the results from in-situ SAXS experiments monitoring the silicification of cuboid-shaped 3-LBs with a squared lattice design are summarized. By comparison of the structural changes during silicification of two cuboid-shaped DNA origami objects with different inner lattice arrangements, i.e. 4-LBs and 3-LBs, we aimed to probe the influence of the inner lattice design on DNA origami silicification.

The SAXS intensities of bare 3-LBs are shown in Figure 5.14 together with the SAXS data recorded during the silicification. The SAXS data of bare 3-LBs exhibit two defined oscillations with a dip at $q \approx 0.08\,\text{Å}^{-1}$ and a distinct peak at $q \approx 0.22\,\text{Å}^{-1}$ characteristic for the cuboid shape of 3-LBs. During the silicification process, the cuboid oscillations and the lattice peak become rapidly invisible. In fact, the SAXS intensities recorded during the silicification are quickly dominated by two power-laws as highlighted in Figure 5.14. This is consistent with the formation of fractal aggregates, i.e. extreme aggregation, which are characterized by the presence of two power-laws at low and high q-values, respectively [202]. Here, $I(q) \propto q^{-3}$ at low q-values corresponds to the scattering from the aggregates, whereas the scattering of the particle surface manifests itself as $I(q) \propto q^{-2}$ at high q-values.

Due to the fractal formation, the SAXS data remain inconclusive, about how well the overall shape, e.g. the cuboids' aspect ratio, and the inner lattice design are preserved during silicification.

However, the Porod invariant Q and the cuboid height A can still be studied. To extract A, the surface scattering is taken into account and the q-range for model fitting limited to a form-factor dominated region ($0.035 < q < 0.35\,\text{Å}^{-1}$) (see section 5.1.4 for details).

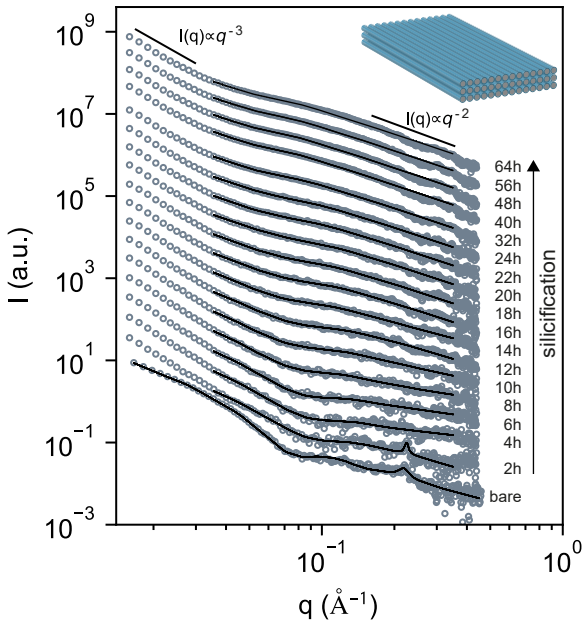

Figure 5.14.: In-situ silicification of 3-LBs monitored by SAXS. SAXS data are recorded for bare 3-LBs and during silicification (gray circles). The SAXS data are shown together with the best fits of a cuboid model and Lorentz peaks accounting for their squared lattice design (solid black lines). Intensities are vertically offset for clarity.

The 3-LBs' Porod invariant as function of silica growth time is shown in Figure 5.15 a. The Porod invariant calculated for the bare 3-LBs $Q_{bare}^{3-LB}(t = 0\,h) = 0.35 \times 10^{-3}\,cm^{-1}\,\text{Å}^{-3}$ is in good agreement with values obtained for bare 24-HBs and 4-LBs. Here, Q increases quickly after the precursor addition and reaches a plateau at $Q_{SiO_2}^{3-LB}(t > 48\,h) = 2.2 \times 10^{-3}\,cm^{-1}\,\text{Å}^{-3}$ only after $\sim$ 48 h. Thus, the 3-LB silica growth last substantially longer and the increase of the Porod invariant is much larger than the 24-HB's and the 4-LB's as summarized in Table 5.3. This is indicative of a larger amount of silica deposition on the 3-LBs helices compared to the two other investigated DNA origami objects.

	24-HB@SiO_2	4-LB@SiO_2	3-LB@SiO_2
Q_{SiO_2}(t) in $(cm^{-1} \cdot \text{Å}^{-3})$	1.1×10^{-3} (24 h)	0.42×10^{-3} (4 h)	2.2×10^{-3} (48 h)

Table 5.3.: Porod invariants of 24-HB@SiO_2, 4-LB@SiO_2, and 3-LB@SiO_2. The time required to reach a constant Porod invariant, i.e. to complete the DNA origamis' silicification, is given in brackets.

A cuboid model (cf. section 5.1.4) is fitted to the SAXS data and shown as solid black lines in Figure 5.14 to determine the 3-LB height A as function of silica growth time. For the bare 3-LBs an interhelical distance can be calculated, too. We find $A_{bare}^{3-LB} = 80.0 \pm 0.4$ Å and $a_{bare}^{3-LB} = 28.8 \pm 0.3$ Å to be somewhat larger than formerly reported values for the same DNA origami object ($A_{bare}^{3-LB} = 76.6 \pm 0.2$ Å and $a_{bare}^{3-LB} = 27.32 \pm 0.02$ Å [7]).

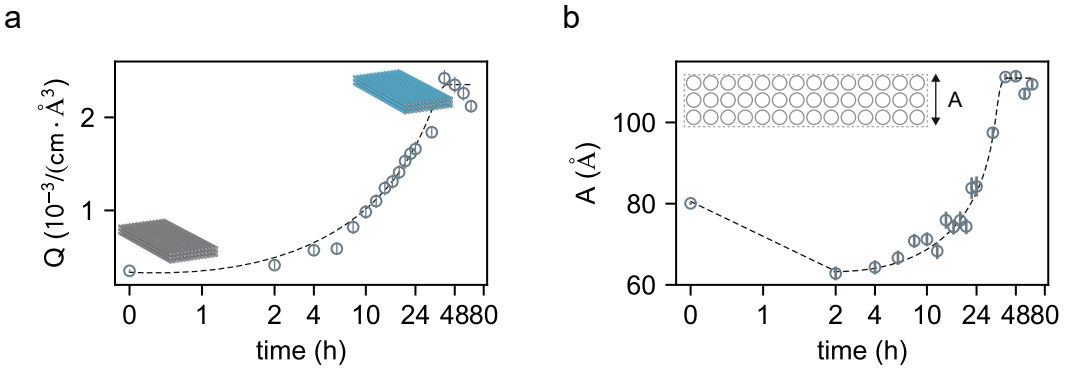

Figure 5.15.: a. Silica growth time dependence of the model-free Porod invariant Q(t) obtained from Figure 5.14. b. Heights of the overall cuboid-shaped 3-LB as function of silica growth time. The data points at t=0 h correspond to bare 3-LBs. Dashed lines serve as guide to the eye.

Figure 5.15 b gives the cuboid height A, which is schematically depicted in the inset, in dependence of the silica growth time. In agreement with previous silicification experiments, the 3-LB height undergoes significant condensation in the beginning of the reaction. We obtain a minimal value of the cuboid height after ~ 2 h with $A_{min}^{3-LB}(t = 2h) = 62.8 \pm 1.7$ Å, i.e the 3-LBs are condensed by 17.2 ± 1.8 Å. Again, we observe a comparable condensation in response to the interaction with TMAPS-only. The corresponding SAXS data and the extracted cuboid heights are shown in Figure A.4). After condensation, we observe an expansion of A exceeding the bare origamis' cuboid height by far. After 48 h the mean cuboid height calculates to $A_{SiO_2}^{3-LB} = 109.7 \pm 0.7$ Å. The outer silica encapsulation for 3-LBs is estimated to be $A_{SiO2}^{3-LB} - A_{min}^{3-LB} = 47 \pm 1$ Å thick.

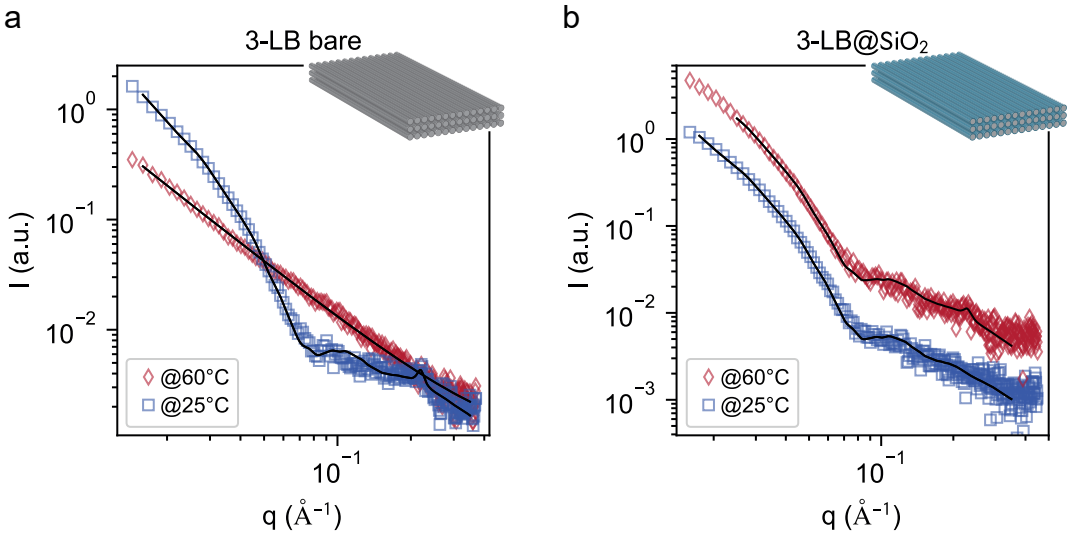

Figure 5.16.: a. SAXS intensities of bare 3-LBs measured at room temperature (blue squares) and after heating the structures to 60°C for 30 min (red diamonds). b. SAXS intensities of 3-LBs@SiO_2 measured at room temperature (blue squares) and after heating the structures to 60°C for 30 min (red diamonds).

This extreme value is in line with the Porod invariant analysis and strongly suggest a large amount of silica deposition on the 3-LBs during the in-situ SAXS measurement. Such thick silica encapsulation is likely to favour aggregation and fractal formation as observed for 3-LBs@SiO_2 (cf. Figure 5.14).
This time, the aggregation of 3-LBs during silicification was successfully reduced by using a silicification protocol for which the origami concentration was reduced by a factor of ten and the reaction solution was kept at rest for three days (cf section 5.1.2). This silicification protocol yielded well-dispersed, non-deformed and thermally stable 3-LBs@SiO_2 with a cuboid height of 77.0 ± 0.4 Å, i.e. an outer silica shell thickness of 14.2 ± 1.2 Å (cf. Figure 5.16).

5.4. Conclusion and discussion

In the following, the previously described results from monitoring the silicification of 24-HBs by SAXS are briefly summarized and combined into one picture. Figure 5.17 shows a cartoon illustration of the 24-HB silicification, derived from studying the Porod invariant, the helix peak intensity, the overall cylinder radius, and the interhelical lattice distance as function of silica growth time.

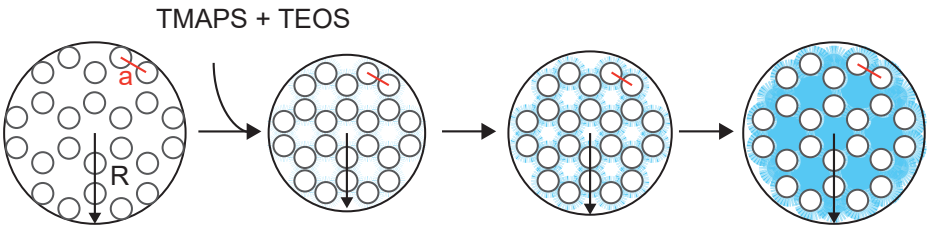

Figure 5.17.: Cartoon illustration of 24-HB silicification.

As the Porod invariant increases steadily as function of silica growth time, we conclude that the silica growth starts immediately after the addition of the second silica precursor TEOS to the reaction solution. It continues until all precursor material is converted into silica or the reaction is interrupted. Higher quantities of precursor will lead to more silica deposition on the 24-HB helices and yield larger cylinder radii for 24-HB@SiO_2. However, to much precursor material will lead to particle aggregation, surface roughness and shape deformation as illustrated in Figure 5.18 and observed for cuboid-shaped origami@SiO_2.
The process of DNA origami silicification is known to be sensitive to movement of the reaction solution [183]. Despite equal precursor ratios, the time required for completed silicification varies greatly depending on whether the reaction solution is held at rest or tumbled. A possible explanation for the in averagely speed up reaction while gentle tumbling might not only be a better mixing of the solution, but also the provided kinetic energy.

The time dependent analysis of the first interhelical peak intensities clearly reveals a silica frosting of the whole origami structure rather than of silica growth in a shell-like fashion on the outer 24-HB surface.
The structural changes of the 24-HB seem to be driven from two contrary mechanisms. During silicification, first, a condensation the cylinder radius as well as the interhelical spacing is observed. This condensation is likely to be driven by firstly, the positively net-charged TMAPS, whose binding to the DNA nucleotides causes electrostatic screening of the repulsion of parallel double helices [7, 191, 203, 204], possibly in conjunction with osmotic effects. As we observe the condensation to be twice as fast under the presence of both precursors, we further speculate that early silica formation entails a hydrophobic effect, which accelerates condensation. The initial reaction lag of TMAPS only induced condensation further suggests that the access of TMAPS to the nucleotide groups by diffusion is obstructed.
The second mechanism is an relaxation and expansion of the 24-HBs' structure due to continuous silica formation on and within the origami objects. Here, the silica growth on the 24-HBs compensates exactly the origami condensation due to the presence of TMAPS. This way, an outer subnanometer thin silica shell is achieved.
However, by experiments studying the thermal stability of extremely condensed 24-HBs@SiO_2, we find that the outer silica shell thickness is not the main indicator for increased stability, but rather the silica penetration into structure and thus its ability to stabilize it from the inside. From X-ray contrast matching conditions, we infer that 40% of water-by-silica replacement within the DNA origami is sufficient to provide stability at physiological relevant conditions.
As a net effect, the overall cylinder-shape as well as the inner honeycomb lattice design of the 24-HB@SiO_2 are well preserved. The appearance of a second interhelical peak as observed for 24-HBs@SiO_2 is a strong hint for lattice rigidification in response to silicification.

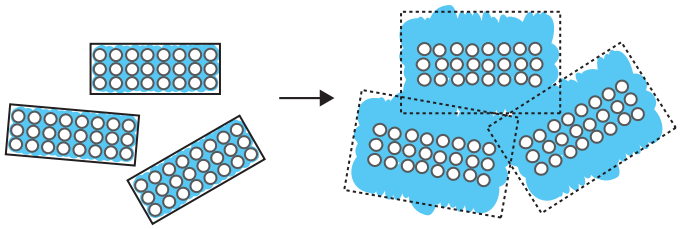

Figure 5.18.: Cartoon illustration of silica 'overgrowth' by the example of 3-LB silicification.

The comparison of the silicification of the cylinder-shaped 24-HBs and the cuboid-shaped 4-LBs, which are both based on a honeycomb lattice design, reveals the following similarities: Firstly, silicification yields a promptly increasing scattering contrast for both in-situ SAXS experiments in response to silica growth; Secondly, silicification for both DNA origami objects provides an increased thermal stability and a well preserved shape; Thirdly, both structures undergo substantial

changes of the shape dimensions and show a large condensation of either the cylinder radius or the cuboid height in response to silicification. However unlike 24-HBs, 4-LBs exhibit no re-expansion of cuboid height during the silicification process. This observation is in line with a vanishing interhelical peak and a smaller increase of the 4-LBs' Porod invariant. These three observations suggest a rather small amount of silica growth on the 4-LBs, despite an equal nucleotide: TMAPS : TEOS ratio for both experiments. Furthermore, the SAXS data of 4-LB@SiO_2 exhibit evidence of irreversible particle aggregation and stacking during the silica growth process.

The silicification comparison of honeycomb lattice based 4-LBs with the squared lattice based 3-LBs, both exhibiting on cuboid shape, reveals the following similarities: Firstly, a promptly increasing scattering contrast during the in-situ SAXS measurement; Secondly, an increased thermal stability; Thirdly, a retained overall shape during the silicification, if a less aggregation inducing silicification procedure is chosen; Although varying in characteristics, e.g. inter particle stacking vs. fractal aggregates, both cuboid DNA origamis exhibit, fourthly, a tendency towards aggregation during silica growth; And lastly, both origami objects undergo a large condensation of the cuboid height in response to silicification. However, we observe much more silica growth and, thus, a large expansion of the cuboid height for the 3-LBs than for 4-LBs or 24-HBs.

Unfortunately, the question to which extend the silicification process is altered by different inner lattice designs, could not be fully answered, but we observe that DNA origami with flat surfaces show increased tendency towards aggregation during silicification.

The interhelical lattice peak vanished for both cuboid-shaped DNA origami objects during silica growth. However, it is reasonable to assume that this a result of a diminished scattering contrast for the extremely thin silica coated 4-LBs (see section 5.3.1), this is unlikely the case for the thick silica encapsulation as observed on the 3-LBs. So far, the 3-LB data remain inconclusive, whether this is result of an increased lattice disorder, or if the scattering signal is overshadowed by the surface scattering of the 3-LB aggregates.

The large differences in the amount of silica formation on DNA origami objects and, consequently, in the thickness of the outer silica encapsulation are unexpected and seem to be too drastic to be only caused by varying DNA origami shapes or inner lattice arrangement. It is likely that this variation is caused by a well-known problem: inaccurate volume delivery due to high vapor pressure. This plays a role when transferring $0.5 - 3\mu l$ of precursor-methanol mixtures into the origami solution to initiate silicification. This way, the nucleotide: TMAPS : TEOS ratio, which was intended to be equal for every conducted experiment, could be altered. It seems that even tiny deviations from this ratio have large effects on the the amount of silica deposition on DNA origami helices. Thus, we identify the precursor ratio as a crucial parameter to achieve conformal and reliable silica growth. However, this is just a minor technical problem on the way to subnanometer fine-control of DNA origami templated silica growth and will soon be resolved.

6. CONCLUSION AND OUTLOOK

Within this thesis, SAXS was used to investigate three different artificial biomolecular constructs, which are capable of a biomimetic or novel function and thus called 'nanoagents': DNA coated gold-silver core-shell nanorods, photoswitchable lipid membranes and silica-coated DNA origami objects. In order to realize some of these experiments, the role of the X-ray beam energy in solution-based SAXS experiments had to be evaluated. As the optimal sample thickness increases with increasing beam energy, high-energy SAXS experiments ($\geq$17.4 keV) exhibit a spacious sample environment and therefore provide the possibility for the installation of complex sample environments involving temperature control, light illumination or tumbling. Moreover, it is important, that the deposited X-ray dose decreases drastically with increasing beam energy in the range of 5-36 keV. This emphasizes the role of higher X-ray energies as low-dose probes in radiation-sensitive soft matter experiments.

First, the structure of DNA-coated gold-silver nanorods for plasmonic applications was studied by SAXS and WAXS experiments. By covering an exceptional broad q-range for the SAXS measurements, the synthesis design of the plasmonic nanorods was validated with subnanometer precision. Furthermore, we confirmed mostly monodisperse nanorods with a gold core, an intact silver shell crucial for improved plasmonic properties and a homogeneous DNA-shell important for the nanorods' chemical addressability and bio-compatibility. Additional, WAXS experiments revealed a fcc crystal structure and mono-crystallinity of the particles.

Second, the switching of photoresponsive lipid membranes, which are assembled from a synthetic lipid with a light-responsive azobenzene group in one of its two hydrophobic tails (azo-PC), is analyzed. Azo-PC can be reversibly isomerised between *trans* and *cis* state upon UV or blue light illumination, respectively. In azo-PC membranes the light-driven molecular switching translates to a precise and reversible optical control of many membrane properties. Here, SAXS was used to demonstrate photo-stimulated membrane thickness changes of ca. 4 Å for ca. 42 Å azo-PC membranes and ca. 1.5 Å for ca. 33 Å red-azo-PC membranes. Red-azo-PC is a second photolipid, which harbors a tetra-ortho-chlorinated azobenzene instead of azobenzene group in its tail and undergoes isomerization with tissue penetrating red light. To realize SAXS experiments on photoswitchable membranes with defined illumination conditions, a dual LED light pump X-ray probe setup was built. Though the macroscopic photo-responses of azo-PC membranes, i.e. thickness variations, are clear, it is unclear how large the changes of *trans*/*cis* ratio are, and if they can be improved. This partly derives from the technical challenge to measure a *trans*/*cis* ratio in ordered anisotropic, highly concentrated assemblies instead of molecular solutions. In this work, the SAXS measured membrane thicknesses were related to *trans*/*cis* ratios within the azo-PC mem-

brane. This revealed an unexpected sensitivity of the photoswitches inside the lipid membranes to the aqueous buffer conditions, particularly with a smaller-than-expected photoswitching yield under low ionic strength. By mixing pre-switched azo-PCs, a membrane thickness control of 8 Å is demonstrated to be experimentally possible if the photoswitching efficiency is unimpeded. This is twice as large as the thickness variation achieved by purely optical means and much larger than the membrane thickness variation achievable by temperature variations with conventional lipids. The correlation of SAXS measured membrane thickness to *trans*/*cis* ratios also revealed soft X-rays (8 keV) to efficiently, rapidly, and quantitatively isomerize photolipid membranes to the all-*trans* state, which was attributed to a process called catalytic switching, i.e. racial redox reactions following X-ray dose deposition in the medium. This enables soft X-rays, as an example for a redox reaction trigger, to enforce a higher degree of membrane property control than by optical means. Also, this confirms a high X-ray dose deposition of soft X-rays in solution-based samples.
Third, we aimed to analyze the impact of the encapsulation of DNA origami objects in a protective silica shell by sol-gel chemistry on the overall origami shape and its inner fine structure. Therefore, the silica growth on a prototypic DNA origami object was monitored in-situ by SAXS over several days. A newly designed sample holder, which tumbled the reaction solution with constant speed around the beam axis, prevented sedimentation during the experiment. A so far unreported substantial condensation of the DNA origami objects induced by one of two silica precursors (TMAPS), probably in conjunction with hydrophobic effects during the early stages of silicification were observed. Subsequently, the DNA origami objects re-expanse in response to silica deposition on the origami helices. By X-ray contrast matching we demonstrate, that silica formation occurs on the inside and the outside of DNA origami, thereby frosting the whole structure in silica. As a net effect, silicification preserves the overall shape and the inner fine structure in great detail and increases the inner lattice order. By experiments studying the thermal stability of 24-HBs@SiO_2, we find that the outer silica shell thickness is not the main indicator for increased stability, but rather the silica penetration into structure and thus its ability to stabilize it from the inside. Comparison with silicification of two more differently shaped DNA origami objects reveal a tendency towards aggregation during silicification for DNA structures with flat surfaces, i.e. cuboid-shaped objects, and highlight the importance of the precursor ratio control in the reaction mixture to achieve conformal silica growth.

SAXS with high-energy X-rays ($\geq$ 17.4keV) provides an undisturbed readout of the photoswitchable membrane thickness, which has been demonstrated to linearly correlate to the photolipid's isomerization fraction. In the future, this correlation can be used to obtain *trans*/*cis* ratios of newly designed photolipid membranes and quantify their operating range under different conditions. This way, photolipids with new properties such as extended optical ranges can be optimized and evaluated for the use in artificial membranes.
For azo-PC membranes, we proved efficient photoswitching in physiological stabilized environ-

ments, i.e. in buffered solutions. This is encouraging for future experiments involving living cells. This might be further relevant for red-azo-PC, which undergoes photoisomerization on irradiation with tissue penetrating red light. It might be beneficial to explore the *trans*/*cis* ratios which drive the red-azo-PC membrane's structure changes and to investigate whether their rather small photo-induced thickness control in DI water can be improved when dissolved in aqueous solution with higher ionic strength.

The 8 Å thickness change accessible to photolipid membranes under photoswitching in buffered systems (20 % of membrane thickness) is massive, and far beyond the effects achievable by temperature or temperature jumps in conventional lipids. This huge membrane thickness change may benefit from ordering effects in the *trans* state related to H-aggregate formation as observed in spectroscopic studies. H-aggregates can be subjected to melting upon higher temperatures, which in turn should be observable by a thinning of the membrane thickness. Thus, it would be fruitful to check the presence of H-aggregates by SAXS measurements of all-*trans* azo-PC membranes at elevated temperatures.

Furthermore, soft X-rays (8 keV) have been demonstrated to induce reversible quantitative *cis*-to-*trans* switching in azo-PC membranes via suitable redox chemistry reactions, which has not been realized before. Thus, the structural response of azo-PC membranes in DI water could be greatly enlarged. Furthermore, this is a rare example of reversible quantitative switching in optically dense systems, which may encourage other researches to exploit redox reactions to optimize the operating range of existing and newly designed photoresponsive materials. Such redox reactions do not necessarily have to be triggered by X-rays but may also be achieved with cleverly chosen dye sensitizers or redox conditions.

For higher X-ray energies such as 17.4 keV and 54 keV, no redox chemistry induced backswitching of azobenzene lipid membranes was observed. In fact, the deposited X-ray dose applied to SAXS samples with high water fraction displays a minimum at 36keV. Importantly, such high X-ray beam energies provide still high quality SAXS data as theoretical calculated and experimentally proven in this thesis. Thus, this work suggests a favorable energy regime of 30-42 keV for SAXS experiments on radiation damage sensitive samples and provides an alternative approach to minimize the deposited X-ray dose in a sample. Hopefully, this guideline will help future X-ray scientists to perform high-energy SAXS experiments and exploit its potential to reduce radiation damage to biological samples.

Due to the rapid development of high power LEDs, and the availability of pulsed lasers at synchrotron sources it is to be expected that future SAXS experiments with pulsed illumination on photoswitchable membranes may allow structure transition times of few ms and below. Light-pump and X-ray probe experiments on such short time scales would be particularly suited to explore the kinetics of switching in photolipid multilayers. Those diffraction patterns consist of intense and defined Bragg peaks allowing for a robust readout of the lamellar repeating distance, which is composed of the thickness of the intercalated water layer and the photolipid membrane

thickness. On such short time scales, the hydrodynamic coupling of the intercalated water to the photolipid membrane may be studied and interesting transient phenomena such as pore formation might be observed. Furthermore, the determination the bending rigidity as a complementary biophysical membrane property would be accessible by SAXS experiments on photolipid multilayers via the Caillé theory.

Monitoring the silicification of prototypic DNA origami objects by SAXS revealed so far unreported condensation of the DNA origami shape and its inner fine structure, prior to their expansion in response to silica deposition on the origami helices. This experiment contributed to gain a profound understanding of the silicification process and may help to establish a silica growth protocol that retains the overall origami shape with high precision. Monitoring the silica growth on large DNA crystals might be equally helpful for finding the balance between silica growth required to stabilize the structures and structure congesting overgrowth. Furthermore, the lattice constants of silicificated DNA crystals are likely to be influenced by the silicification process, too. Their investigation in response to silica growth may be crucial for implementing their envisioned application as photonic crystals.

Comparison of different DNA origami silicification experiments revealed a tendency towards aggregation during silicification for origami objects with flat surfaces. These experiments furthermore identified the precursor ratio as crucial parameter to achieve conformal and reliable silica formation and a final outer encapsulation thickness on the nanometer scale. These control might be improved in the future by addressing a well-known technical challenge: The high vapor pressure of methanol often results in inaccurate volume delivery when transferring small solutions volumes, such as $0.5 - 3\,\mu l$ of precursor-methanol mixtures. This way, the precise control of the precursor ratios, which in turn is crucial to fine tune the silica growth on DNA origamis might be impeded. However, with these results in mind and the technology for monitoring silica growth closely, this technical challenge can soon be resolved.

Some aspects of the DNA origami silicification, such as the sensitivity of the reaction solution to movement or the occasional formation of pure silica spheres besides the DNA origami templated silica growth are to date not fully understood. The synthesis of monodisperse pure silica nanoparticles often involves fast stirring of the reaction solution, which is usually an alcohol-based media with low water loading. It additionally involves the addition of ammonia to the reaction solution in order to fine-control the hydrolysis of the silica precursors and some use a two-step procedure with per-hydrolysis of small silica clusters. Some of these aspects may be applied to the synthesis of origami@SiO_2 and improve the quality of the origami's silica coating. In this context the complementary analysis of origami@SiO_2 with high-resolution cryogenic transmission electron microscopy (cryo-TEM) may give additional insights on the origami@SiO_2's surface structure and the degree of porosity in the silica coating. The latter may be also determined by SAXS, if the origami@SiO_2 objects are highly monodisperse, non-aggregated and display a smooth surface. Determining the silica's degree of porosity may contribute to answer the question if and to which

extend ion or even small enzyme exchange can be maintained through a silica shell.
Rapid sedimentation of heavy nanoparticles such as origami@SiO_2 or large DNA crystals during SAXS measurements was a major technical problem in the past, not only at the LMU laboratory setup but also at synchrotron beamlines with sub-second measurement times. This was solved by the design of a new sample holder, which tumbles the liquid probe with constant speed around the X-ray beam axis. This simple technique expands the range of potential SAXS samples tremendously and enables among others in-situ studies of DNA crystal assembly and its disintegration in the future.
Within this thesis, SAXS was demonstrated to allow not only the characterization of complex nanoconstructs at physiologically relevant conditions, but also the investigation of nanoagents while performing a specific tasks. Many X-ray studies contributed to optimize the nanoagents' envisioned operation. However, pushing the limits of light and X-ray exposure times, developing new photoswitchable compounds or perfecting the protocol of DNA origami templated silica growth will reveal new interesting phenomena in the future and leading the way towards new applications.

A. SUPPLEMENTARY DATA

A.1. Z→E switching of azobenzene lipid vesicles in deionized water

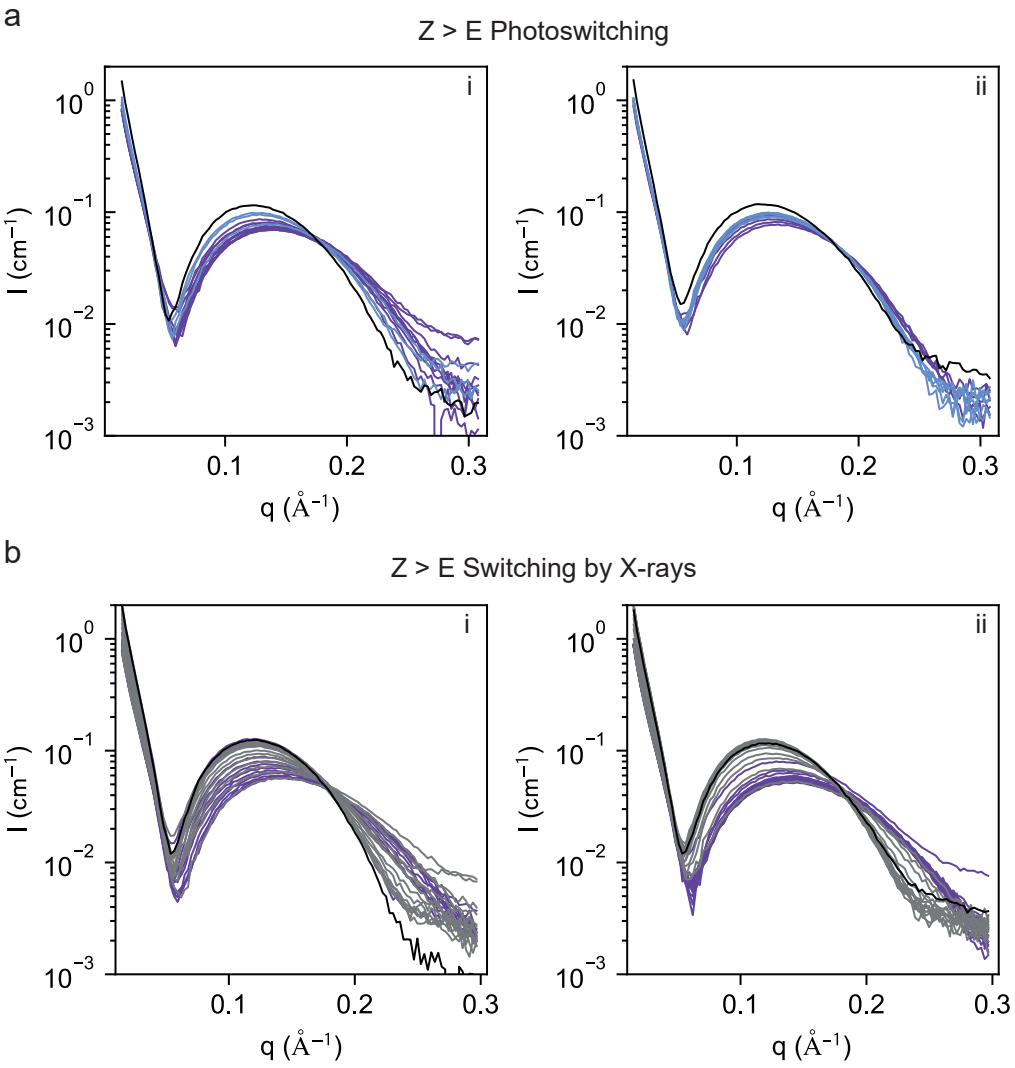

Figure A.1.: Switching of azobenzene lipid vesicles in water by light and X-rays (data related to Figure 4.17 b and Figure 4.19). a(i) SAXS measurements on azo-PC SUVs initially in the dark state (all-trans, black), then during 120 s of UV illumination (purple, increased %Z), then during 30 s of blue illumination (blue, %Z intermediate between UV and dark conditions). a(ii) SAXS measurements as in a(i), but using 60 s of UV and 60 s of blue illumination. b(i) SAXS measurements on azo-PC SUVs initially in the dark state (black, all-trans) then during 205 s of UV illumination (purple) then during subsequent X-ray exposures (grey). b(ii) SAXS measurements as in b(i), but using 105 s of UV illumination. X-ray exposure and delay times are given in Table A.1.

A.2. Detailed timing parameters for LED pump X-ray probe experiments

	Number of X-ray exposures	X-ray exposure time [s]	X-ray off time [s]	$t_{UV}[s]$	$t_{blue}[s]$
Fig.A.1a(i)	15	5	5	120	30
Fig.A.1a(ii)	12	5	5	60	60
Fig.A.1b(i)	40	5	5	205	
Fig.A.1b(ii)	30	5	5	105	
Fig.4.16 (8keV)	20	1	19	160	

Table A.1.: Detailed timing parameters for LED pump X-ray probe SAXS experiments for data shown in different Figures as indicated in the first column.

A.3. The influence of the silica precursor TMAPS on the 24 helix-bundle

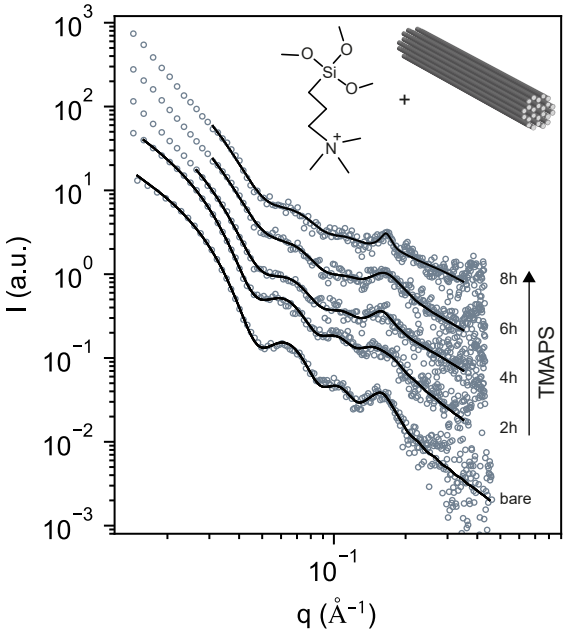

Figure A.2.: SAXS intensities of bare 24-HBs and after the addition of TMAPS (gray circles) together with the best fit of a cylinder model and a Lorentz peak accounting for the honeycomb lattice structure (solid black lines).

A.4. Temperature stability of silica-coated 24 helix-bundles verified by TEM

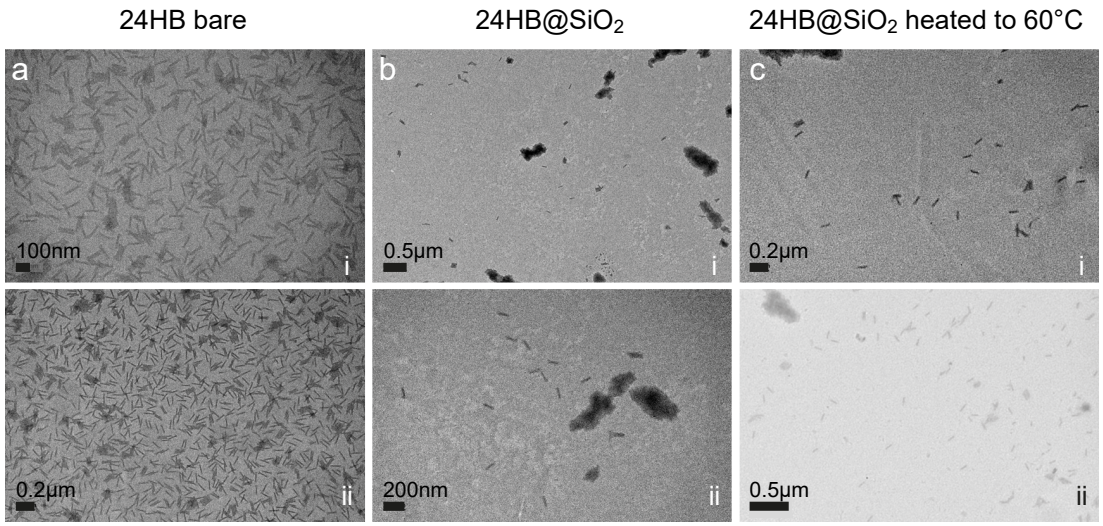

Figure A.3.: Temperature stability of 24-HB@silica verified by TEM. TEM micrograph of (a) bare 24-HBs, (b) 24-HB@SiO_2 with subnanometer silica coating at room temperature and (c) after heating to60° for 30 min are shown. TEM images were taken by L. Wassermann.

A.5. The influence of the silica precursor TMAPS on the three layer bloc

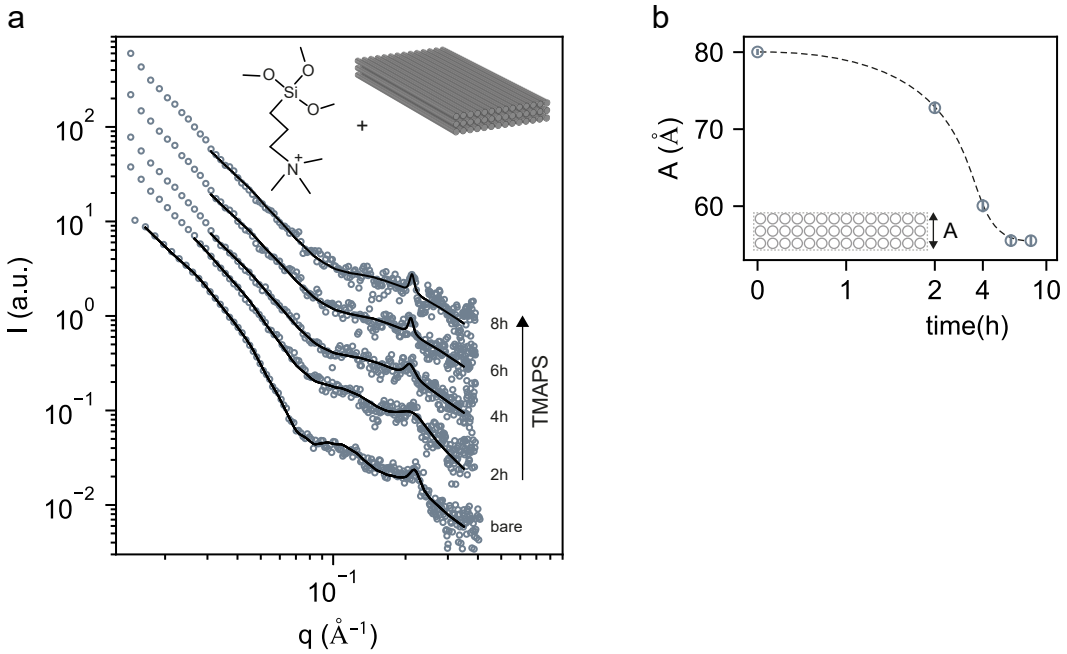

Figure A.4.: a. SAXS intensities of bare 3-LBs and after the addition of TMAPS (gray circles) together with the best fit of a cuboid model and a Lorentz peak accounting for the squared lattice structure (solid black lines). b. Heights of the overall cuboid-shaped 3-LBs are extracted from (a) as a function of TMAPS incubation time.

B. ASSOCIATED MANUSCRIPT

A previous version of this manuscript was published on the pre-print server arXiv [1].

B.1. Full text manuscript

In situ small-angle X-ray scattering reveals strong condensation of DNA origami during silicification

Martina F. Ober[1], Anna Baptist[2], Lea Wassermann[2], Amelie Heuer-Jungemann[2,*], and Bert Nickel[1,*]

[1] Faculty of Physics and CeNS, Ludwig-Maximilians-Universiät München, Geschwister-Scholl-Platz 1, 80539 Munich, Germany
[2] Max Planck Institute of Biochemistry and Center for Nanoscience (CeNS), Ludwig-Maximilians-Universität München, Am Klopferspitz 18, 82152 Martinsried, Germany

Corresponding authors: *heuer-jungemann@biochem.mpg.de, nickel@lmu.de

Version 23th April 2022

Abstract *The silicification of DNA origami structures increases their mechanical and thermal stability and provides chemical protection. So far, it is unclear how silicification affects the internal structure of the DNA origami and whether the whole DNA framework is embedded or if silica just forms an outer shell. By using in situ small-angle X-ray scattering (SAXS), we show that the net-cationic silica precursor TMAPS induces substantial condensation of the DNA origami, which is further enhanced by the addition of TEOS at early reaction times to an almost 10 % size reduction. We identify the SAXS Porod invariant as a reliable, model-free parameter for the evaluation of the amount of silica formation at a given time. Contrast matching of the DNA double helix Lorentzian peak reveals that silica growth also occurs on the inner surfaces of the origami. The less polar silica forming within the origami structure, replacing more than 40 % of the internal hydration water causes a hydrophobic effect: origami condensation. In the maximally condensed state, thermal stabilization of the origami up to 60 °C could be observed. If the reaction is driven beyond this point, the overall size of the silicified origami increases again due to more and more silica deposition on the DNA origami. DNA origami objects with flat surfaces show a strong tendency towards aggregation during silicification, presumably driven by the very same entropic forces causing condensation. Our studies provide novel insights into the silicification reaction and hints for the formulation of optimized reaction protocols.*

Introduction

DNA origami[1] is a versatile bottom-up nanofabrication technique to engineer nanometer-sized objects with sub-nanometer precision and complete site-specific addressability due to the programmable self-assembly of complementary DNA strands[2]. Potential applications of such DNA origami objects are manifold and include bio-sensing[3], drug delivery, as well as various biophysical[4] and biomedical applications[5, 6, 7, 8, 9]. A major bottleneck of utilizing DNA origami nanostructures in biomedical applications, however, is their inherent instability in common biological buffers and cellular environments as well as their susceptibility to enzymatic degradation[10, 11, 12]. Therefore, there is a need to increase the chemical, thermal and mechanical stability of DNA origami nanostructures in order to unravel their full potential and utilization in real-life applications.

One recently reported approach to achieve higher stability of DNA origami nanostructures is their encapsulation in a protective silica shell. Resulting structures are even stable in the absence of salt-containing buffers, at high temperatures, and in the presence of nucleases[7, 13, 14]. We demonstrated silicification of single DNA origami nanostructures and 3D DNA origami crystals[15], resulting in mechanical enforcement. This stabilization allowed us to analyse these fragile origami structures in the dry state, without suffering from structural collapse[13, 16]. Silicified DNA origami structures are promising candidates for biomedical applications and they play a prominent role for the customized synthesis of inorganic dielectric 2D[17, 18] and 3D nanomaterials[7, 19, 20].

The silicification process is a sol-gel approach based on a modified Stöber reaction[7, 13, 14]. The reaction is initiated through the electrostatic interactions of the quaternary ammonium head group of N-trimethoxysilylpropyl-N,N,N-trimethylammonium chloride (TMAPS) and the anionic DNA phosphate backbone. Siloxane groups on TMAPS then provide co-condensation sites for tetraethyl orthosilicate (TEOS) and enable silica growth. The successful growth of silica on DNA origami nanostructures was thus far mainly evidenced through analysis of structures in the dry state via transmission electron microscopy (TEM), scanning electron microscopy (SEM), atomic force microscopy (AFM) and energy dispersive X-ray spectroscopy (EDX)[7, 13, 14]. “Shell” thicknesses were inferred indirectly through microscopy images. However, to date it is unclear how the silicification reaction commences and whether silica grows as a “shell” around the origami, or if silica also penetrates the internal structure of the helix bundles.

In view of many possible applications of silicified-DNA origami nanostructures, especially as sculptured dielectrics, detailed understanding of the internal structure is essential in order to rationalize the protective nature of the silicification and its dielectric properties. Nevertheless, conventionally applied microscopy and spectroscopy techniques do not allow for such detailed investigation and analysis. In order to gain access to the required knowledge on the silicification process, we here use small-angle X-ray scattering (SAXS), a well-established structural tool to study DNA origami[12, 15, 21] and silica nanocomposites at physiological conditions in solution[22, 23]. Here, via *in situ* SAXS, we reveal and quantify a TMAPS-induced condensation of the inner double helix spacing of 24 helix bundles (24HBs) and four-layered origami bricks (4-LBs), as well as an outer shape contraction. Silica forms both on the inside and outside of the DNA origami as revealed by X-ray contrast matching. The inner order of the origami and the overall shape are well-preserved. We demonstrate that silica penetration into the origami structure is the main cause for increased thermal stability up to 60°C rather than an outer silica shell. Moreover, we observe that DNA origami with flat surfaces show increased tendency towards aggregation during silicification.

Materials and Methods

Folding and purification of DNA origami structures

Both DNA origami structures used here were designed using the CaDNAno software[24] (design schematics in **Figures S1-3** and **Table S1**)

24HB: The 24HB structure (design schematics in **Figure S1a** and **Figure S2**) was folded using 30 nM of DNA scaffold p8064 (tilibit nanosystems GmbH, Germany), and 100 nM of each staple oligonucleotide (Eurofins Genomics Germany GmbH and Integrated DNA Technologies, Inc., USA) in buffer containing 400 mM Tris-Acetate, 1 mM EDTA (pH = 8) and 14 mM $MgCl_2$. The mixture was heated to 65°C and held at this temperature for 15 min, then slowly cooled down to 4°C over a period of 15 hours. For further details see[12].

The 24HBs were concentrated and purified from excess staples by two rounds of polyethylene glycol (PEG) precipitation and re-dispersion in buffer (1x TE, 3 mM $MgCl_2$). In brief, the origami folding solution was mixed in a 1:1 volumetric ratio with PEG precipitation buffer (15 % w/v PEG (MW: 8000 g/mol), 500 mM NaCl, 2x TE), adjusted to a $MgCl_2$ concentration of 10 mM and centrifuged at 16000 rcf for 25 min. The supernatant was removed and the DNA pellet was re-suspended in 0.5 mL of 1x

TE buffer containing 11 mM $MgCl_2$. The PEG precipitation step was repeated after 30 min of shaking, and the purified structures were re-suspended in the final buffer (1x TE, 3 mM $MgCl_2$). This solution was shaken for 24 h at room temperature at 350 rpm for complete dispersion of the origami. Concentration of the purified DNA origami solution (up to 270 nM or 1.4 g/L) was verified via absorption measurements (Thermo Scientific NanoDrop 1000 Spectrophotometer). The successful folding of structures was confirmed by TEM analysis. DNA origami solutions were stored at 4°C until further use.

4-LB: The 4-LB (design schematics in **Figure S1b** and **Figure S3**) was folded using 10 nM of the scaffold p8064 (tilibit nanosystems GmbH, Germany), 100 nM of each staple oligonucleotide (Integrated DNA Technologies, Inc., USA) in buffer containing 40 mM Tris, 20 mM acetic acid, 1 mM EDTA (pH = 8) and 18 mM $MgCl_2$. The mixture was heated to 65°C and held at this temperature for 15 min, then slowly cooled down to 20°C over a period of 16 hours. The 4-LB origami solution was concentrated and purified from excess staples by ultrafiltration. Briefly, the folding mixture (~2 mL) was divided over 4-5 Amicon Ultra filters (0.5 mL, 100 K, Millipore, USA) and each centrifuged at 8000 rcf for 8 min. The centrifugal steps were repeated 3-5 times with fresh buffer (1xTAE, 3 mM $MgCl_2$) added in every step. The resulting solution (~30 µL) was re-suspended in buffer and the procedure repeated. A purified origami solution of 100 - 120 µL in total with a concentration up to 270 nM (1.4 g/L) was obtained and stored at 4°C until further use. The correct folding of the DNA origami was confirmed by TEM analysis

Silica coating

110 µL of purified 24HBs (270 nM) were mixed with 0.67 µL of TMAPS (TCI, USA) (50% in methanol) and shaken at 350 rpm for 1 min in an Eppendorf tube. 2.67 µL of TEOS (Sigma Aldrich, USA) (50% in methanol) were added to the tube, followed by shaking for another 15 min. Finally, the solution was filled into a sample cell for SAXS, which tumbles slowly (50 rpm). This way, molar ratios of (1:5:12.5) of phosphate groups:TMAPS:TEOS, were achieved, respectively.

For the 4-LB structures, the TMAPS-only containing origami solution was filled into the SAXS tumbling chamber after shaking at 350 rpm for 1 min in an Eppendorf tube. Subsequently, TEOS (50% in methanol) was added 15 min later directly into the SAXS tumbling chamber.

TEM Imaging

TEM imaging was carried out using a JEM-1230 transmission electron microscope (JEOL) operating at 80 kV. For sample preparation 5 -10 µL of a solution containing (silicified) DNA origami structures were deposited on glow-discharged TEM grids (formvar/carbon-coated, 300 mesh Cu; TED Pella, Inc.) for at least 1 min, depending on sample concentration. For visualization, bare origami structures were negatively stained by briefly washing the grid with 5 µL of a 2% uranyl formate (UFO) solution followed by staining with UFO for 10 - 30 s. Silicified DNA origami were not stained, but washed twice with MilliQ water.

In house SAXS experiments

Most X-ray data were recorded at an in house Mo X-ray SAXS setup described in detail elsewhere[25]. We measured at 17.4 keV X-ray energy with an X-ray beam size of 1.0 x 1.0 mm² at the sample position. Sample-to-detector distance was 1 m. Data were recorded using a Dectris Pilatus 3 R 300K CMOS Detector (487 x 619 pixels of size (172 x 172) µm². We calibrated the sample to detector distance and the beam center position with silver behenate powder.

Synchrotron SAXS experiments

SAXS data from 24HB@SiO_2 before and after heating of the sample solution to 60 °C for 30 min were recorded at the Austrian SAXS beamline at ELETTRA synchrotron using a beam energy of 8 keV[26] and a beam size of 0.2 x 2.0 mm^2. The sample solution was loaded into 1.3 mm diameter quartz glass capillaries by flow-through. A Pilatus detector from Dectris Ltd., Switzerland with 981 × 1043 pixels of size 172 × 172 $µm^2$ served as detector.

Results

From previous reports, it is known that DNA silicification is a slow process, taking at least several hours, often up to 7 days[7, 13, 14]. Here we followed the silicification process via an X-ray lab source using Mo characteristic radiation[25]. Mo X-rays induce less radiation dose compared to Cu radiation of the same intensity[27], allowing for long *in situ* SAXS experiments without the risk of radiation damage to the sample. Furthermore, Mo radiation allows for larger sample lengths along the beam (10 mm vs. c.a. 1.5 mm) yielding more practical geometric constrains for SAXS sample cells. As DNA origami objects exhibit a tendency to sediment during silicification, we

constructed a special cell allowing for tumbling of the sample with ~ 1 round/s around its centre to ensure well-dispersed DNA origami solutions throughout the measurement (see supporting information **note S2** for details).

The silicification reaction was continuously analysed by SAXS measurements. These measurements are then binned in time to achieve the best signal to noise ratio. We found that a binning time of 1h was sufficiently fast to follow the silicification reaction with good X-ray statistics.

Prior to silicification, a reference measurement of the purified origami was taken. The SAXS intensity distribution for the bare 24HBs is shown in **Figure 1a**. The SAXS signal I(q) exhibits three distinct intensity oscillations with dips at q ≈ 0.05 $Å^{-1}$, q ≈ 0.09 $Å^{-1}$, and q ≈ 0.13 $Å^{-1}$. These dips are characteristic for the cylindrical shape of 24HBs. Modelling of the 24HB as a homogeneous cylinder[12] with radius $R_{bare} = 80.1 \pm 0.2Å$ allowed matching of the SAXS intensity in this q-range. At q ≈ 0.16 $Å^{-1}$, the SAXS intensity shows an additional, Lorentzian-shaped peak, which is not predicted by the homogeneous cylinder model. In order to reproduce this feature, the structure model was extended by the designed DNA double helix arrangement in a honeycomb lattice, as schematically depicted in **Figure S1a**. Within this established approach, the interhelical distance was found to be $a_{bare} = 26.2 \pm 0.3Å$.The values for R_{bare} and $a_{bare}$are in good agreement with our previously reported values for this origami type[12]. The full structure model is detailed in the **note S3** of the supporting information.

Next, we monitored the structural changes during silicification. X-ray measurements were taken over a period of up to 80 h. Silica growth was primed by the addition of TMAPS, and subsequently initiated by the injection of TEOS (see methods for details). To determine the time required for the silicification to reach completion, we evaluated the time dependence of the Porod invariant Q (**Figure 1b**). Briefly speaking, if the silicification reaction yields a product that scatters more intensely than the solvent, the Porod invariant Q will increase, and once the reaction stops, Q will saturate. The Porod invariant Q is a model-free measure of the total scattering contrast ($\Delta\rho$) of the overall sample solution, which was obtained here essentially by numerical integration of the SAXS intensities shown in **Figure 1a** (see **note S4** for details). For the bare 24HBs we obtained $Q_{bare}^{24HB}(t = 0h) = 0.3 \cdot 10^{-3} cm^{-1}Å^{-3}$. During silicification, Q increased as a function of time. Since the electron density of amorphous silica ($\rho_{SiO2} \approx 19 \cdot 10^{-6}Å^{-2}$)

is larger than the electron density of water ($\rho_{H2O} = 9.4 \cdot 10^{-6}\text{Å}^{-2}$), this finding is consistent with increasing silica deposition *on* or *in* the 24HBs. The Porod invariant was observed to saturate after ~ 24 h suggesting that the reaction had already finished at this time. This is an interesting finding since this time is much shorter than reaction times reported previously[13] where reactions took up to a week. A possible explanation could be that in these reports the silicification reaction mixture was left to react undisturbed at temperatures slightly below RT, while here during the measurement gentle tumbling was applied at RT in order to avoid sedimentation. Silicification reaction kinetics are highly influenced by movement, pH and temperature, therefore tumbling at RT may have in avertedly sped up the reaction[28].

Per se, the Porod invariant is not sensitive to the distribution of the silica. Therefore, we now analyse the temporal intensity changes of the Lorentzian peak (I_{Lor}), which is sensitive to the inner structure of the DNA origami. Strikingly, as can be seen in **Figure 1c**, this peak vanished shortly after the reaction started. However, after running the silicification reaction for more than 4 h, the Lorentzian peak recovered in intensity, surpassing the initial intensity level and even showing a second order peak at q ≈ 0.32 Å^{-1} (cf. **Figure 1a)**. The disappearance and recovery of a diffraction peak is a phenomenon known as contrast matching. Contrast matching occurs if the scattering length between an object and its matrix are equal[29]. The scattering length densities from water, DNA, and silica are $\rho_{H2O} = 9.4 \cdot 10^{-6}\text{Å}^{-2}$, $\rho_{DNA} = 13 \cdot 10^{-6}\text{Å}^{-2}$, and $\rho_{SiO2} \approx 19 \cdot 10^{-6}\text{Å}^{-2}$, respectively. In turn, once ca. 40 % of the water volume fraction within the DNA origami voids are replaced by silica (x_{SiO2} = 0.375, compare **note S5** in the supporting information), contrast matching occurs, i.e., the diffraction peak vanishes, as observed in **Figure 1c** after 4 h. With more and more water being replaced by silica, contrast inversion, i.e., recovery of the diffracted intensity occurs as validated in **Figure 1c** for later reaction times. The helix peak intensity saturated after ~24 h in accordance with the saturation of the Porod invariant Q, indicating completion of the silicification reaction.

Previous studies on DNA origami silicification lacked information on whether silica is covering exclusively the outer surface of the DNA origami object, or penetrating the inner structure as well, embedding the individual helices [7, 13, 14, 17, 19]. The *in situ* SAXS results presented here clearly reveal that silica does forms in between the double helix arrangement of the origami structure. Since the equilibrium distance of the double helix

is a balance of attractive and repulsive forces, the question arises if this balance is distorted by the presence of silica. We can verify such changes by evaluating the origami cylinder radius (*R*) and the interhelical distance (*a*) of the 24HBs (cf. **Figure 2**). Since TMAPS binds to the DNA backbone through electrostatic interactions, condensation or expansion effects, as previously observed by us for change in ionic strength, or by osmotic effects, are possible[12].

So far it was unclear to which extend silicification changes the internal structure of a DNA origami. To disentangle potential effects of TMAPS and TEOS alone, bare 24HBs were incubated with TMAPS only, and studied for several hours. The corresponding SAXS data are shown in **Figure S5**. Both the 24HB cylinder radius (*R*) and interhelical distance (*a*) show a substantial decrease in response to interaction with TMAPS (cf. **Figure 2a, b**) after an incubation time of 4 h. After eight hours, we obtained a minimal cylinder radius of $R_{min}^{TMAPS} = 73.4 \pm 0.4$ Å and an interhelical distance of $a_{min}^{TMAPS} = 25.2 \pm 0.3$ Å. These observations indicate that the interaction of the DNA phosphate backbone with TMAPS condenses the outer radius by 6.7 ± 0.4 Å, and the DNA-double helix spacing by 1.0 ± 0.3 Å. Such a condensation of DNA origami objects in the early steps of silicification has never been observed before. We propose that TMAPS binding to the DNA backbone causes electrostatic screening reducing the repulsion between neighbouring helices[12, 30, 31, 32], possibly in conjunction with water depletion effects. The initial lag of 4 h incubation time suggests that TMAPS accesses the phosphate groups by obstructed diffusion.

Interestingly, we observed this condensation effect even faster if TEOS was added immediately after TMAPS injection. During the first 4 h of silica growth, the cylinder radius decreased down to $R_{min} = 74.2 \pm 0.5$ Å (cf. **Figure 2c**) and the minimal interhelical distance $a_{min}(t = 8\ h) = 23.8 \pm 0.2$ Å could already be observed after 8 h (cf. **Figure 2d**). This accelerated condensation suggests hydrophobic effects within the origami in response to early silica formation.

A naïve comparison of the radius before (R_{bare}) and after silicification (R_{SiO2}) would suggest that there is no silica shell on the outside of the origami at all. However, since the honeycomb lattice of 24HBs remains significantly condensed even towards the end of the reaction ($a_{SiO2} = 24.7 \pm 0.05$ Å), the definition of the "outer silica shell thickness" requires some caution. We suggest that the difference between the cylinder radius at

the end of the reaction ($R_{SiO2} = 80.4 \pm 0.1$ Å) to the most condensed radius (R_{min}) is a realistic upper limit for the silica encapsulation thickness. Here, we found $(R_{SiO2} - R_{min}) = 6.2 \pm 0.3$ Å. Thus, the outer silica shell thickness is clearly in the sub-nanometer range.

Silicified DNA origami show impressive thermal stability (heating up to 1200 °C)[13, 14, 33]. We wondered if the early condensed state of the origami with about 40 % silica infill and sub-nanometer shell already shows such enhanced temperature stability. To answer this question, we heated a DNA origami at the maximally condensed state ($R = 74.5 \pm 0.4$ Å) to 60 °C for 30 min. Bare 24HBs fully melt at this temperature[12]. Contrastingly, the silicified structures remained intact as confirmed by SAXS and TEM analysis (cf. **Figure 3**). Surprisingly, it appears that the 40 % silica frosting in the condensed origami state already provides substantial thermal stability.

All origami discussed so far were cylindrically shaped 24HBs. In order to verify our findings, we also studied cuboid, brick shaped origami during silicification and noted a great tendency towards aggregation, which is already visible by naked eye as macroscopic clouds in solution. However, in view of the entropic forces at work during silicification, this is expected since depletion forces are best known for favouring aggregation of colloids[34]. Since the outer coating here is sub-nanometer, strongly curved cylindrical origami apparently do not possess enough contact area to develop such strong aggregates. Flat surfaces of brick-like DNA structures, however, readily form aggregates. To explore this scenario on the molecular level, we investigated the silicification of a cuboid DNA origami, i.e. the 4-LB, also designed on a honeycomb lattice.

The SAXS intensity for the 4-LBs before silicification exhibits one to two distinct oscillations with dips at q ≈ 0.07 $Å^{-1}$ and q ≈ 0.13 $Å^{-1}$, characteristic for the overall cuboid shape of 4-LBs, see **Figure 4a**. Additionally, a pronounced Lorentzian peak arising from the honeycomb lattice design can be observed. The thickness (A) of the 4-LB origami is small enough to be extracted with high precision from the SAXS data a cuboid model (cf. **Figure 4c**). We obtained a thickness of $A_{bare} = 89.9 \pm 0.4$ Å. At this stage, the brick-like 4-LB origami is well dispersed, i.e., SAXS data can be modelled without the need for a structure factor.

After initiating silicification, the Porod invariant Q saturates already after ~ 4 h, i.e.,

much earlier than in the case of the 24HB (cf. **Figure 4b**). The overall increase of the Q value after silicification is only about half compared to that of the 24HBs. During silica formation the brick thickness is condensed to a minimal thickness of $A_{min}(t = 56\ h) = 80.3 \pm 1.3$ Å. However, we did not observe a reversal of the condensation effect. In agreement with this observation, the origami reaches the contrast matching condition, i.e., the helix-helix peak vanished, but there is no recovery. Instead, we observe an upturn of SAXS intensity at small q-values during the 4-LBs' silica growth in **Figure 4a**, which is an established fingerprint of aggregation. In some cases, this aggregation gives rise to a particle-particle stacking peak (cf. **Figure S6**). We therefore conclude that DNA origami with flat surfaces show increased tendency towards aggregation during silicification possibly due to increased entropic forces on the cuboid surface. This aggregation may even obstruct influx of further silica particles into the origami. So somewhat paradoxically, the brick particles here form rather large aggregates without reaching similar silica uptake compared to cylindrical origami. Nevertheless, the 4-LB, similar to the 24HB showed increased thermal stability after 4 h of silicification, i.e. with an ultrathin outer silica coating, suggesting that enough silica deposition occurred to preserve the brick shape (**Figure S7)**.

Discussion

The Porod invariant Q turns out to be a model free indicator for the kinetics and yield associated with DNA origami silicification. Silicification of DNA origami is a rather slow process and the initial phase is characterized by a pronounced condensation upon silica incorporation. In general, silicification under similar conditions exhibits two reaction phases: Initially, TMAPS primes the silica polymerization reaction which then consumes TEOS yielding "primary silica particles", or better, short silica chains of here maybe in average 3-4 units (ratio TEOS 2.5:TMAPS 1). These primary silica particles should form within minutes, i.e., much faster than the silicification reaction kinetics observed here, which takes hours. We therefore suggest that the silicification reaction of the DNA origami here is driven by phase two of the general silicification reaction; aggregation of primary silica particles and their condensation into silica networks[28, 35, 36]. This scenario implies diffusion of the primary particles (silica chains) into the DNA origami and subsequent electrostatic binding of cationic TMAPS-TEOS precursors to anionic DNA. Binding of these less polar chains to the internal surfaces of DNA helices gives rise to hydrophobic effects, such as initial condensation of all of the origami

structures studied. Binding to the outer surfaces favors strong aggregation of brick-shaped origami, even for ultrathin shells.

Conclusions

Using *in situ* SAXS we were able to show that a strong condensation of DNA origami nanostructures occurs during silicification. Silica deposition is not limited to the outside of the origami, but also occurs within the individual helix bundles. Interestingly, cuboidal DNA origami structures showed strong signs of aggregation during silicification and an overall decreased level of silica deposition compared to cylindrical DNA origami structures. Silica "shells" observed for both origami shapes used here are in the sub-nanometer regime, yet provide sufficient stability for shape retention at high temperatures over an extended period of time. We expect that these insights into the molecular arrangements during synthesis are key to the development of enhanced silicification protocols of DNA origami needed to fabricate e.g. sculptured dielectrics. One key requirement is to prevent aggregation of planar structures, possibly by inclusion of some bulky, water-soluble silanes, which bind only to the outer origami surface due to steric hindrance. Another aspect is that the inner part of the origami should be more readily accessible to primary silica particles to prevent their assembly outside of the origami. For this purpose, small primary particles may be explored followed by subsequent further additions of TEOS. It is well-documented that TEOS, following full or partial hydrolysis preferentially reacts with larger silica clusters rather than with itself, which, in this case, would be provided by the partially silicified DNA origami[36]. By following a careful step-by-step silicification approach, this could lead to a higher degree of control over silica shell thickness and overall structure stability.

Acknowledgements

We acknowledge financial support from the German Research Foundation (DFG) through SFB1032 (Nanoagents) projects A06 and A07 number 201269156; the BMBF grant no. 05K19WMA (LUCENT) and by the Bavarian State Ministry of Science, Research, and Arts grant "SolarTechnologies go Hybrid (SolTech)". A.H-J acknowledges funding from the DFG through the Emmy Noether program (project no. 427981116). This work benefited from SasView software, originally developed by the DANSE project under NSF award DMR-0520547. We would like to thank Heinz Amenitsch for assistance in using the SAXS beamline at the synchrotron Elettra in Trieste and the CERIC-ERIC Consortium for the access to experimental facilities. Also, we would like to thank Marianne Braun for help with TEM imaging.

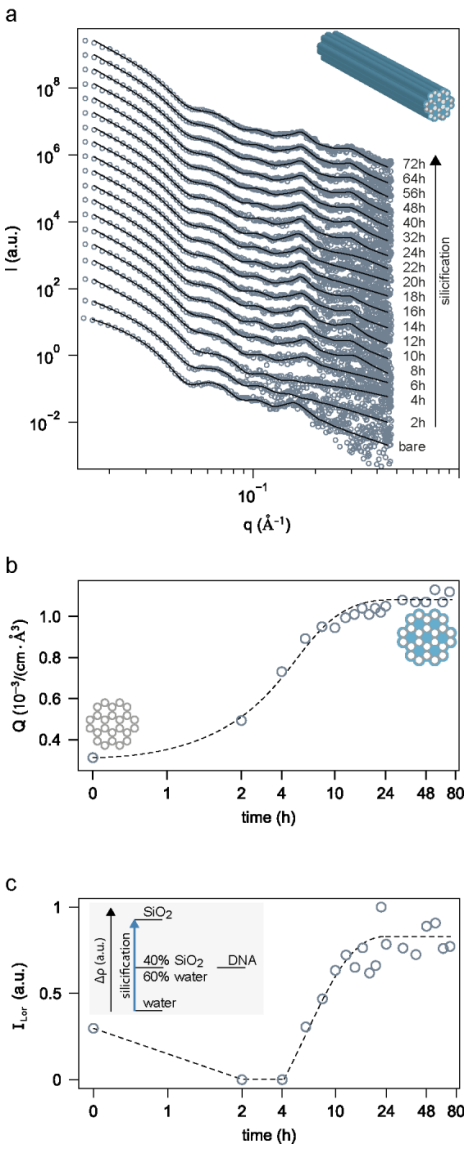

Figure 1 In situ silicification of 24HBs while tumbling with constant speed (50rpm) monitored by SAXS. SAXS data is recorded for bare 24HB and during silicification (a). The data is shown together with the best fits of a cylinder model together with Lorentzian peaks accounting for the inner honeycomb lattice arrangement. Data is scaled for clarity. Model-free Porod invariant Q (b) as a measure of the overall scattering contrast and normalized interhelical peak intensities I_{Lor} (c) are extracted from the SAXS data shown in (a) as function of silica growth time. 24HB shape with honeycomb lattice structure is shown in the inset. Dashed line serves as guide to the eye.

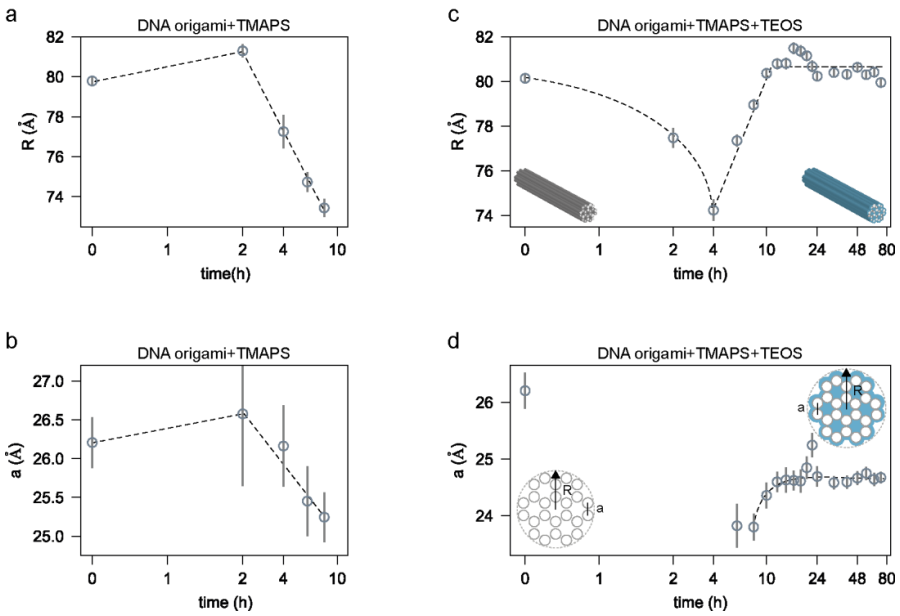

Figure 2 Radii of the overall cylinder-shaped 24HBs and interhelical distance extracted from **Figure S3** and **Figure 1a** as a function of TMAPS incubation time (a,b) and silica growth induced by TMAPS and TEOS (c,d). Dashed lines serve as guide to the eye. Schematic of the 24HB honeycomb lattice structure are shown as insets.

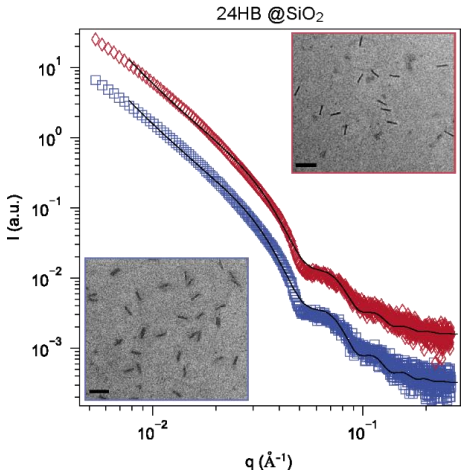

Figure 3 Temperature stability of extremely condensed silicified 24HBs verified by SAXS and TEM. SAXS intensities of 24HBs@SiO_2 ($R_{SiO2} = 74.5 \pm 0.4$Å) measured at room temperature (blue squares) and after heating the structures to 60 °C for 30 min (red diamonds) and TEM micrographs of 24HB @SiO_2 at room temperature (blue frame) and after heating to 60°C for 30 min (red frame) are shown in the insets. Scale bars: 200 nm.

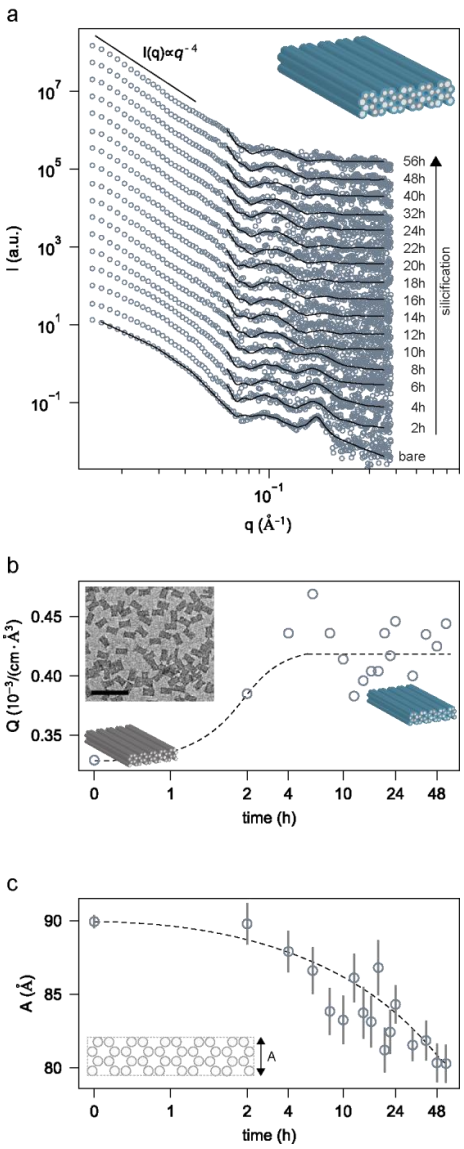

Figure 4 SAXS intensities of bare 4-LBs and during silicification together with the best fit of a cuboid model and Lorentzian peaks accounting for the honeycomb lattice structure. Data is scaled for clarity. b. Silica growth time dependence of the model-free Porod invariant Q extracted from (a) and a TEM micrograph of 4-LB @SiO_2. Scale bars: 200 nm. b. Heights of the overall cuboid shaped 4-LB as function of silica growth time. Schematic 4-LB cuboid shape with honeycomb lattice structure and front view are shown in the insets. Dashed lines serve as guide to the eye.

References

1. Rothemund PWK. Folding DNA to create nanoscale shapes and patterns. *Nature* 2006, **440**(7082)**:** 297-302.

2. Seeman NC, Sleiman HF. DNA nanotechnology. *Nature Reviews Materials* 2018, **3**(1)**:** 17068.

3. Ochmann SE, Vietz C, Trofymchuk K, Acuna GP, Lalkens B, Tinnefeld P. Optical Nanoantenna for Single Molecule-Based Detection of Zika Virus Nucleic Acids without Molecular Multiplication. *Analytical Chemistry* 2017, **89**(23)**:** 13000-13007.

4. Nickels PC, Wünsch B, Holzmeister P, Bae W, Kneer LM, Grohmann D*, et al.* Molecular force spectroscopy with a DNA origami-based nanoscopic force clamp. *Science* 2016, **354**(6310)**:** 305-307.

5. Hu Q, Li H, Wang L, Gu H, Fan C. DNA Nanotechnology-Enabled Drug Delivery Systems. *Chemical Reviews* 2019, **119**(10)**:** 6459-6506.

6. He L, Mu J, Gang O, Chen X. Rationally Programming Nanomaterials with DNA for Biomedical Applications. *Advanced Science* 2021, **8**(8)**:** 2003775.

7. Liu X, Zhang F, Jing X, Pan M, Liu P, Li W*, et al.* Complex silica composite nanomaterials templated with DNA origami. *Nature* 2018, **559**(7715)**:** 593-598.

8. Berger RML, Weck JM, Kempe SM, Hill O, Liedl T, Rädler JO*, et al.* Nanoscale FasL Organization on DNA Origami to Decipher Apoptosis Signal Activation in Cells. *Small* 2021, **17**(26)**:** 2101678.

9. Ijäs H, Shen B, Heuer-Jungemann A, Keller A, Kostiainen Mauri A, Liedl T*, et al.* Unraveling the interaction between doxorubicin and DNA origami nanostructures for customizable chemotherapeutic drug release. *Nucleic Acids Research* 2021, **49**(6)**:** 3048-3062.

10. Perrault SD, Shih WM. Virus-Inspired Membrane Encapsulation of DNA Nanostructures To Achieve In Vivo Stability. *ACS Nano* 2014, **8**(5)**:** 5132-5140.

11. Paunescu D, Puddu M, Soellner JOB, Stoessel PR, Grass RN. Reversible DNA encapsulation in silica to produce ROS-resistant and heat-resistant synthetic DNA 'fossils'. *Nature Protocols* 2013, **8**(12)**:** 2440-2448.

12. Fischer S, Hartl C, Frank K, Radler JO, Liedl T, Nickel B. Shape and Interhelical Spacing of DNA Origami Nanostructures Studied by Small-Angle X-ray Scattering. *Nano Lett* 2016, **16**(7)**:** 4282-4287.

13. Nguyen L, Döblinger M, Liedl T, Heuer-Jungemann A. DNA-Origami-Templated Silica Growth by Sol-Gel Chemistry. *Angewandte Chemie International Edition* 2019, **58**(3)**:** 912-916.

14. Nguyen M-K, Nguyen VH, Natarajan AK, Huang Y, Ryssy J, Shen B*, et al.* Ultrathin Silica Coating of DNA Origami Nanostructures. *Chemistry of Materials* 2020, **32**(15)**:** 6657-6665.

15. Zhang T, Hartl C, Frank K, Heuer-Jungemann A, Fischer S, Nickels PC*, et al.* 3D DNA Origami Crystals. *Adv Mater* 2018**:** e1800273.

16. Wang Y, Dai L, Ding Z, Ji M, Liu J, Xing H*, et al.* DNA origami single crystals with Wulff shapes. *Nature Communications* 2021, **12**(1)**:** 3011.

17. Shang Y, Li N, Liu S, Wang L, Wang Z-G, Zhang Z*, et al.* Site-Specific Synthesis of Silica Nanostructures on DNA Origami Templates. *Advanced Materials* 2020, **32**(21)**:** 2000294.

18. Zhao Y, Zhang C, Yang L, Xu X, Xu R, Ma Q*, et al.* Programmable and Site-Specific Patterning on DNA Origami Templates with Heterogeneous Condensation of Silver and Silica. *Small* 2021**:** 2103877.

19. Jing X, Zhang F, Pan M, Dai X, Li J, Wang L*, et al.* Solidifying framework nucleic acids with silica. *Nature Protocols* 2019, **14**(8)**:** 2416-2436.

20. Michelson A, Zhang H, Xiang S, Gang O. Engineered Silicon Carbide Three-Dimensional Frameworks through DNA-Prescribed Assembly. *Nano Letters* 2021, **21**(4)**:** 1863-1870.

21. Hartl C, Frank K, Amenitsch H, Fischer S, Liedl T, Nickel B. Position Accuracy of Gold Nanoparticles on DNA Origami Structures Studied with Small-Angle X-ray Scattering. *Nano Letters* 2018, **18**(4)**:** 2609-2615.

22. Balmer JA, Mykhaylyk OO, Armes SP, Fairclough JPA, Ryan AJ, Gummel J*, et al.* Time-Resolved Small-Angle X-ray Scattering Studies of Polymer−Silica Nanocomposite Particles: Initial Formation and Subsequent Silica Redistribution. *Journal of the American Chemical Society* 2011, **133**(4)**:** 826-837.

23. Han H, Li L, Wang W, Tian Y, Wang Y, Wang J*, et al.* Core-Shell-Corona Silica Hybrid Nanoparticles Templated by Spherical Polyelectrolyte Brushes: A Study by Small Angle X-ray Scattering. *Langmuir* 2017, **33**(38)**:** 9857-9865.

24. Douglas SM, Dietz H, Liedl T, Högberg B, Graf F, Shih WM. Self-assembly of DNA into nanoscale three-dimensional shapes. *Nature* 2009, **459**(7245)**:** 414-418.

25. Bruetzel LK, Fischer S, Salditt A, Sedlak SM, Nickel B, Lipfert J. A Mo-anode-based in-house source for small-angle X-ray scattering measurements of biological macromolecules. *Review of Scientific Instruments* 2016, **87**(2)**:** 025103.

26. Amenitsch H, Bernstorff S, Laggner P. High-flux beamline for small-angle x-ray scattering at ELETTRA. *Review of Scientific Instruments* 1995, **66**(2)**:** 1624-1626.

27. Ober MF, Müller-Deku A, Baptist A, Amenitsch H, Thorn-Seshold O, Nickel B. SAXS measurements of azobenzene lipid vesicles reveal buffer-dependent photoswitching and quantitative Z-> E isomerisation by X-rays. *arXiv preprint arXiv:211112570* 2021.

28. Yi Z, Dumée LF, Garvey CJ, Feng C, She F, Rookes JE*, et al.* A New Insight into Growth Mechanism and Kinetics of Mesoporous Silica Nanoparticles by in Situ Small Angle X-ray Scattering. *Langmuir* 2015, **31**(30)**:** 8478-8487.

29. Heller W. Small-angle neutron scattering and contrast variation: a powerful combination for studying biological structures. *Acta Crystallographica Section D* 2010, **66**(11)**:** 1213-1217.

30. Qiu X, Kwok LW, Park HY, Lamb JS, Andresen K, Pollack L. Measuring Inter-DNA Potentials in Solution. *Physical Review Letters* 2006, **96**(13)**:** 138101.

31. Roodhuizen JAL, Hendrikx PJTM, Hilbers PAJ, de Greef TFA, Markvoort AJ. Counterion-Dependent Mechanisms of DNA Origami Nanostructure Stabilization Revealed by Atomistic Molecular Simulation. *ACS Nano* 2019, **13**(9)**:** 10798-10809.

32. Ponnuswamy N, Bastings MMC, Nathwani B, Ryu JH, Chou LYT, Vinther M*, et al.* Oligolysine-based coating protects DNA nanostructures from low-salt denaturation and nuclease degradation. *Nature Communications* 2017, **8**(1)**:** 15654.

33. Majewski PW, Michelson A, Cordeiro MAL, Tian C, Ma C, Kisslinger K*, et al.* Resilient three-dimensional ordered architectures assembled from nanoparticles by DNA. *Science Advances* 2021, **7**(12)**:** eabf0617.

34. Lin K-h, Crocker JC, Prasad V, Schofield A, Weitz DA, Lubensky TC*, et al.* Entropically Driven Colloidal Crystallization on Patterned Surfaces. *Physical Review Letters* 2000, **85**(8)**:** 1770-1773.

35. Keefer KD, Schaefer DW. Growth of Fractally Rough Colloids. *Physical Review Letters* 1986, **56**(22)**:** 2376-2379.

36. Han Y, Lu Z, Teng Z, Liang J, Guo Z, Wang D*, et al.* Unraveling the Growth Mechanism of Silica Particles in the Stöber Method: In Situ Seeded Growth Model. *Langmuir* 2017, **33**(23)**:** 5879-5890.

B.2. Supporting information

Supporting Information

In situ small-angle X-ray scattering reveals strong condensation of DNA origami during silicification

Martina F. Ober[1], Anna Baptist[2], Lea Wassermann[2], Amelie Heuer-Jungemann[2,*], and Bert Nickel[1,*]

[1] Faculty of Physics and CeNS, Ludwig-Maximilians-Universiät München, Geschwister-Scholl-Platz 1, 80539 Munich, Germany
[2] Max Planck Institute of Biochemistry and Center for Nanoscience (CeNS), Ludwig-Maximilians-Universität München, Am Klopferspitz 18, 82152 Martinsried, Germany

Corresponding authors: *heuer-jungemann@biochem.mpg.de, nickel@lmu.de

Version 23th April 2022

S1: DNA origami shapes by design

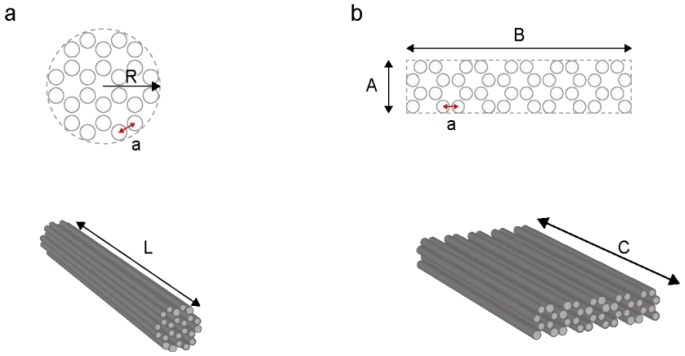

Figure S 1 Schematic DNA origami shapes and front views of a 24-HB with a honeycomb lattice design (a) and a 4-LB with a honeycomb lattice design (b). Each solid cylinder represents a DNA double helix.

DNA origami	A(Å)	B(Å)	C(Å)	R(Å)	L(Å)	#(helices)
24-HB	-	-	-	79	1000	24
4-LB	78	270	571	-	-	40

Table S 1 DNA origami dimensions by design. The values are calculated in Angström assuming a base pair distance of 0.34 nm, an average interhelical distance of 2.6 nm and a radius of a DNA double helix of 1 nm.

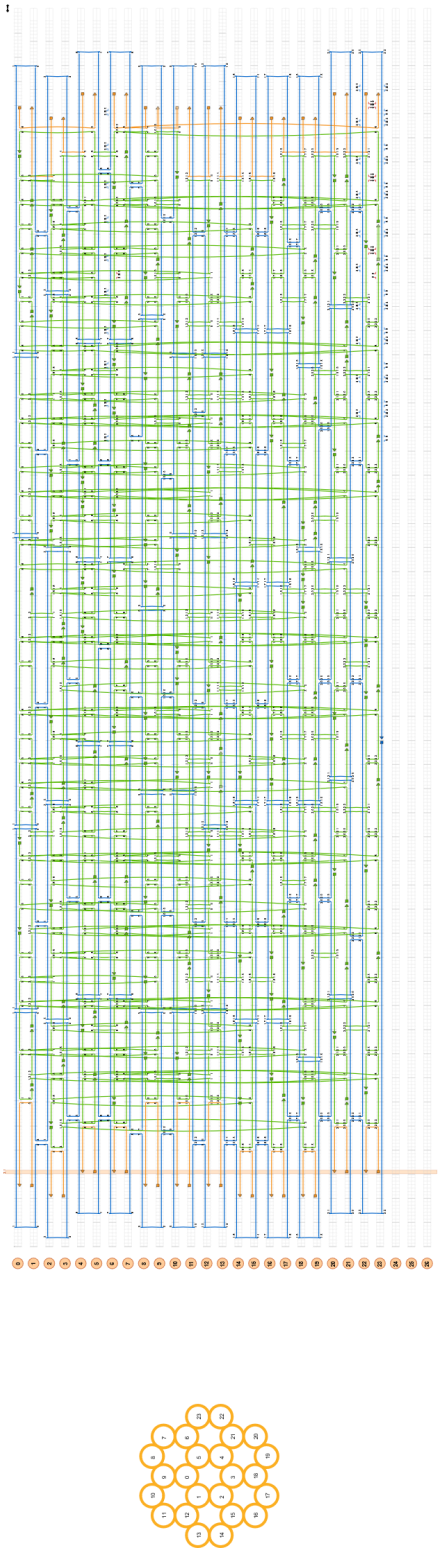

Figure S 2 Design diagram of the 24HB using caDNAno and cross-sectional view of the helices

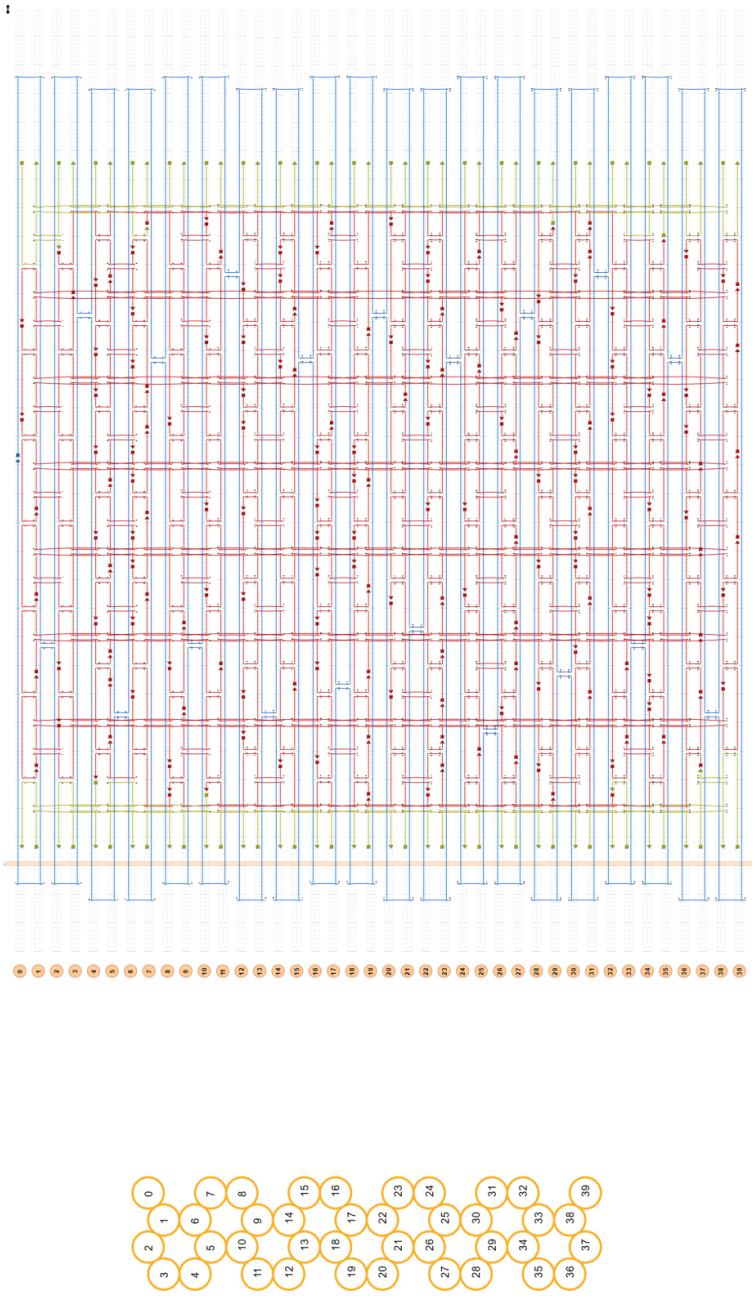

Figure S 3 Design diagram of the 4-LB using caDNAno and cross-sectional view of the helices

S2: Custom-built sample tumbler

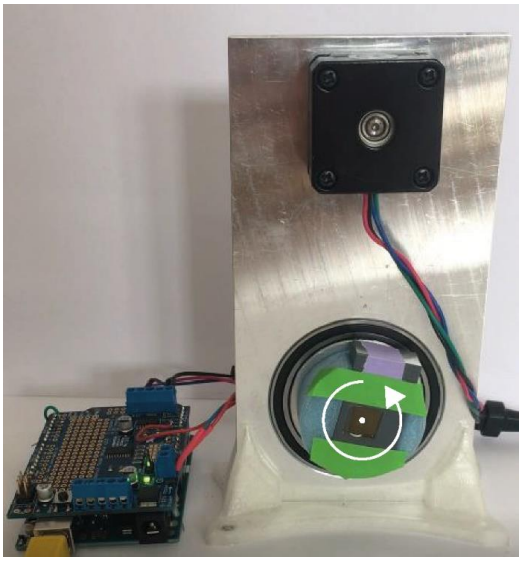

Figure S 4 Photograph of our custom-built sample tumbler, which rotates the sample with ~ 1 round/s around the X-ray beam axis to avoid sedimentation of origami@SiO_2.

S3: Small angle X-ray scattering (SAXS) analysis

All DNA origami dimensions, as well as their inner structure, are obtained from model fits of the total scattering intensity I(q) to a geometrical model describing the overall origami shape with additional peaks accounting for the inner helix arrangement (Fischer *et al.*, 2016). The scattering intensity is given in dependence of the scattering vector $q =$. Here, λ is the X-ray wavelength and 2θ the scattering angle. To analyse the scattering data of 24HB@SiO_2, we use a cylinder model together with a Debye background to account for free oligonucleotides, a power law to include the effects of aggregation, and Lorentzian peaks to account for the inner honeycomb lattice structure, as given in equations (1) - (5).

$$I(q) \propto \frac{s_{cyl}}{V_{cyl}} \int_0^{\frac{\pi}{2}} {F_{cyl}}^2(q) sin(\alpha) d\alpha + s_{deb} F_{deb}(q) + s_{pow} F_{pow}(q) + s_{hk} F_{lor}(q) \quad (1)$$

$$F_{cyl}(q) = (\rho_{DNA} - \rho_{water}) V_{cyl} \frac{sin\left(q\frac{L}{2}cos\frac{\alpha}{2}\right)}{q\frac{L}{2}cos\frac{\alpha}{2}} \frac{2J_1\left(qRsin(\alpha)\right)}{qRsin(\alpha)} \quad (2)$$

Here, J_1 is the first order Bessel function, α the angle between the cylinder axis and the *q-vector*, *L* the length of the cylinder core, *R* the radius of the cylinder core, V_{cyl} is the cylinder volume and $\rho_{DNA/water}$ the electron density of DNA and water, respectively.

$$F_{deb}(q) = \frac{2\left(exp\left(-q^2R_g^2\right) - 1 + q^2R_g^2\right)}{\left(q^2R_g^2\right)^2} \quad (3)$$

$$F_{pow}(q) = q^{-x} \quad (4)$$

R_g is the radius of gyration and *x* the exponent of the power law.

$$F_{lor}(q) = \frac{1}{1 + \left(\frac{q - q_0}{B}\right)^2} \quad (5)$$

Here, q_0 is the peak position and *B* is the half-width-half-maximum of the Lorentz peak. q_0 is directly related to the lattice spacing d via $d = \frac{2\pi}{q_0}$. For DNA origamis with a hexagonal lattice, i.e. a 24HB and the 4-LB, we have $a_{hexagonal} = \sqrt{\frac{4}{9}}d = \frac{2}{3}\frac{2\pi}{q_0}$ as a result of the relation $\frac{1}{d} = \frac{4}{3}\left(\frac{h^2+hk+k^2}{a^2}\right)$ which is valid for a 2D hexagonal lattice with *h* and *k* as Miller indices.

To analyse the scattering data of 4-LB@silca a cuboid model as given in equation (6) and (7) is used instead of a cylinder model (Mittelbach & Porod, 1961).

$$F_{cuboid}(q,\alpha,\beta) = \int_0^1 \phi_q\left(\mu\sqrt{1-\sigma^2}, a\right)\left[S\left(\frac{\mu c\sigma}{2}\right)\right]^2 d\sigma \quad (6)$$

$$\text{with } \phi_q(\mu,a) = \int_0^1 \left\{S\left[\frac{\mu}{2}cos\left(\frac{\pi}{2}u\right)\right] S\left[\frac{\mu a}{2}sin\left(\frac{\pi}{2}u\right)\right]\right\}^2 du, \quad (7)$$

$S(x) = \frac{sin(x)}{x}$, and$\mu = qB$. The substitution of $\sigma = cos\alpha$ and $\beta = \frac{\pi}{2}u$ are applied. Here, *A*, *B*, and *C* are the axis dimensions of the parallelepiped, *Δρ* the scattering contrast between DNA and water, α the angle between *C* and $\vec{q}$*, and* β the angle between the projection of the particles in the *xy*-plane and *y*-axis*.* Furthermore, it is assumed, that *a = A/B < 1, b = B/B = 1*, and *c = C/B > 1*.

During the model fitting the electron density of DNA ρ_{DNA} and water ρ_{water}, the length of the 24HB L, and the widths B and C of 4-LB were fixed to $\rho_{DNA} = 13 \cdot 10^{-6}\text{Å}^{-2}$, $\rho_{water} = 9.4 \cdot 10^{-6}\text{Å}^{-2}$,$\rho_{SiO2} = 19 \cdot 10^{-6}\text{Å}^{-2}$, $L = 1000\text{Å}$, $B^{4-LB} = 379\text{Å}$, $C^{4-LB} = 555\text{Å}$, $B^{3-LB} = 379\text{Å}$, and $C^{3-LB} = 627\text{Å}$. Model fitting was achieved by running the software internal population-based DREAM algorithm using the software package SasView (SasView, 2014). The q-range dominated by aggregation is excluded from model fitting.

S4: Calculation of the Porod invariant

The Porod invariant Q is a model-free measure of the total scattering contrast. For a two-phase system it is calculated via

$$Q = \int_0^\infty I(q)q^2dq \propto 2\pi^2\Delta\rho^2.$$

Thus, Q provides a measure of the total scattering contrast, which allows in our case to trace the silica growth. The calculation of Q relies on the extrapolation of the experimental scattering data $I(q)$ to small and large *q.* For extrapolation to small *q*, we fit the data to the Guinier function$I(q) = I_0 \cdot exp\left(\frac{-q^2R_g^2}{3}\right)$. Here, R_G denotes the radius of gyration, which quantifies the objects distribution of scattering length density. We further omit extrapolation of the data to large q due to increased noise and limit the integration to $q_{max} = 0.35\text{Å}^{-1}$. This way, we obtain the Porod invariant Q as function of silicification time (O. Glatter, 1982, Mantella *et al.*, 2020).

S5: Contrast matching

The concept of contrast matching, i.e. the vanishing of the scattering contrast between the DNA helices and their surrounding matrix, can be utilized to estimate the corresponding silica volume fraction.

$$x_{SiO_2} \cdot \rho_{SiO_2} + x_{H_2O} \cdot \rho_{H_2O} = \rho_{DNA} \quad (1)$$

For the contrast matching condition, the volume fraction weighted electron density of the water-silica mixture with the respective electron densities ρ_{H_2O} and ρ_{SiO_2} is equal to the electron density of DNA ρ_{DNA} (cf. Equation (1)). Here, x_{SiO_2}denotes the volume fraction of silica and x_{H_2O} denotes the volume fraction water. With $x_{H_2O} = 1 - x_{SiO_2}$, $\rho_{DNA} = 13 \cdot 10^{-6}\text{Å}^{-2}$, $\rho_{water} = 9.4 \cdot 10^{-6}\text{Å}^{-2}$, and $\rho_{SiO2} = 19 \cdot 10^{-6}\text{Å}^{-2}$ Equation (1) can be solved for x_{SiO_2}.

For an estimation of the DNA volume fraction of bare 24HBs, the standard atomic DNA volume in the 24HB (p8064 scaffold) is calculated via

$$1760 \cdot V_{Guanine} + 1767 \cdot V_{Cytosine} + 1942 \cdot V_{Adenine} + 2595 \cdot V_{Thymine} \quad (2)$$

to $2.47 \cdot 10^6\text{Å}^3$ (Nadassy *et al.*, 2001) and compared to the cylinder volume obtained from SAXS measurements $V_{Cyl} = \pi R_{bare}^2 L = 20.2 \cdot 10^6\text{Å}^3$. This reveals 12% DNA and 88% water volume fraction for a bare 24HBs.

S6: Silicification of 24HBs – Parameter overview

	Q $[10^{-3}cm^{-1}Å^{-3}]$	R [Å]	a [Å]	t [h]
Bare 24HBs	$Q_{bare} = 0.3$	$R_{bare} = 80.1 \pm 0.2$	$a_{bare} = 26.2 \pm 0.3$	t = 0 h
Most condensed 24HB@SiO_2		$R_{min}^{SiO2} = 74.2 \pm 0.5$	$a_{min}^{SiO2} = 23.8 \pm 0.2$	t = 4-8 h
Most condensed 24HB@TMAPS		$R_{min}^{TMAPS} = 73.4 \pm 0.4$	$a_{min}^{TMAPS} = 25.2 \pm 0.3$	t = 8h
24HB@SiO_2	$Q_{SiO2} = 1.1$	$R_{SiO2} = 80.4 \pm 0.1$	$a_{SiO2} = 24.7 \pm 0.05$	t >12 h

Table S *2* The Porod invariant (Q), the cylinder Radius (R), the interhelical spacing (a) and the time (t) for bare, most condensed, TMAPS-only exposed, and silicificated 24HBs. The parameters correspond to the data shown in Figure 1bc and 2 and were obtained from Porod invariant analysis as well as model fitting of the in-situ SAXS data.

S7: Silicification of 4-LBs – Parameter overview

	Q $[10^{-3}cm^{-1}Å^{-3}]$	A [Å]	t [h]
Bare 4-LBs	$Q_{bare} = 0.3$	$A_{bare} = 89.9 \pm 0.4$	t = 0 h
Most condensed 4-LBs@SiO_2	$Q_{SiO2} = 0.45$	$A_{min}^{SiO2} = 80.3 \pm 1.3$	t = 56 h

Table S 3 The Porod invariant (Q), the cuboid height (A), and the time (t) for bare and silicificated 4-LBs. The parameters correspond to the data shown in Figure 4bc and were obtained from Porod invariant analysis as well as model fitting of the in-situ SAXS data.

S8: SAXS data of 24HBs exposed to TMAPS only for several hours

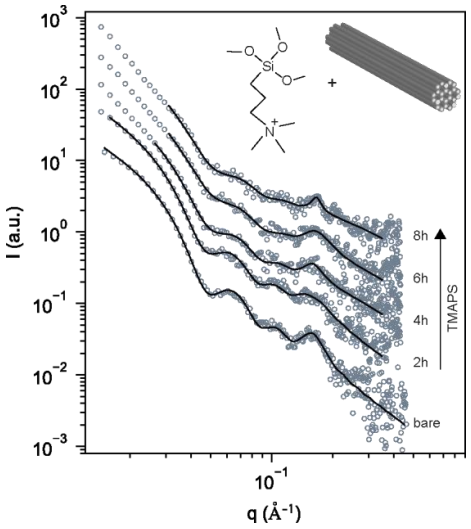

Figure S 5 SAXS intensities of bare 24HBs and after the addition of TMAPS together with the best fits of a cylinder model and Lorentz peaks accounting for the inner honeycomb lattice arrangement. Data is scaled for clarity.

S9: Temperature stability of ultrathin silica-coated 4LBs

The thermal stability of condensed ultrathin silica-coated 4-LBs@SiO_2 ($A_{SiO2} = 86.2 \pm 1.7$) is demonstrated by heating the structures to 60°C for 30min and subsequent SAXS analysis. Uncoated origamis completely dissolve at this temperature (Fischer *et al.*, 2016), whereas the origami@SiO_2 remain stable.

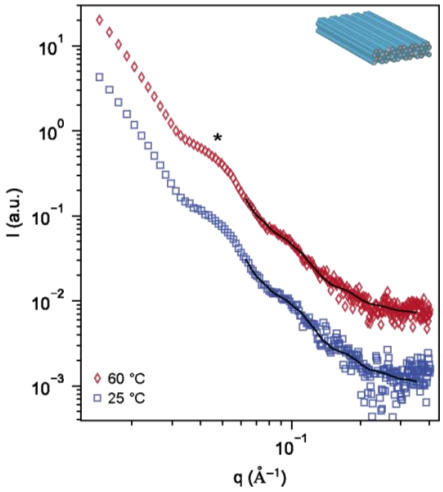

Figure S 6 SAXS intensities of condensed ultrathin silica-coated 4-LBs@SiO_2 measured at room temperature (blue squares) and after heating the structures to 60 °C for 30 min (red diamonds). The 4-LB@ SiO_2 stacking peak visible in the low q-regime is highlighted. Centre-to-centre distance is calculated to 137± 3 Å.

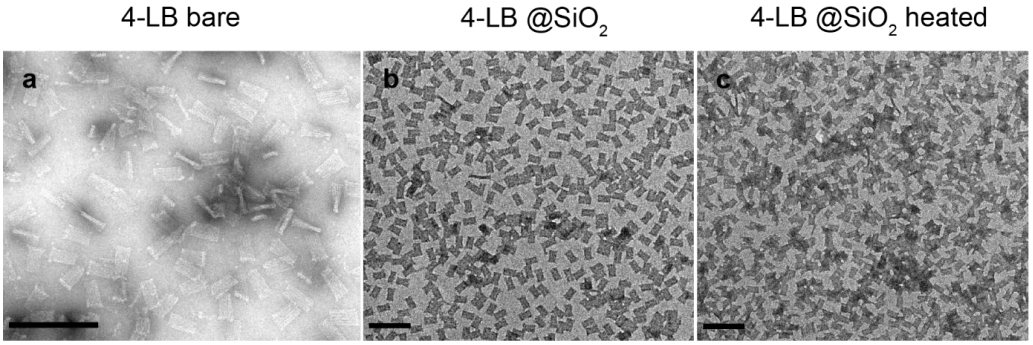

Figure S 7 Temperature stability of condensed ultrathin silica-coated 4-LBs @SiO_2 verified by TEM. TEM micrograph of (a) bare 4-LBs, (b) 4-LB @SiO_2 at room temperature and (c) after heating to 60°C for 30 min are shown. Scale bars: 200 nm.

References

Fischer, S., Hartl, C., Frank, K., Radler, J. O., Liedl, T. & Nickel, B. (2016). *Nano Lett* **16**, 4282-4287.
Mantella, V., Strach, M., Frank, K., Pankhurst, J. R., Stoian, D., Gadiyar, C., Nickel, B. & Buonsanti, R. (2020). *Angewandte Chemie International Edition* **n/a**.
Mittelbach, P. & Porod, G. (1961). *Acta Physica Austriaca* **14**, 185-211.
Nadassy, K., Tomás-Oliveira, I., Alberts, I., Janin, J. & Wodak, S. J. (2001). *Nucleic Acids Research* **29**, 3362.
O. Glatter, O. K. (1982). *Academic Press Inc. (London)*.
SasView (2014).

LIST OF FIGURES

LIST OF TABLES

LIST OF ABBREVIATIONS

24-HB	24 helix-bundle
3-LB	three layer bloc
4-LB	four layer bloc
AFM	atomic force microscopy
Ag	silver
AgNR	silver nanorod
Au	gold
Au/Ag NR	gold-silver nanorod
Au/Ag NR@DNA	DNA-functionalized gold-silver nanorod
AuNR	gold nanorod
CdTe	cadmium telluride
COC	cycloolefin co-polymer
CSDA	co-structure directing agent
Cu	copper
DESY	Deutsches Elektronen Synchrotron
DI	deionized (water)
DLS	dynamic light scattering
DNA	deoxyribonucleic acid
FCC	face centered cubic
FRAP	fluorescence recovery after photobleaching
FWHM	full width half maximum
GaAs	gallium arsenide
Ge	germanium
GUV	giant unilamellar vesicles
HB	helix-bundle
HPC	hybrid photon counting
HPLC	high-performance liquid chromatography
HR	helix-ring
LED	light emitting diode
LMU	Ludwig-Maximilian-Universität München
LUV	large unilamellar vesicles
MD	molecular dynamics
Mo	molybdenum
NIST	National Institute of Standards and Technology
NP	nanoparticle

NR	nanorod
PBS	phosphate buffered saline
PC	phosphocholine
PD	polydispersity
PSS	photostationary states
QE	quantum efficiency
SAXS	small-angle X-ray scattering
SDD	sample-to-detector distance
SEM	scanning electron microscopy
Si	silicon
SiO_2	silicon dioxide
SUV	small unilamellar vesicles
TEM	transmission electron microscopy
TEOS	Tetraethoxysilane
TMAPS	Trimethyl(3-(trimethoxysilyl)propyl)ammonium chloride
TTL	transistor-to-transistor logic
UV	ultraviolet
Vis	visible
WAXS	wide-angle X-ray scattering

BIBLIOGRAPHY

[1] Ober M F et al. In situ small-angle x-ray scattering reveals strong condensation of DNA origami during silicification. *arXiv e-prints*, page arXiv: 2204.07385, 2022.

[2] Röntgen W C. On a new kind of ray, a preliminary communication. *Wurzburg Physico-Médical Society on December*, 28, 1895.

[3] Watson J D et al. Molecular structure of nucleic acids: A structure for deoxyribose nucleic acid. *Nature*, 171(4356):737–738, 1953.

[4] Franklin R E et al. Molecular configuration in sodium thymonucleate. *Nature*, 171(4356):740–741, 1953.

[5] Wilkins M H F et al. Molecular structure of nucleic acids: Molecular structure of deoxypentose nucleic acids. *Nature*, 171(4356):738–740, 1953.

[6] Brützel L K et al. A mo-anode-based in-house source for small-angle X-ray scattering measurements of biological macromolecules. *Review of Scientific Instruments*, 87(2):025103, 2016.

[7] Fischer S et al. Shape and interhelical spacing of DNA origami nanostructures studied by small-angle X-ray scattering. *Nano Lett*, 16(7):4282–7, 2016.

[8] Hartl C et al. Position accuracy of gold nanoparticles on DNA origami structures studied with small-angle X-ray scattering. *Nano Letters*, 18(4):2609–2615, 2018.

[9] Zhang T et al. 3d DNA origami crystals. *Adv Mater*, page e1800273, 2018.

[10] Nguyen L et al. Chiral assembly of gold-silver core-shell plasmonic nanorods on DNA origami with strong optical activity. *ACS Nano*, 14(6):7454–7461, 2020.

[11] Urban P et al. A lipid photoswitch controls fluidity in supported bilayer membranes. *Langmuir*, 36(10):2629–2634, 2020.

[12] Pritzl S D et al. Optical membrane control with red light enabled by red-shifted photolipids. *Langmuir*, 2021.

[13] Ober M F et al. SAXS measurements of azobenzene lipid vesicles reveal buffer-dependent photoswitching and quantitative Z→E isomerisation by X-rays. *Nanophotonics*, 2022.

[14] Als-Nielsen J and Des M. *Elements of modern X-ray physics*. Wiley, New York, repr. jan. 2010 edition, 2010.

[15] *Neutron, X-rays and Light. Scattering Methods Applied to Soft Condensed Matter*. Elsivier, 2002.

[16] Svergun D I et al. *Small angle X-ray and neutron scattering from solutions of biological macromolecules*, volume 19. Oxford University Press, 2013.

[17] Blanchet C E et al. Versatile sample environments and automation for biological solution X-ray scattering experiments at the P12 beamline (PETRA III, DESY). *Journal of Applied Crystallography*, 48(2):431–443, 2015.

[18] Mantella V et al. Polymer lamellae as reaction intermediates in the formation of copper nanospheres as evidenced by in situ X-ray studies. *Angewandte Chemie International Edition*, 59(28):11627–11633, 2020.

[19] Sichert J A et al. Quantum size effect in organometal halide perovskite nanoplatelets. *Nano Letters*, 15(10):6521–6527, 2015.

[20] Grote L et al. X-ray studies bridge the molecular and macro length scales during the emergence of coo assemblies. *Nature Communications*, 12(1):4429, 2021.

[21] Pauw B R. Everything SAXS: small-angle scattering pattern collection and correction. *Journal of Physics: Condensed Matter*, 25(38):383201, 2013.

[22] Pedersen J S et al. Analytical treatment of the resolution function for small-angle scattering. *Journal of Applied Crystallography*, 23(4):321–333, 1990.

[23] Berger M J et al. Xcom: Photon cross sections database. *National Institute of Standards and Technology, Gaithersburg, MD, USA*, 1998.

[24] Hubbell J H et al. Atomic form factors, incoherent scattering functions, and photon scattering cross sections. *Journal of Physical and Chemical Reference Data*, 4(3):471–538, 1975.

[25] Jeffries C M et al. Limiting radiation damage for high-brilliance biological solution scattering: practical experience at the embl P12 beamline PETRAIII. *Journal of Synchrotron Radiation*, 22(2):273–279, 2015.

[26] Kuwamoto S et al. Radiation damage to a protein solution, detected by synchrotron X-ray small-angle scattering: dose-related considerations and suppression by cryoprotectants. *Journal of Synchrotron Radiation*, 11(6):462–468, 2004.

[27] Nicolas J-D et al. Radiation damage studies in cardiac muscle cells and tissue using microfocused X-ray beams: experiment and simulation. *Journal of Synchrotron Radiation*, 26(4):980–990, 2019.

[28] Cherezov V et al. Too hot to handle? Synchrotron X-ray damage of lipid membranes and mesophases. *Journal of Synchrotron Radiation*, 9(6):333–341, 2002.

[29] Paithankar K S et al. Know your dose: Raddose. *Acta Crystallographica Section D*, 66(4):381–388, 2010.

[30] Fischetti R F et al. High-resolution wide-angle X-ray scattering of protein solutions: effect of beam dose on protein integrity. *Journal of Synchrotron Radiation*, 10(5):398–404, 2003.

[31] Meisburger S et al. Breaking the radiation damage limit with cryo-SAXS. *Biophysical Journal*, 104(1):227–236, 2013.

[32] Maleknia S D et al. Determination of macromolecular folding and structure by synchrotron X-ray radiolysis techniques. *Analytical Biochemistry*, 289(2):103–115, 2001.

[33] Franke D et al. Correlation map, a goodness-of-fit test for one-dimensional X-ray scattering spectra. *Nature Methods*, 12(5):419–422, 2015.

[34] Brooks-Bartlett J C et al. Development of tools to automate quantitative analysis of radiation damage in SAXS experiments. *Journal of Synchrotron Radiation*, 24(1):63–72, 2017.

[35] Abècassis B et al. Probing in situ the nucleation and growth of gold nanoparticles by small-angle X-ray scattering. *Nano Letters*, 7(6):1723–1727, 2007.

[36] Polte J et al. Nucleation and growth of gold nanoparticles studied via in situ small angle X-ray scattering at millisecond time resolution. *ACS Nano*, 4(2):1076–1082, 2010.

[37] Wu S et al. In situ synchrotron X-ray characterization shining light on the nucleation and growth kinetics of colloidal nanoparticles. *Angewandte Chemie International Edition*, 58(27):8987–8995, 2019.

[38] Attix F H. *Introduction to Radiological Physics and Radiation Dosimetry*. Wiley VCH, 2004.

[39] Marchal J et al. Detective quantum efficiency model of single-X-ray-photon counting hybrid pixel detectors. *Journal of Instrumentation*, 7(11):P11028–P11028, 2012.

[40] Dickerson J L et al. The potential benefits of using higher X-ray energies for macromolecular crystallography. *Journal of Synchrotron Radiation*, 26(4):922–930, 2019.

[41] Narayanan T. High brilliance small-angle X-ray scattering applied to soft matter. *Current Opinion in Colloid & Interface Science*, 14(6):409–415, 2009.

[42] Tuukkanen A T et al. Progress in small-angle scattering from biological solutions at high-brilliance synchrotrons. *IUCrJ*, 4(5):518–528, 2017.

[43] Amenitsch H et al. First performance assessment of the small-angle X-ray scattering beamline at elettra. *Journal of Synchrotron Radiation*, 5(3):506–508, 1998.

[44] Buffet A et al. P03, the microfocus and nanofocus X-ray scattering (minaxs) beamline of the petra iii storage ring: the microfocus endstation. *Journal of Synchrotron Radiation*, 19(4):647–653, 2012.

[45] Seeck O H et al. The high-resolution diffraction beamline P08 at PETRA III. *Journal of Synchrotron Radiation*, 19(1):30–38, 2012.

[46] P21.1 data sheet, 2021.

[47] Honkimaki V et al. Characteristic X-ray flux from sealed cr, cu, mo, ag and w tubes. *Journal of Applied Crystallography*, 23(5):412–417, 1990.

[48] Veen F v d et al. Coherent X-ray scattering. *Journal of Physics: Condensed Matter*, 16(28):5003–5030, 2004.

[49] Fischer S. *Small-angle X-ray scattering analysis of nanomaterials*. Dissertation, 2017.

[50] Nath N et al. Label free colorimetric biosensing using nanoparticles. *Journal of Fluorescence*, 14(4):377–389, 2004.

[51] Rycenga M et al. Controlling the synthesis and assembly of silver nanostructures for plasmonic applications. *Chemical Reviews*, 111(6):3669–3712, 2011.

[52] Kelly K L et al. The optical properties of metal nanoparticles: The influence of size, shape, and dielectric environment. *The Journal of Physical Chemistry B*, 107(3):668–677, 2003.

[53] Langer J et al. Present and future of surface-enhanced raman scattering. *ACS Nano*, 14(1):28–117, 2020.

[54] Mejia-Salazar J R et al. Plasmonic biosensing. *Chemical Reviews*, 118(20):10617–10625, 2018.

[55] Doria G et al. Noble metal nanoparticles for biosensing applications. *Sensors*, 12(2):1657–1687, 2012.

[56] Gu M et al. Nanomaterials for optical data storage. *Nature Reviews Materials*, 1(12):16070, 2016.

[57] Kuzyk A et al. DNA-based self-assembly of chiral plasmonic nanostructures with tailored optical response. *Nature*, 483(7389):311–314, 2012.

[58] Kneer L M et al. Circular dichroism of chiral molecules in DNA-assembled plasmonic hotspots. *ACS Nano*, 12(9):9110–9115, 2018.

[59] Kühler P et al. Plasmonic DNA-origami nanoantennas for surface-enhanced raman spectroscopy. *Nano Letters*, 14(5):2914–2919, 2014.

[60] Funck T et al. Sensing picomolar concentrations of rna using switchable plasmonic chirality. *Angewandte Chemie International Edition*, 57(41):13495–13498, 2018.

[61] Funck T et al. Dual aptamer-functionalized 3d plasmonic metamolecule for thrombin sensing. *Applied Sciences*, 9(15):3006, 2019.

[62] Lamarre J-M et al. Anisotropic nonlinear optical absorption of gold nanorods in a silica matrix. *Optics Communications*, 281(2):331–340, 2008.

[63] Mulvihill M J et al. Anisotropic etching of silver nanoparticles for plasmonic structures capable of single-particle sers. *Journal of the American Chemical Society*, 132(1):268–274, 2010.

[64] Fernanda Cardinal M et al. Modulation of localized surface plasmons and sers response in gold dumbbells through silver coating. *The Journal of Physical Chemistry C*, 114(23):10417–10423, 2010.

[65] Jakab A et al. Highly sensitive plasmonic silver nanorods. *ACS Nano*, 5(9):6880–6885, 2011.

[66] Mayer M et al. Aqueous gold overgrowth of silver nanoparticles: Merging the plasmonic properties of silver with the functionality of gold. *Angewandte Chemie International Edition*, 56(50):15866–15870, 2017.

[67] Jette E R et al. Precision determination of lattice constants. *The Journal of Chemical Physics*, 3(10):605–616, 1935.

[68] Genix A-C et al. Nanoparticle self-assembly: from interactions in suspension to polymer nanocomposites. *Soft Matter*, 14(25):5161–5179, 2018.

[69] Livsey I. Neutron scattering from concentric cylinders. intraparticle interference function and radius of gyration. *J. Chem. Soc., Faraday Trans. II; (United Kingdom)*, pages Medium: X; Size: Pages: 1445–1452, 1987.

[70] Kotlarchyk M et al. Study of schultz distribution to model polydispersity of microemulsion droplets. *J. Phys. Chem.; (United States)*, pages Medium: X; Size: Pages: 1533–1538, 1988.

[71] SasView. Sasview software, originally developed by the DANSE project under NSF award dmr-0520547, 2014. http://www.sasview.org/sasview/index.html.

[72] Jana N R et al. Wet chemical synthesis of high aspect ratio cylindrical gold nanorods. *The Journal of Physical Chemistry B*, 105(19):4065–4067, 2001.

[73] Sharma V et al. Shape separation of gold nanorods using centrifugation. *Proceedings of the National Academy of Sciences*, 106(13):4981–4985, 2009.

[74] Wu T et al. Combinatorial study of the mushroom-to-brush crossover in surface anchored polyacrylamide. *Journal of the American Chemical Society*, 124(32):9394–9395, 2002.

[75] Brittain W J et al. A structural definition of polymer brushes. *Journal of Polymer Science Part A: Polymer Chemistry*, 45(16):3505–3512, 2007.

[76] Hartl C. *Characterization of DNA nanostructures with small-angle X-ray scattering*. Dissertation, 2018.

[77] Flory P J. *Principles of Polymer Chemistry*. Cornell University Press, Ithaca, NY,, Ithaca, New York:, 1953.

[78] Werkmeister F. *Flexible electrolyte gated organic field effect transistors for sensing*. Dissertation, 2016.

[79] Denz M et al. Cyclic olefin copolymer as an X-ray compatible material for microfluidic devices. *Lab on a Chip*, 18(1):171–178, 2018.

[80] Ilavsky J. Nika: software for two-dimensional data reduction. *Journal of Applied Crystallography*, 45(2):324–328, 2012.

[81] Holzwarth U et al. The scherrer equation versus the 'debye-scherrer equation'. *Nature Nanotechnology*, 6(9):534–534, 2011.

[82] Scherrer P. *Bestimmung der inneren Struktur und der Größe von Kolloidteilchen mittels Röntgenstrahlen*, pages 387–409. Springer Berlin Heidelberg, Berlin, Heidelberg, 1912.

[83] Li T et al. Small angle X-ray scattering for nanoparticle research. *Chemical Reviews*, 116(18):11128–11180, 2016.

[84] Mouritsen O G et al. *Life As a Matter of Fat. The Emerging Science of Lipidomics*. The Frontiers Collection. Springer, Cham, Springer-Verlag, Berlin, 2005.

[85] Akiyama H et al. Photochemically reversible liquefaction and solidification of single compounds based on a sugar alcohol scaffold with multi azo-arms. *Advanced Materials*, 24(17):2353–2356, 2012.

[86] Yamada M et al. Photomobile polymer materials-various three-dimensional movements. *Journal of Materials Chemistry*, 19(1):60–62, 2009.

[87] Kim D-Y et al. Morphological transitions of a photoswitchable aramid amphiphile nanostructure. *Nano Letters*, 21(7):2912–2918, 2021.

[88] Liang X et al. A DNA nanomachine powered by light irradiation. *ChemBioChem*, 9(5):702–705, 2008.

[89] Gao L et al. A robust, gfp-orthogonal photoswitchable inhibitor scaffold extends optical control over the microtubule cytoskeleton. *Cell Chemical Biology*, 28(2):228–241.e6, 2021.

[90] Morstein J et al. Photoswitchable lipids. *ChemBioChem*, 22(1):73–83, 2021.

[91] Hüll K et al. In vivo photopharmacology. *Chemical Reviews*, 118(21):10710–10747, 2018.

[92] Russew M-M et al. Photoswitches: From molecules to materials. *Advanced Materials*, 22(31):3348–3360, 2010.

[93] Mitscherlich E. Ueber das stickstoffbenzid. *Annalen der Physik*, 108(15):225–227, 1834.

[94] Pernpeintner C et al. Light-controlled membrane mechanics and shape transitions of photoswitchable lipid vesicles. *Langmuir*, 33(16):4083–4089, 2017.

[95] Pritzl S D et al. Photolipid bilayer permeability is controlled by transient pore formation. *Langmuir*, 36(45):13509–13515, 2020.

[96] Urban P et al. Light-controlled lipid interaction and membrane organization in photolipid bilayer vesicles. *Langmuir*, 34(44):13368–13374, 2018.

[97] Doroudgar M et al. How photoswitchable lipids affect the order and dynamics of lipid bilayers and embedded proteins. *Journal of the American Chemical Society*, 143(25):9515–9528, 2021.

[98] Yu J K et al. Nonadiabatic dynamics simulation of the wavelength-dependent photochemistry of azobenzene excited to the $n\pi^*$ and $\pi\pi^*$ excited states. *Journal of the American Chemical Society*, 142(49):20680–20690, 2020.

[99] Chatzikleanthous D et al. Lipid-based nanoparticles for delivery of vaccine adjuvants and antigens: Toward multicomponent vaccines. *Molecular Pharmaceutics*, 18(8):2867–2888, 2021.

[100] Wang N et al. Liposomes used as a vaccine adjuvant-delivery system: From basics to clinical immunization. *Journal of Controlled Release*, 303:130–150, 2019.

[101] Kumpulainen T et al. Ultrafast elementary photochemical processes of organic molecules in liquid solution. *Chemical Reviews*, 117(16):10826–10939, 2017.

[102] Duarte L et al. Structural and spectroscopic characterization of e- and z-isomers of azobenzene. *Physical Chemistry Chemical Physics*, 16(32):16919–16930, 2014.

[103] Baroncini M et al. Light-responsive (supra)molecular architectures: Recent advances. *Advanced Optical Materials*, 7(16):1900392, 2019.

[104] Wagner-Wysiecka E et al. Azo group(s) in selected macrocyclic compounds. *Journal of Inclusion Phenomena and Macrocyclic Chemistry*, 90(3):189–257, 2018.

[105] Broichhagen J et al. A roadmap to success in photopharmacology. *Accounts of Chemical Research*, 48(7):1947–1960, 2015.

[106] Krämer R. *E/Z Isomerisierungen in molekularen Schaltern - Die Azogruppe als molekularer Schlüsselbaustein*. Dissertation, 2016.

[107] Urban P. *Optical control of lipid interaction in photolipid membranes*. Dissertation, 2021.

[108] Quick M et al. Photoisomerization dynamics and pathways of trans- and cis-azobenzene in solution from broadband femtosecond spectroscopies and calculations. *The Journal of Physical Chemistry B*, 118(29):8756–8771, 2014.

[109] Otolski C J et al. Spatial confinement alters the ultrafast photoisomerization dynamics of azobenzenes. *Chemical Science*, 11(35):9513–9523, 2020.

[110] Crecca C R et al. Theoretical study of the isomerization mechanism of azobenzene and disubstituted azobenzene derivatives. *The Journal of Physical Chemistry A*, 110(26):8188–8203, 2006.

[111] Aleotti F et al. Multidimensional potential energy surfaces resolved at the raspt2 level for accurate photoinduced isomerization dynamics of azobenzene. *Journal of Chemical Theory and Computation*, 15(12):6813–6823, 2019.

[112] Jerca F A et al. Advances and opportunities in the exciting world of azobenzenes. *Nature Reviews Chemistry*, 2021.

[113] Demchenko A P et al. Breaking the kasha rule for more efficient photochemistry. *Chemical Reviews*, 117(21):13353–13381, 2017.

[114] Bandara H M D et al. Photoisomerization in different classes of azobenzene. *Chemical Society Reviews*, 41(5):1809–1825, 2012.

[115] Kathan M et al. Photoswitchable molecules as key ingredients to drive systems away from the global thermodynamic minimum. *Chemical Society Reviews*, 46(18):5536–5550, 2017.

[116] Goulet-Hanssens A et al. Electrocatalytic z $\rightarrow$ e isomerization of azobenzenes. *Journal of the American Chemical Society*, 139(1):335–341, 2017.

[117] Goulet-Hanssens A et al. Hole catalysis as a general mechanism for efficient and wavelength-independent z $\rightarrow$ e azobenzene isomerization. *Chem*, 4(7):1740–1755, 2018.

[118] Chu Z et al. Supramolecular control of azobenzene switching on nanoparticles. *Journal of the American Chemical Society*, 141(5):1949–1960, 2019.

[119] Banerjee G et al. Uv induced bystander signaling leading to apoptosis. *Cancer Letters*, 223(2):275–284, 2005.

[120] Cheong W F et al. A review of the optical properties of biological tissues. *IEEE Journal of Quantum Electronics*, 26(12):2166–2185, 1990.

[121] Hope M J et al. Production of large unilamellar vesicles by a rapid extrusion procedure. characterization of size distribution, trapped volume and ability to maintain a membrane potential. *Biochimica et Biophysica Acta (BBA) - Biomembranes*, 812(1):55–65, 1985.

[122] Baptist A. *Kleinwinkel-Röntgenstreuung an photoschaltbaren Lipidmembranen*. Bachelor thesis, 2018.

[123] Ong S G M et al. Evaluation of extrusion technique for nanosizing liposomes. *Pharmaceutics*, 8(4):36, 2016.

[124] Sattler C. Laborpraktikumsbericht. 2018.

[125] Bouwstra J A et al. Small angle X-ray scattering: possibilities and limitations in characterization of vesicles. *Chemistry and Physics of Lipids*, 64(1):83–98, 1993.

[126] Pabst G et al. Structural analysis of weakly ordered membrane stacks. *Journal of Applied Crystallography*, 36(6):1378–1388, 2003.

[127] Brzustowicz M R et al. X-ray scattering from unilamellar lipid vesicles. *Journal of Applied Crystallography*, 38(1):126–131, 2005.

[128] Komorowski K et al. Vesicle adhesion and fusion studied by small-angle X-ray scattering. *Biophys J*, 114(8):1908–1920, 2018.

[129] Kučerka N et al. Influence of cholesterol on the bilayer properties of monounsaturated phosphatidylcholine unilamellar vesicles. *The European Physical Journal E*, 23(3):247–254, 2007.

[130] Kučerka N et al. Fluid phase lipid areas and bilayer thicknesses of commonly used phosphatidylcholines as a function of temperature. *Biochimica et Biophysica Acta (BBA) - Biomembranes*, 1808(11):2761–2771, 2011.

[131] Pabst G et al. X-ray kinematography of temperature-jump relaxation probes the elastic properties of fluid bilayers. *Langmuir*, 16(23):8994–9001, 2000.

[132] Rappolt M et al. Structural, dynamic and mechanical properties of popc at low cholesterol concentration studied in pressure/temperature space. *European Biophysics Journal*, 31(8):575–585, 2002.

[133] Hung W-C et al. The condensing effect of cholesterol in lipid bilayers. *Biophysical Journal*, 92(11):3960–3967, 2007.

[134] Kučerka N et al. The effect of cholesterol on short- and long-chain monounsaturated lipid bilayers as determined by molecular dynamics simulations and X-ray scattering. *Biophysical Journal*, 95(6):2792–2805, 2008.

[135] Czeslik C et al. Effect of high pressure on the structure of dipalmitoylphosphatidylcholine bilayer membranes: a synchrotron-X-ray diffraction and ft-ir spectroscopy study using the diamond anvil technique. *Chemistry and Physics of Lipids*, 91(2):135–144, 1998.

[136] Winter R et al. Pressure effects on the structure of lyotropic lipid mesophases and model biomembrane systems. *Zeitschrift für Kristallographie - Crystalline Materials*, 215(8):454–474, 2000.

[137] Winter R et al. Effect of pressure on membranes. *Soft Matter*, 5(17):3157–3173, 2009.

[138] Weiss T M et al. Hydrophobic mismatch between helices and lipid bilayers. *Biophysical Journal*, 84(1):379–385, 2003.

[139] Kuiper J M et al. H-aggregation of azobenzene-substituted amphiphiles in vesicular membranes. *Langmuir*, 20(4):1152–1160, 2004.

[140] Jämbeck J P M et al. Derivation and systematic validation of a refined all-atom force field for phosphatidylcholine lipids. *The Journal of Physical Chemistry B*, 116(10):3164–3179, 2012.

[141] Mills T T et al. Order parameters and areas in fluid-phase oriented lipid membranes using wide angle X-ray scattering. *Biophysical Journal*, 95(2):669–681, 2008.

[142] Bortolus P et al. Cis-trans photoisomerization of azobenzene: Solvent and triplet donor effects. 1979.

[143] R. King N et al. Effect of media polarity on the photoisomerisation of substituted stilbene, azobenzene and imine chromophores. *Journal of Materials Chemistry*, 7(4):625–630, 1997.

[144] Serra F et al. Effects of solvent viscosity and polarity on the isomerization of azobenzene. *Macromolecules*, 41(3):981–986, 2008.

[145] Fischer E. Temperature dependence of photoisomerization equilibria. part i. azobenzene and the azonaphthalenes. *Journal of the American Chemical Society*, 82(13):3249–3252, 1960.

[146] Malkin S et al. Temperature dependence of photoisomerization. part ii. 1 quantum yields of cis- trans isomerizations in azo-compounds. *The Journal of Physical Chemistry*, 66(12):2482–2486, 1962.

[147] Kojima M et al. Effect of solvent on cis-to-trans isomerization of 4-hydroxyazobenzene aggregated through intermolecular hydrogen bonds. *Journal of Physical Organic Chemistry*, 18(10):994–1000, 2005.

[148] Schanze K S et al. Solvent effects on the thermal cis-trans isomerization and charge-transfer absorption of 4-(diethylamino)-4'-nitroazobenzene. *The Journal of Organic Chemistry*, 48(17):2808–2813, 1983.

[149] Blevins A A et al. Effect of positional substitution on the optical response of symmetrically disubstituted azobenzene derivatives. *The Journal of Physical Chemistry B*, 108(16):4962–4968, 2004.

[150] Yu S H et al. Consideration of azobenzene-based self-assembled monolayer deposition conditions for maximizing optoelectronic switching performances. *Chemistry of Materials*, 33(15):5991–6002, 2021.

[151] Gurtovenko A A et al. Effect of nacl and kcl on phosphatidylcholine and phosphatidylethanolamine lipid membranes: Insight from atomic-scale simulations for understanding salt-induced effects in the plasma membrane. *The Journal of Physical Chemistry B*, 112(7):1953–1962, 2008.

[152] Pabst G et al. Rigidification of neutral lipid bilayers in the presence of salts. *Biophysical Journal*, 93(8):2688–2696, 2007.

[153] Gurtovenko A A. Asymmetry of lipid bilayers induced by monovalent salt: Atomistic molecular-dynamics study. *The Journal of Chemical Physics*, 122(24):244902, 2005.

[154] De Mel J U et al. Influence of salt on membrane rigidity of neu-tral dopc vesicles, April 01, 2020 2020.

[155] Yue B et al. Highly stable phospholipid unilamellar vesicles from spontaneous vesiculation: A dls and sans study. *The Journal of Physical Chemistry B*, 109(1):609–616, 2005.

[156] Sachs J N et al. Changes in phosphatidylcholine headgroup tilt and water order induced by monovalent salts: Molecular dynamics simulations. *Biophysical Journal*, 86(6):3772–3782, 2004.

[157] Clarke R J et al. Influence of anions and cations on the dipole potential of phosphatidylcholine vesicles: A basis for the hofmeister effect. *Biophysical Journal*, 76(5):2614–2624, 1999.

[158] Lessard J G et al. Micropolarities of lipid bilayers and micelles. iii: Effect of monovalent ions on the dielectric constant of the water-membrane interface of unilamellar phosphatidylcholine vesicles. *J. phys. chem. (1952)*, 90(5):811–817, 1986.

[159] Kimura Y et al. Local dielectric properties around polar region of lipid bilayer membranes. *The Journal of Membrane Biology*, 85(3):225–231, 1985.

[160] Konrad D B et al. Computational design and synthesis of a deeply red-shifted and bistable azobenzene. *Journal of the American Chemical Society*, 142(14):6538–6547, 2020.

[161] Seemann H et al. Volumetric properties, compressibilities and volume fluctuations in phospholipid-cholesterol bilayers. *Zeitschrift für Physikalische Chemie*, 217(7):831–846, 2003.

[162] Rothemund P W K. Folding DNA to create nanoscale shapes and patterns. *Nature*, 440(7082):297–302, 2006.

[163] Seeman N C et al. DNA nanotechnology. *Nature Reviews Materials*, 3(1):17068, 2018.

[164] Douglas S M et al. Self-assembly of DNA into nanoscale three-dimensional shapes. *Nature*, 459(7245):414–418, 2009.

[165] Loescher S et al. 3d DNA origami nanoparticles: From basic design principles to emerging applications in soft matter and (bio-)nanosciences. *Angewandte Chemie International Edition*, 57(33):10436–10448, 2018.

[166] Hong F et al. DNA origami: Scaffolds for creating higher order structures. *Chemical Reviews*, 117(20):12584–12640, 2017.

[167] Wagenbauer K F et al. Gigadalton-scale shape-programmable DNA assemblies. *Nature*, 552(7683):78–83, 2017.

[168] Liu W et al. Diamond family of nanoparticle superlattices. *Science*, 351(6273):582–586, 2016.

[169] Dass M et al. DNA origami-enabled plasmonic sensing. *The Journal of Physical Chemistry C*, 125(11):5969–5981, 2021.

[170] Stein I H et al. Single-molecule four-color fret visualizes energy-transfer paths on DNA origami. *Journal of the American Chemical Society*, 133(12):4193–4195, 2011.

[171] Nicoli F et al. Directional photonic wire mediated by homo-förster resonance energy transfer on a DNA origami platform. *ACS Nano*, 11(11):11264–11272, 2017.

[172] Douglas S M et al. DNA-nanotube-induced alignment of membrane proteins for nmr structure determination. *Proceedings of the National Academy of Sciences*, 104(16):6644–6648, 2007.

[173] Sacca B et al. Orthogonal protein decoration of DNA origami. *Angewandte Chemie*, 122(49):9568–9573, 2010.

[174] Nickels P C et al. Molecular force spectroscopy with a DNA origami-based nanoscopic force clamp. *Science*, 354(6310):305–307, 2016.

[175] Ochmann S E et al. Optical nanoantenna for single molecule-based detection of zika virus nucleic acids without molecular multiplication. *Analytical Chemistry*, 89(23):13000–13007, 2017.

[176] Selnihhin D et al. Multifluorophore DNA origami beacon as a biosensing platform. *ACS Nano*, 12(6):5699–5708, 2018.

[177] He L et al. Rationally programming nanomaterials with DNA for biomedical applications. *Advanced Science*, 8(8):2003775, 2021.

[178] Hu Q et al. DNA nanotechnology-enabled drug delivery systems. *Chemical Reviews*, 119(10):6459–6506, 2019.

[179] Liu J et al. A DNA-based nanocarrier for efficient gene delivery and combined cancer therapy. *Nano Letters*, 18(6):3328–3334, 2018.

[180] Liu N et al. DNA-assembled advanced plasmonic architectures. *Chemical Reviews*, 118(6):3032–3053, 2018.

[181] Paunescu D et al. Reversible DNA encapsulation in silica to produce ros-resistant and heat-resistant synthetic DNA 'fossils'. *Nature Protocols*, 8(12):2440–2448, 2013.

[182] Perrault S D et al. Virus-inspired membrane encapsulation of DNA nanostructures to achieve in vivo stability. *ACS Nano*, 8(5):5132–5140, 2014.

[183] Nguyen L et al. DNA-origami-templated silica growth by sol-gel chemistry. *Angewandte Chemie International Edition*, 58(3):912–916, 2019.

[184] Nguyen M-K et al. Ultrathin silica coating of DNA origami nanostructures. *Chemistry of Materials*, 32(15):6657–6665, 2020.

[185] Wang Y et al. DNA origami single crystals with wulff shapes. *Nature Communications*, 12(1):3011, 2021.

[186] Shang Y et al. Site-specific synthesis of silica nanostructures on DNA origami templates. *Advanced Materials*, 32(21):2000294, 2020.

[187] Zhao Y et al. Programmable and site-specific patterning on DNA origami templates with heterogeneous condensation of silver and silica. *Small*, page 2103877, 2021.

[188] Jing X et al. Solidifying framework nucleic acids with silica. *Nature Protocols*, 14(8):2416–2436, 2019.

[189] Michelson A et al. Engineered silicon carbide three-dimensional frameworks through DNA-prescribed assembly. *Nano Letters*, 21(4):1863–1870, 2021.

[190] Stöber W et al. Controlled growth of monodisperse silica spheres in the micron size range. *Journal of Colloid and Interface Science*, 26(1):62–69, 1968.

[191] Roodhuizen J A L et al. Counterion-dependent mechanisms of DNA origami nanostructure stabilization revealed by atomistic molecular simulation. *ACS Nano*, 13(9):10798–10809, 2019.

[192] Kielar C et al. On the stability of DNA origami nanostructures in low-magnesium buffers. *Angewandte Chemie*, 130(30):9614–9618, 2018.

[193] Balmer J A et al. Time-resolved small-angle X-ray scattering studies of polymer-silica nanocomposite particles: Initial formation and subsequent silica redistribution. *Journal of the American Chemical Society*, 133(4):826–837, 2011.

[194] Han H et al. Core-shell-corona silica hybrid nanoparticles templated by spherical polyelectrolyte brushes: A study by small angle X-ray scattering. *Langmuir*, 33(38):9857–9865, 2017.

[195] Olsson A et al. A holder to rotate sample cells to avoid sedimentation in small-angle neutron scattering and ultra small-angle neutron scattering experiments. *Measurement Science and Technology*, 24(10):105901, 2013.

[196] Brummer C. *In-situ Small-angle X-ray Scattering on Silicificated DNA Origamis*. Bachelor thesis, 2020.

[197] Frank K. *Kleinwinkelröntgenstreuung an DNA-Origami-Kristallen und Lipidphasen*. Master thesis, 2017.

[198] Mittelbach P et al. Zur Röntgenkleinwinkelstreuung verdünnter kolloider Systeme. die Berechnung der Streukurven von Parallelepipeden. *Acta Physica Austriaca*, 14:185–211, 1961.

[199] O. Glatter O K. Small angle X-ray scattering. *Academic Press Inc. (London)*, 1982.

[200] Majewski P W et al. Resilient three-dimensional ordered architectures assembled from nanoparticles by dna. *Science Advances*, 7(12):eabf0617, 2021.

[201] Huang H et al. Growth of perovskite CsPbBr3 nanocrystals and their formed superstructures revealed by in situ spectroscopy. *Chemistry of Materials*, 32(20):8877–8884, 2020.

[202] Rieker T P et al. Small-angle X-ray scattering study of the morphology of carbon black mass fractal aggregates in polymeric composites. *Langmuir*, 16(13):5588–5592, 2000.

[203] Qiu X et al. Measuring inter-DNA potentials in solution. *Physical Review Letters*, 96(13):138101, 2006. PRL.

[204] Ponnuswamy N et al. Oligolysine-based coating protects DNA nanostructures from low-salt denaturation and nuclease degradation. *Nature Communications*, 8(1):15654, 2017.